ISSN 1000-9620

海洋通报

Marine Science Bulletin

NATIONAL MARINE DATD AND
INFORMATION SERVICE OF CHINA

2011
Volume 13
Number 1

MARINE SCIENCE BULLETIN

Vol. 13 No. 1 May 2011

CONTENTS

Study on the relationship between ENSO and tropical Indian Ocean temperature ····· CAI Yi et al. (01)

Study on the Meso-scale process of the Kuroshio front to the east of Taiwan ····· WANG Qi et al. (10)

Freak wave simulation based on nonlinear model and the research on the time-frequency energy spectrum of simulation results ····· CUI Cheng et al. (25)

Characteristic analysis of Tianjin offshore tide ····· LI Xi-bin et al. (40)

Distribution of dissolved cadmium in Prydz Bay, Antarctica ····· SUN Wei-ping et al. (50)

Preliminary screening of antimicrobial and antitumor activities from cultivated microalgaes ····· DENG Wei et al. (60)

Heavy metal distribution patterns and environmental quality assessment of the mariculture areas in Nanao, Shantou ····· ZHOU Yan-hui et al. (71)

Seasonal variations in species composition and abundance of tintinnids in Shantou coastal water, China ····· LIU Hua-xue et al. (80)

Research and realization of visual digital ocean system ····· ZHANG Feng et al. (87)

LIBRARY
LIBRARY
Pacific Islands Fisheries Science Center
NOAA Fisheries
Honolulu, Hawai'i

Study on the relationship between ENSO and tropical Indian Ocean temperature

CAI Yi, LI Hai

National Research Center for Marine Environmental Forecasting, Beijing 100081

Abstract: The relationship between ENSO and Indian Ocean Dipole was discussed by using the data set of sea temperature from Scripps Institute of Oceanography, the air temperature at 1000hPa from the NCEP reanalysis data and the Nino3 index from the Climate Prediction Center (CPC) of U.S.A. during the period from 1955 to 2001. The results show that there exists a Dipole on the maximum temperature anomalous level (MTAL) in the Indian Ocean, which close relates to ENSO in the Pacific Ocean. During El Nino periods there are good relationships between ENSO and Indian Ocean Dipole which maximum correlation occurring when ENSO leads by one month, but in La Nina periods the relationship is not so good. The distribution of Dipole in Indian Ocean is from northeast to southwest, which one (west) pole in 65°E - 75°E, 6°S - 10°S and the other in 85°E - 95°E, 2°N - 6°N, which is different from that defined by Saij. The correlation coefficients of Nino3 index with temperature anomalies in the west/east poles on the MTAL are over 0.4 - 0.15, respectively. It is a main sea temperature system in the tropical Indian Ocean. However, in the surface layer from sea surface to the depth of 20 m - 30 m there is no such a dipole with opposite sea temperature anomalies in the NE and SW of tropical Indian Ocean. The SSTA in the NE might be influenced by the sensible exchange process because the evolution of sea and 1 000 hPa air temperature anomaly time series of the NE of tropical Indian Ocean is quite similar except those during 1962 - 1963 and 1986. The periods of Indian Ocean Dipole are shorter than that of ENSO, and about 1 to 6-year.

Keywords: Pacific Ocean ENSO, Indian Ocean dipole, vertical maximal temperature anomalous level, EOF analysis

Introduction

Since the concept Dipole of Tropic Indian Sea Surface Temperature Anomaly (SSTA) was firstly promoted by Saij and Yamagata (1999), the study about it induces people's

Received on Feb. 18, 2011

Corresponding author: caiyi@nmefc.gov.cn.

great interests. Saij and Webster (1999) think it is a interaction phenomenon between air and ocean in the tropical Indian Ocean, which has no relationship with ENSO, in fact, the relationship between the Dipole index and the ENSO is not good, Cao (2001) and Cai (2005) by studying the evolution of sea temperature anomaly on the upper layer maximum temperature anomalous level (MTAL) in the Indian Ocean, concludes that the Dipole closely related to the ENSO. Li Chongyin, et al. (2001) thought the Dipole not only exists in the Indian Ocean, but also has good negative relationship with ENSO, and their connection is mainly by the tropical atmosphere Walker circulation. Qian Haifeng et al. (2003) thought below the 80m of surface layer, the Dipole phenomenon is more obviously and closely relates to ENSO. Stefan Hastenrath (2002) thought there was no Dipole existing in the Indian Ocean, and the Dipole should be a phenomenon similar to teeterboard, one side positive and the other side negative, but the SSTA to the east and west ends of the Tropical Indian Ocean Sea Surface has positive relationship, and the Dipole is only their relative difference. Therefore, by now there are still many different opinions about the Dipole. The above mentioned work on the relationship between the Dipole and ENSO is from the definition of the Dipole of Tropical Indian Sea Surface to discuss. Here we start from ENSO to discuss the relationship between ENSO and the Indian Ocean Sea Temperature Anomaly and the Indian Ocean Dipole.

1 Data sources

The data set of sea temperature for analysis is monthly averaged sea temperature reanalysis data coming from Scripps Institute of Oceanography of U.S.A. from Jan. 1955 to Dec. 2001, totally 564 months. The vertical direction ranges from 0 m to 400 m and is divided to 11 layers, they are 0 m, 20 m, 40 m, 60 m, 80 m, 120 m, 160 m, 200 m, 240 m, 300m, and 400 m, respectively. The horizontal extension is 20°S - 20° N, 40^{0}E - 120^{0}E, the grid space is 5° (lon)×2° (lat). El Nino is defined by the Tropical Pacific SSTA in the region of Nino3, the data set comes from the Climate Prediction Center (CPC) of U.S.A. (http://www.cpc.ncep.noaa.gov/data/indices/). The monthly averaged air temperature at 1000hPa comes from the NCEP's reanalysis data from 1960 to 1999, and the horizontal grid space is 2.5°(lon) × 2.5°(lat). The above data refers to climate averaged anomalies, therefore, the climate average of above data must be calculated firstly, and then subtracted by the original data to get the climate averaged anomalies. The below discussions are all for the anomalies.

2 Data analysis

In order to discuss the relationship between ENSO and the Indian Ocean sea temperature, the correlation between the SSTA in the Nino3 region and the Indian Ocean sea temperature anomaly (STA) on the vertical Maximum Temperature Anomaly Level (MTAL) is analyzed (Fig. 1a). The so called MTAL is a curved surface of climate averaged vertical maximum sea temperature anomaly. Cao Jiping et al. (2003) proved that the MTAL corresponds to the oceanic upper layer thermocline, which can reflect the characteristics of oceanic upper layer well. It can be seen from Fig. 1a that the Pacific ENSO is obviously related to the STA on the Indian Ocean MTAL, and the maximum positive correlation is located to the south tropic, about in the domain of 65°E - 75°E, 6°S - 10°S (the West Indian Ocean), the correlation coefficient is over 0.4, and along the east coast of the equatorial Indian Ocean in the domain of 85°E - 95°E, 2°N - 6°N (the East Indian Ocean) has negative correlation center, and the correlation coefficient is over -0.15. It can also be seen from Fig. 1a that on the MTAL the distribution of SSTA which closely relates to the ENSO has the phenomenon of Dipole similar to the teeterboard, but its position is different from that defined by Saij, which is along the direction from the northeast to the southwest. The STA distribution on the MTAL is called Dipole in this paper, and the index of Dipole is defined by the difference of above defined northeast Indian Oceanic STA subtracted by the southwestern Indian Oceanic STA. The correlation analysis between the Dipole index and Nino3's SSTA shows that the ENSO one month leading the Indian Ocean Dipole has the maximum correlation to the Indian Ocean Dipole, and the correlation coefficient is 0.46 (Fig. 1b). It can be seen from Fig. 1b that the year of El Nino has good corresponding relationship with Dipole, and each El Nino corresponds to an Indian Ocean Dipole except 1994, but it is not true for the year of La Nina. Therefore the Dipole on the MTAL, especially the events of negative phase, is not caused by the ENSO completely and it is also related to the air-ocean interaction itself. It can be known from the power spectra analysis that the period of Indian Ocean Dipole is shorter than the period of El Nino, usually 1 to 6 years. From the above analysis it can be concluded that along the direction from northeast from southwest on the MTAL of the Indian Ocean there exists the phenomenon of Dipole similar to the teeterboard, which has good correlation with ENSO, and the maximum correlation with ENSO is at the time of one month leading the Indian Ocean Dipole.

Similarly, in order to discuss the relationship between ENSO and the SSTA of the Indian Ocean, the correlations between Nino3's SSTA and SSTA of Indian Ocean were shown on Fig. 2. It can be seen from Fig. 2 that there is no Dipole distribution similar to that correlation coefficients of sea temperature on MTAL. The whole Indian Ocean is a

consistent positive correlation, and two largest correlation centers are located at the northeast Indian Ocean and the southwest Indian Ocean, respectively, which are consistent with the positions of Dipole on MTAL (Fig. 1a), but the difference is that the negative correlation center of the northeastern Indian Ocean on the MTAL with ENSO becomes positive correlation center here and the correlation coefficient is greater than 0.35, therefore it can be known that the positive correlation of the STA in the southwest Indian Ocean with ENSO is a deep system of the upper layer the Indian Ocean, but to the northeast, the STA of the upper layer and deeper layer Indian Ocean correlating to ENSO is a non-consistent system and this is a problem the researchers are arguing with, there is a Dipole in the Indian Ocean and whether this Dipole correlates to ENSO or not if it exists. According to Stefan Hastenrath [7] , it can be seem from Fig. 2 that at least the SSTA of the Indian Ocean has no Dipole correlating to ENSO.

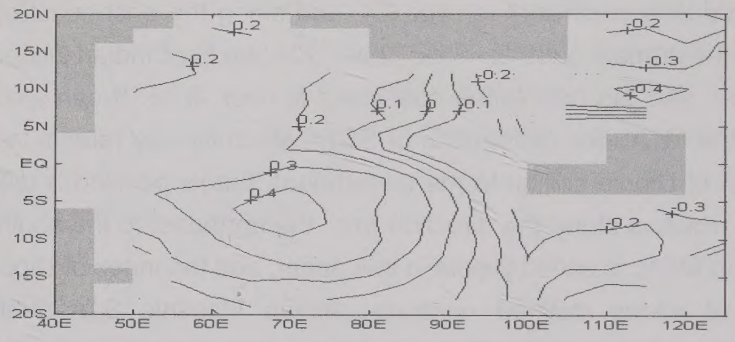

Fig. 1a Distribution of correlation between SSTA in Nino3 and the temperature anomaly in MATL

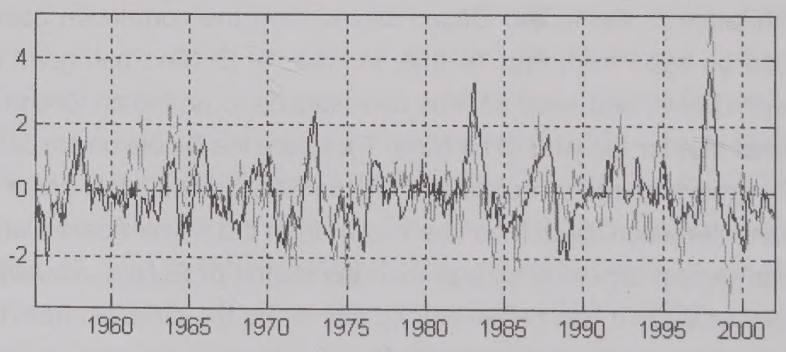

Fig. 1b Dipole index in MATL (dashed line) and SSTA in Nino3 (solid line)

In order to know how the center correlating to ENSO in the northeast Indian Ocean and the STA at the vertical direction of the whole equatorial Indian Ocean distribute, the longitudinal average along the 2°S - 2°N was made to get the vertical profile and then the EOF analysis of the STA was carried out on the profile. Fig. 3a shows the first character vector of EOF analysis of STA on the vertical longitudinal profile, and Fig. 3b shows the

time coefficient and the SSTA of Nino3 region, which the ratio of first character vector of EOF analysis to the total is 24%. For comparing with the SSTA of Nino3, the time coefficient was normalized first. It can be seen from Fig. 3 that in the Indian Ocean, the time coefficient of the first character vector and the SSTA of Nino3 region correlates well, the correlation coefficient for the same period is the largest, which is 0.504. The distribution of STA at the vertical direction along the equator in the Indian Ocean is similar to that of the Pacific's, the warm center is at east and the cold center is at west, respectively. It is constant warm center from the sea surface to the 200m depth layer in the west Indian Ocean, and the cold center of east Indian Ocean is on the layer under 20-50m. Combing Fig. 1a and Fig. 2 it can be known that the center of positive anomaly on the sea surface of the equatorial east Indian Ocean, which correlates to ENSO, is a very shallow system whose depth is from the sea surface to the 20 m - 50m layer only, but for the whole equatorial Indian Ocean, the main system is a Dipole similar to the teeterboard and this Dipole correlates to ENSO well and this is a big different between the Indian Ocean's Dipole and the Pacific Ocean's ENSO. The shallow system from the sea surface to the 20-50m layer in the eastern Indian Ocean may be caused by local ocean-air thermal process. In order to verify this conjecture, the correlation coefficients between SSTA in Nino3 region and the air temperature anomaly of the Indian Ocean on 1 000 hPa was shown on Fig. 4. It can be seen from the figure that there is a positive correlation center which the correlation coefficient is larger than 0.3 in the upper atmosphere layer above the equatorial northeast Indian Ocean, and this center is near the correlation center of the SSTA of the equatorial eastern Indian Ocean (Fig. 2). The variations of the averaged STA's center (80°E - 90°E, 0°N - 6°N) of the eastern Indian Ocean and the averaged air temperature anomaly's center on the 1000hPa (77.5°E - 85°E, 5°N - 10°N) with time were shown on Fig. 5, on which the two curves are uniformed, from the figure it can be seen that except the early 1960's and 1986, the two averaged centers have very consistent varying tendency in all other years and this proved our conjecture from another side.

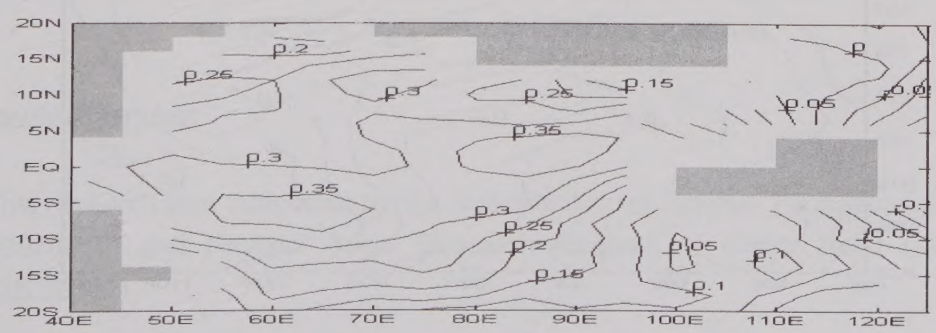

Fig. 2 Distribution of correlation between SSTA in Nino3 and the temperature anomaly on Indian Ocean sea surface

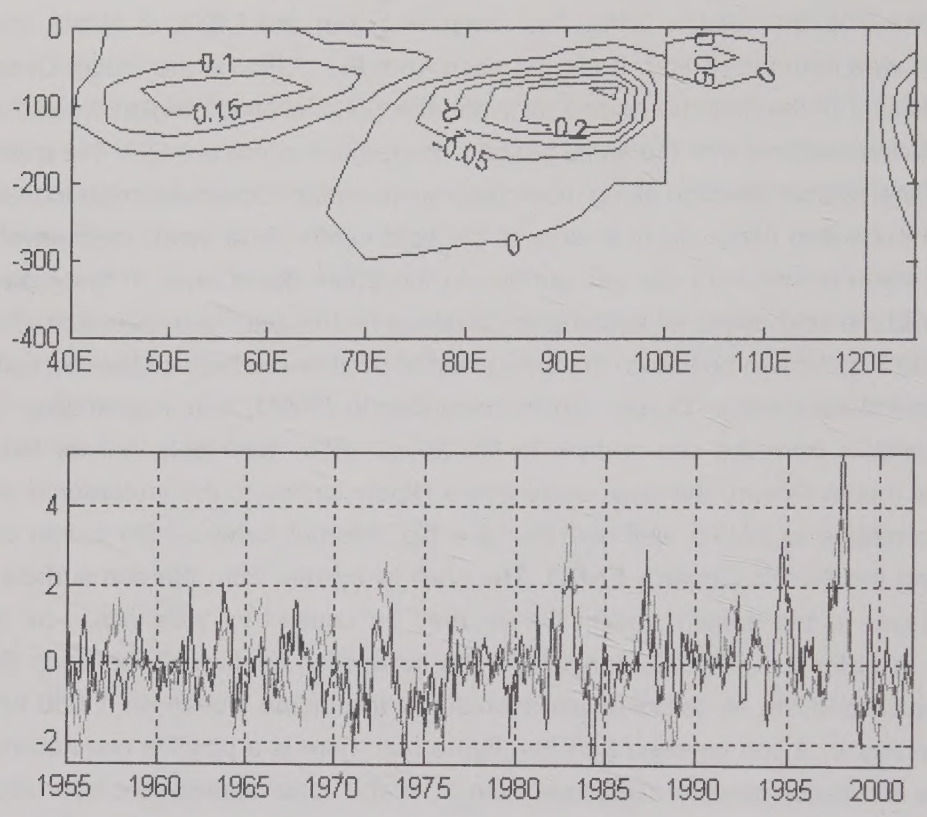

Fig. 3 EOF analysis of the temperature anomaly of equatorial latitudinal vertical section

(a) the first mode eigenvector (b) the first mode time serial (dashed line)

and SSTA in Nino3 (solid line)

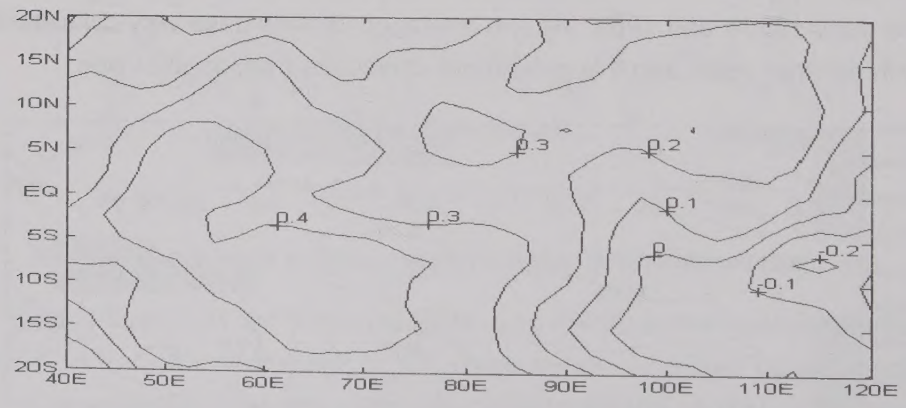

Fig. 4 Distribution of correlation between SSTA in Nino3 and Indian Ocean air temperature anomaly in 1 000 hPa.

3 Conclusion

By analyzing the atmospheric and oceanic data set of the Indian Ocean, it was found that the STA distribution on the MTAL of the Indian Ocean has a phenomenon of Dipole which closely correlates to ENSO, but the distribution of STA is different from the one defined by Saij, which is along the direction of northeast and southwest. The Dipole is a main system of equatorial Indian Ocean, but the difference from ENSO is that the Dipole is located in equatorial eastern Indian Ocean and the STA does not extend to the sea surface. The distribution of STA from the sea surface to the shallow water layer of 20 m - 50m has the same sign as that in the equatorial southwest Indian Ocean, therefore on the sea surface, there is no Dipole phenomenon correlating to the ENSO. The same STA sign of the equatorial eastern Indian Ocean and the equatorial southwestern Indian Ocean may be caused by the air-ocean thermal process, such as sensible heat.

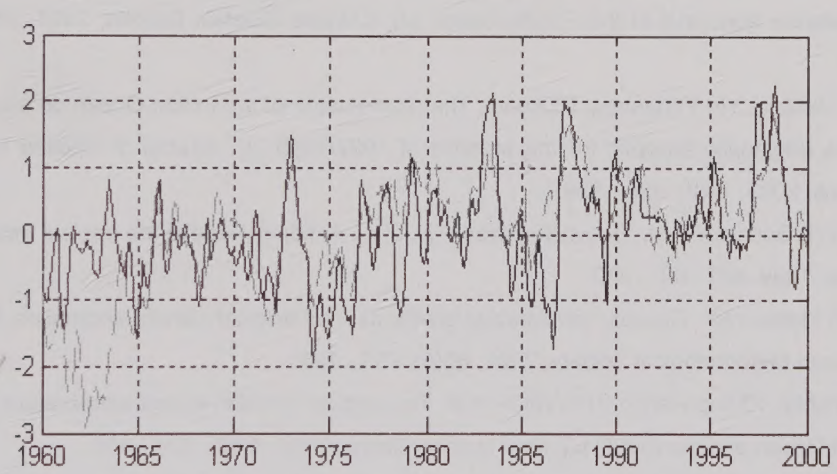

Fig. 5 The mean sea surface temperature anomaly (80°E - 90°E, 0°N - 6°N) in equatorial east Indian Ocean (dashed line) and the mean air temperature anomaly (77.5°E - 85°E, 5°N - 10°N) in 1 000 hPa (solid line)

Acknowledgement

This research was supported by the National Natural Science Foundation of China, (No. 40976015) and National Basic Research Program of China under Grant No. (2010CB950302).

Reference

[1] Cai Yi, Zhang Jianhua, Yu Weidong. The upper layer sea temperature analysis of the equatorial Pacific Ocean and Indian Ocean [J]. Journal of Tropical Oceanography, 2005, 24(4): 60 - 66.

[2] Cao Jiping, Cao Qingchen, Liu Lin. The ENSO event of tropical Pacific Ocean and the dipole event of the Indian Ocean [J]. Acta Meteor. Sinica, 2005, 63(5): 594 - 602.

[3] Cao Jiping, Yuan Shaoyu, Cai Yi. The events of large scale air-ocean interaction on the tropical Indian Ocean [J]. Acta Meteor. Sinica, 2003, 61(2): 251 - 256.

[4] Cao Qingchen, Cao Jiping. The effect of tropical west Pacific Ocean and tropical east Indian Ocean to the ENSO developing [J]. Progress in Natural Science, 2001, 11(12): 1 293 - 1 300.

[5] Li Chongyin, Mu Mingquan. The dipole type oscillation of the sea temperature in the equatorial Indian Ocean [J]. Chinese Journal of Atmospheric Sciences, 2001, 25(4): 433 - 443.

[6] Li Chongyin, Mu Mingquan, Pan Jing. The sea temperature dipole of the Indian Ocean and the sea temperature abnormal of the Pacific Ocean [J]. Chinese Science Bulletin, 2001, 46(20): 1 747 - 1 751.

[7] Qian Haifeng, Yin Yonghong, Ni Runqi. The dipole mode of the Indian Ocean on the surface layer and its diagnostic analysis for the process of 1997/1998 [J]. Journal of Applied Meteorological Science, 2003, 14(2): 129 - 139.

[8] Saji H N, Goswami B N, Vinayachandran P N, et al. A dipole mode in the tropical Indian Ocean [J]. Natrue, 1999, 401: 360 - 363.

[9] Stefan Hastenrath. Dipoles, temperature gradients, and tropical climate anomalies. Bulletin of the American Meteorological Society, 2002, 83(5): 735 - 738.

[10] Tan Yanke, Zhang Renhe, He Jinhai, et al. The annual variation of sea temperature in the tropical Indian Ocean and the ENSO [J]. Acta Meteor. Sinica, 2004, 62(6): 831 - 840.

[11] Webster P J, Moore A, Loschinigg J, et al. Coupled ocean-atmosphere dynamics in the Indian Ocean [J]. Nature, 1999, 401: 356 - 360.

热带印度洋海温异常与ENSO关系的进一步研究

蔡 怡，李 海

（国家海洋环境预报中心，北京 100081）

摘 要：用 1955 年 1 月 — 2001 年 12 月美国 Scripps 海洋研究所的海温再分析资料、美国 NCEP 再分析资料和美国气候预测中心(CPC) 资料，讨论了热带太平洋 ENSO 与热带印度洋海温距平以及与印度洋偶极子(Dipole) 的关系，研究结果发现：在垂直最大温度距平曲面(MTAL) 上，热带印度洋海温距平分布

存在着与热带太平洋 ENSO 密切相关的 Dipole 现象，其中最大的相关在太平洋 ENSO 超前印度洋 Dipole 一个月。但是，热带印度洋 Dipole 的分布与 Saij 定义的位置略有不同，为东北西南向，它们分别在 6°S — 10°S、65°E — 75°E（西印度洋）和 2°N — 6°N、85°E — 95°E（东印度洋），它是赤道印度洋的一个主要海温距平系统。另外，在热带印度洋东北部与 ENSO 相关的海温距平是一个上下不一致的系统，该海温距平并没有伸展到海面，从海面到20 m — 50 m 的浅薄水层，则为与赤道西南印度洋相同符号的海温距平分布。因此在海面，海温距平不存在与 ENSO 有关的 Dipole 现象，赤道印度洋 Dipole 只存在于次表层以下，这是赤道印度洋 Dipole 与 ENSO 不同之处。这种赤道东北印度洋表层与赤道西南印度洋表层同符号的海温距平现象，有可能是海气热力过程如感热过程造成的。热带印度洋 Dipole 的周期要小于El Nino3，一般为1a — 6 a。

关键词：太平洋ENSO；印度洋Dipole；海洋垂直最大海温距平曲面(MTAL)；EOF分析

Study on the Meso-scale process of the Kuroshio front to the east of Taiwan

WANG Qi, LI Wei, MA Ji-rui, HAN Gui-jun, ZHANG Xue-feng

National Marine Data and Information Service, State Oceanic Administration, Tianjin 300171, *China*

Abstract: By using the reanalysis data, the impact of oceanic eddies and frontal wave on Kuroshio front to the east of Taiwan (KFETW) is studied. The result indicates that cold eddies (warm eddies) corresponding to the first baroclinic mode of Rossby wave can weaken (strengthen) the strength of the KFETW and narrow (widen) the width of this front. A frontal wave of the KFETW during January to February in 1991 is detected from the reanalysis data. And the trough (crest) of the frontal wave may weaken (strengthen) the strength of the KFETW and narrow (widen) the width and thickness of this front. It is found through the diagnostic analysis of the energy source of the frontal wave that the contribution of barotropic instability or that of baroclinic instability is more than that of Kelvin-Helmholtz (K-H) instability by 1 - 2 order of magnitude, and the contribution of the baroclinic instability is 5 times than that of the barotropic instability, thereby the frontal wave is basically driven by the baroclinic instability.

Keyword: Kuroshio front, the east of Taiwan, reanalysis, oceanic eddy, frontal wave

1 Introduction

Kuroshio front, the marginal front of west boundary current, has great scientific significance in research. In addition, the position of the fishing ground has close relationship with that of Kuroshio front, and the sound speed difference between the two sides of Kuroshio front has influence on sound propagation in water, so the research on Kuroshio front is applicable in the national economy and military affairs. Therefore Kuroshio front has always been the hot research subject for the domestic and overseas oceanographer. However due to the lack of long term continuous section observation of Kuroshio to the east of Taiwan, the research on Kuroshio front to the east of Taiwan (KFETW) is still rare to the present. By using the ocean reanalysis, Li et al. (2010) discussed temporal and special multi-scale variation of KFETW, and analyzed the influence of Kuroshio and upwelling on KFETW. But they didn't study the influence of the meso-scale process on the KFETW.

Received on March 5, 2011

Corresponding author: qiqi_ada@yahoo.cn

Based on the reanalysis data from above mentioned in Li et al. (2010) and through the case study, this paper discussed the influence of oceanic eddy on the KFETW, and studied one frontal wave of KFETW and analyzed the energy source of such frontal wave and its effects on KFETW. In order to reach complete and definite description, section 2 of this paper briefly described the reanalysis process of Li et al.(2010), and section 3 discussed the influence of oceanic eddy and frontal wave on KFETW, and the conclusion was made in section 4.

2 Reanalysis of KFETW

Three elements of ocean reanalysis include ocean dynamic model, observation data and ocean data assimilation. These three elements applied in the ocean reanalysis by Li et al. (2010) [1] are reviewed as follows.

2.1 Numerical model configuration

The applied ocean dynamic model is Princeton Ocean Model of the general coordination system (POMgcs in brief. Mellor et al., 2002; Ezer and Mellor, 2004) [2, 3], and the model extent is 99°E - 142°E, 10°S~41°N, applying horizontal variant grid with the horizontal resolution from 1/2° through 1/4°and 1/6°, and in the range of 117°E~130°E, 19°N - 33°N, it changes to 1/8°. The resolution of Kuroshio is the highest (1/8°). Referring to Mellor et al. (2002) [2], the hybrid coordination of z and σ coordinates is applied when POMgcs is used. The maximum model depth reaches 5 035 m.

Reanalysis time period by Li et al. (2010) [1] is from Jan. 1, 1986 to Dec. 31, 2005, lasting 20 years. Monthly average temperature and salinity (T-S) were applied in the first-guess fields of reanalysis data assimilation. The corresponding surface height field was directly from Estimating the Circulation and Climate of the Ocean product (ECCO), and the corresponding velocity was set to zero, making the running model gradually generating the flow field matching with temperature and salinity fields. The above mentioned first-guess fields of surface height, temperature, salinity and current were put into POMgcs. After being integrated for 40 years the model runs stable; then 6-year assimilation was made by using temperature and salinity observations, and the result were taken as the initial field of ocean reanalysis. Open boundary conditions applied monthly average sea surface height, temperature, salinity and current field of SODA product (Simple Ocean Data Assimilation). The wind field of meteorological driving force was the merging field of QuikSCAT (Quick Scatterometer) and reanalysis wind field of NCEP product (National Centers of Environmental Prediction), and the thermal flux field was directly from reanalysis results of NCEP.

2.2 Data for assimilation and quality control

Ocean observation data assimilated into ocean reanalysis system include Nansen cast, CTD, various BT and Argo temperature and salinity profile observation data, multi-source satellite altimetry sea surface height anomaly and satellite remote sensing sea surface temperature. The in situ temperature and salinity observation data were under strict quality control, and in specialty, the salinity drifting was corrected for Argo observation data by using the method developed by Wong et al. (2003).

2.3 Ocean data assimilation

Ocean data assimilation system was formed based on the multi-grid 3-dimensional variational (3D-Var) data assimilation scheme. The basic idea of this data assimilation scheme can be referred to Li et al. (2008) [5]. Referring to the salinity consistency modification scheme of Troccoli et al. (2002) [6], the salinity was under consistency revision during the process of assimilating the temperature. Based on the research by Zhu and Yan (2006) [7], satellite altimetry sea surface height anomaly data assimilation scheme was modified by introducing nonlinear temperature and salinity relationship of model as strong restriction conditions. Detailed practice of above mentioned data assimilation can be referred to Li (2008) [8].

3 Influence of meso-scale process on KFETW

Based on the reanalysis data from Li et al. (2010) [1]and through case study, this part discusses the impact of oceanic eddy on KFETW and researches on one frontal wave of KFETW, and analyzes energy source of this frontal wave and its influence on this front.

3.1 Influence of oceanic eddy on KFETW

In the oceanic eddies corresponding to the first baroclinic mode of Rossby wave, cyclonic eddy is usually related to the upper convexity of isotherm of thermocline, which leads the center of eddy present cold core, thereby cold eddy in brief, while anti-cyclonic eddy is usually related to the lower concave of isotherm of thermocline, which leads the center of eddy present warm core, thereby warm eddy in brief. The west side of KFETW (the east side of Taiwan) has cold water, and the east side has warm water, therefore, in the process of oceanic eddy moving from east to west and arriving in the area of KFETW, cyclonic eddy (cold eddy) can make the warm water side of thermal front be with falling temperature, thus decreasing the temperature difference between two sides of thermal front, and reducing the strength of thermal front; to the contrary, anti-cyclonic eddy (warm

eddy) can make the warm water side of thermal front be with rising temperature, thus increasing the temperature difference between two sides of thermal front, and improving the strength of thermal front. Fig. 1 shows the condense spectrum between relative vorticity at the levels of 150 m, 200 m, 250 m and 300m to the east of Taiwan derived from the reanalysis result in this study and corresponding strengths of KFETW at the same levels. In the period above 30d, the correlation coefficients of the periods of 55d, 77d, 85d, 93d can exceed 0.7. It's worth to note that the values of phase cross-spectrum on the above periods are about 180°, which indicates that there is anti-phasic relationship between relative vorticity and thermal front strength at these periods, that is, its correlation is negative. Thus cyclonic eddy (cold eddy) reduces thermal front strength, and anti-cyclonic eddy (warm eddy) rises thermal front strength.

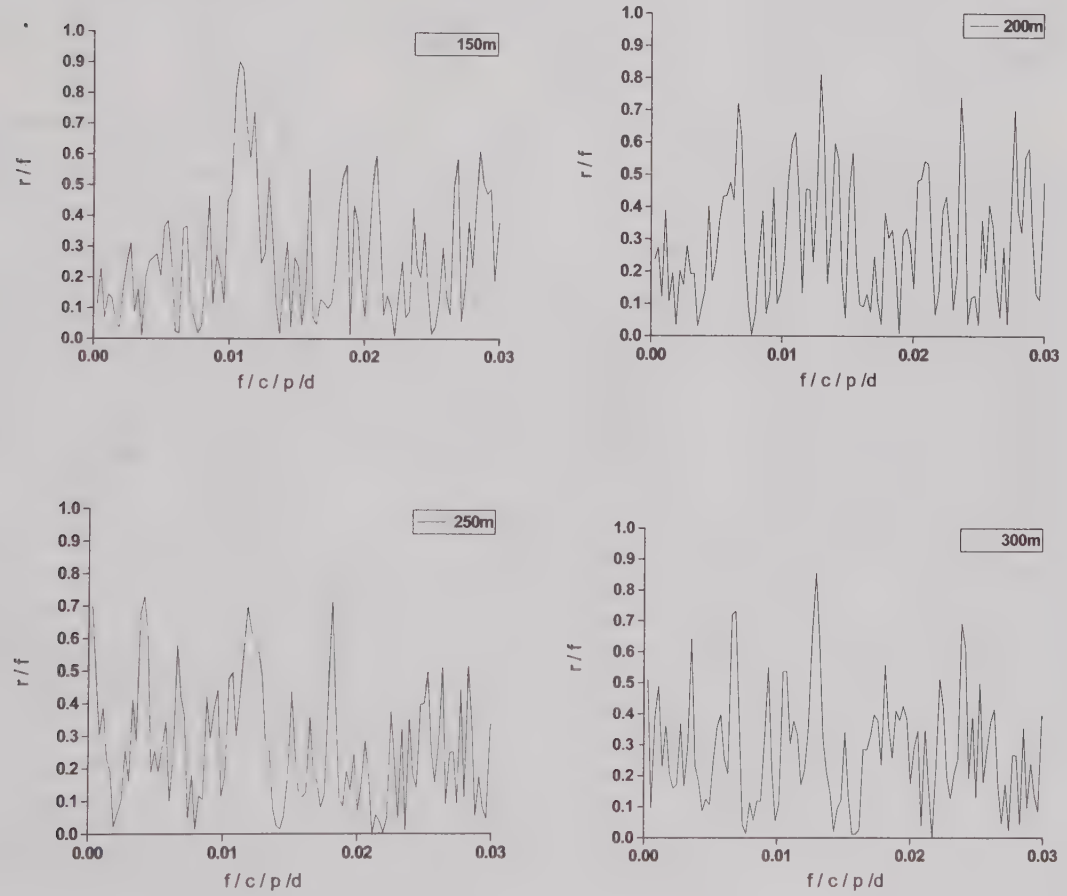

Fig. 1 Condense spectrum between relative vorticity at the levels of 150 m, 200 m, 250 m and 300 m to the east of Taiwan derived from the reanalysis result in this study and corresponding strengths of KFETW at the same levels.

For illustrating the impact of oceanic eddy on KFETW, the case for explaining the impacts of cold eddy and warm eddy on this front was chosen from the reanalysis results. Fig. 2 shows the cold eddy during August to September of 1997 and corresponding variation process of corresponding KFETW. The moving velocity of this cold eddy was about 7.1 cm/s. As the figure on Aug. 13, 1997 shows, before the cold eddy met with this front, the corresponding front strength is 0.070 °C/km, with the breadth of 30.2 km, and the thickness of 240 m, distributing between the water level of 20 m - 260 m. Also as the figure on Sep.17, 1997 shows, when the cold eddy met with this front, the right side temperature of Kuroshio descended and isotherm rose up, at the same time, this front strength weakened to 0.059 °C/km, and the width 21.7 km, the thickness 100 m, being at the water level of 150 m - 250 m, and the horizontal position of the northern end of this front diverted about 20.4 km to the east, and the horizontal position of the southern end of this front diverted about 9.3 km to the east. Thereafter this cold eddy gradually weakened, and this front came back to the former status.

Fig. 3 shows the warm eddy during May to June of 1997 and the variation process of corresponding KFETW. The moving velocity of this warm eddy was about 7.2 cm/s. As the figure on May 14, 1997 shows, before the warm eddy met with this front, the corresponding front strength is 0.070 °C/km with the breadth of 39.6 km, and the thickness of 310 m, distributing between the water level of 20 m - 350 m. Also as the figure on June 11, 1997 shows, when the warm eddy met with this front, from the section figure, the right side temperature of Kuroshio rose and isotherm descended, at the same time, this front strength rose to 0.081 °C/km, and the width 60.4km, the thickness 270 m, being at the water level of 50 m - 350 m.

In conclusion, cold eddy (warm eddy) generated by the first baroclinic mode of Rossby wave can reduce (increase) the right side water temperature of KFETW, weaken (strengthen) two side temperatures difference of this front, weaken (strengthen) the strength of the KFETW and narrow (widen) the width of this front. However the impacts on the thickness and depth of this front depend on the influential depth of oceanic eddy.

3.2 Frontal wave of KFETW and its mechanism

Sugimoto et al. (1988) [9] once stated that fluctuant period of East China Sea Kuroshio meander was about 11 - 14 days, and the wave lengthen was nearly 300 - 350 km, and phase speed was 30 cm/s. Qiu et al. (1990) [10] pointed out that the typical period of Kuroshio meander was 14 - 20 days, and the wave lengthen was 100 - 150 km, and phase speed was nearly 20 - 26 cm/s. In the reanalysis of this paper, one Kuroshio frontal wave to the east of Taiwan during Jan. to Feb. of 1991 was got, and this frontal wave propagated

northward from Luzon Strait to the north to the northeast of Taiwan, and corresponding Kuroshio had some changes. As figure 4 shows, on Jan. 25, 1991 when there was no oceanic eddy intruding at the east side of Kuroshio, both sea surface height contour line and 200m level isotherm at the southeast of Taiwan Island had the trend of eastward bending, which reached northward to 23.5°N on Jan. 31, and then reached northward to the northeast of Taiwan on Feb. 6.

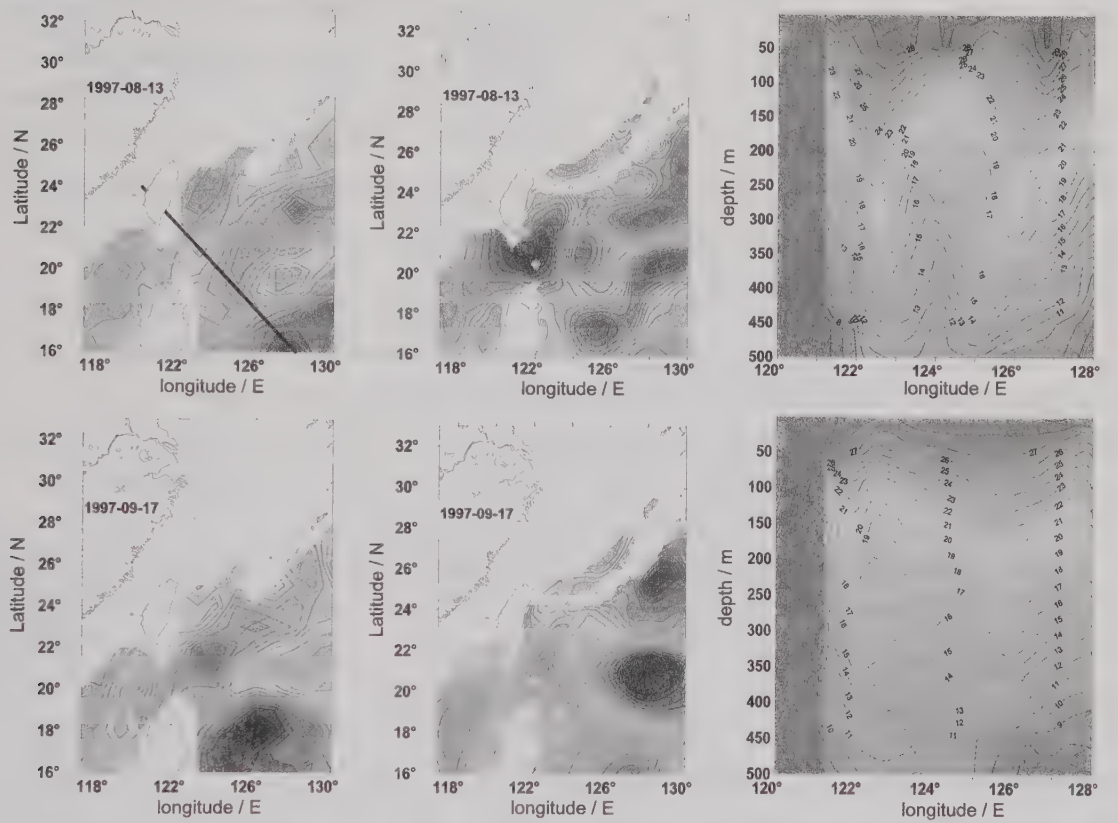

Fig. 2 Influence of cyclonic eddy (cold eddy) on KFETW

(Three upper figures show the results on Aug. 13, 1997, among which the left one is satellite altimetry sea surface height anomaly (unit: m), and the middle one is reanalysis sea surface height anomaly (unit: m), and the right one is reanalysis section temperature (the location of the section is indicated by upper left figure, unit: °C). Three lower maps show the results on Sep. 17, 1997, which have the same indication as three upper figures. Blue represents negative anomaly, and red represents positive anomaly, and the broken line is zero value; the interval of sea surface height anomaly isolines is 0.05m, and only areas with depths of more than 1 000 m are drawn.)

For researching the propagation of this frontal wave, the reanalysis sea surface height field and temperature field at the level of 200 m from Jan. 16 to Feb. 15 1991 were averaged, and the anomaly field was derived by deducting the average field from the reanalysis sea surface height field and temperature field at the level of 200m on different

date of the same period, and Figure 5 shows the corresponding anomaly field. Negative anomaly corresponded to wave trough, and positive one was related to wave crest. As figure shows, wave trough on Jan. 16, 1991, generated from Luzon Strait, and propagated northward along with Kuroshio, and at the same time, the temperature section still maintained the normal level. On Jan. 25, a wave crest followed with this wave trough. From Jan. 31 to Feb. 3, when the wave trough was to the east of Taiwan, the east side isotherm of temperature section rose up, thereby two-side temperature gradients of Kuroshio decreased and this front strength weakened; then the wave trough continued to propagate northward, and on Feb. 9, it dissipated at the northeast of Taiwan, and the eastern sea area was gradually prevailed by wave crest, and the eastern isotherm of temperature section descended, and this temperature front gradually strengthened and came back to the normal level. The wavelength of this frontal wave was about 244 km, and phase speed was about 28cm/s, and period was 15 days.

For researching the contribution of different instabilities to frontal wave, in Samelson (1993) [11], under the hydrostatic approximation，linearized primitive equations satisfied by disturbance were used to research the contribution of barotropic instability, Kelvin-Helmholtz (K-H) instability and baroclinic instability to harassing energy. Basic state was geostrophic, satisfying thermal-wind relation, and current velocity only had north component, not changing with latitude. Based on the research of Samelson (1993) [11], in this paper, equations satisfied by basic state were extended to the nonlinear equations only neglecting local changes, and equations satisfied by disturbance state were derived in this paper. Referring to Samelson （1993）[11], it was set that $b = -\frac{g}{\rho_0}\rho'$, $B = -\frac{g}{\rho_0}\overline{\rho}$, where ρ' is disturbance density, $\overline{\rho}$ density of basic state, ρ_0 reference density, and the equations satisfied by basic state are as follows:

$$\begin{cases} U\dfrac{\partial U}{\partial x}+V\dfrac{\partial U}{\partial y}+W\dfrac{\partial U}{\partial z}-fV=-\dfrac{1}{\rho_0}\dfrac{\partial P}{\partial x} \\ U\dfrac{\partial V}{\partial x}+V\dfrac{\partial V}{\partial y}+W\dfrac{\partial V}{\partial z}+fU=-\dfrac{1}{\rho_0}\dfrac{\partial P}{\partial y} \\ \dfrac{\partial U}{\partial x}+\dfrac{\partial V}{\partial y}+\dfrac{\partial W}{\partial z}=0 \\ 0=-\dfrac{1}{\rho_0}\dfrac{\partial P}{\partial z}+B \\ U\dfrac{\partial B}{\partial x}+V\dfrac{\partial B}{\partial y}+W\dfrac{\partial B}{\partial z}=0 \end{cases} \quad (1)$$

The equations satisfied by disturbance state are as follows:

$$\begin{cases} \dfrac{\partial u}{\partial t}+U\dfrac{\partial u}{\partial x}+u\dfrac{\partial U}{\partial x}+V\dfrac{\partial u}{\partial y}+v\dfrac{\partial U}{\partial y}+W\dfrac{\partial u}{\partial z}+w\dfrac{\partial U}{\partial z}-fv=-\dfrac{1}{\rho_0}\dfrac{\partial p}{\partial x} \\ \dfrac{\partial v}{\partial t}+U\dfrac{\partial v}{\partial x}+u\dfrac{\partial V}{\partial x}+V\dfrac{\partial v}{\partial y}+v\dfrac{\partial V}{\partial y}+W\dfrac{\partial v}{\partial z}+w\dfrac{\partial V}{\partial z}+fu=-\dfrac{1}{\rho_0}\dfrac{\partial p}{\partial y} \\ \dfrac{\partial u}{\partial x}+\dfrac{\partial v}{\partial y}+\dfrac{\partial w}{\partial z}=0 \\ 0=-\dfrac{1}{\rho_0}\dfrac{\partial p}{\partial z}+b \\ \dfrac{\partial b}{\partial t}+U\dfrac{\partial b}{\partial x}+u\dfrac{\partial B}{\partial x}+V\dfrac{\partial b}{\partial y}+v\dfrac{\partial B}{\partial y}+W\dfrac{\partial b}{\partial z}+w\dfrac{\partial B}{\partial z}=0 \end{cases} \tag{2}$$

So the equation satisfied by disturbance state energy is as follows:

$$\begin{aligned} \frac{d}{dt}\int\frac{1}{2}\rho_0\left(u^2+v^2+\frac{b^2}{B_z}\right)d\Omega=&-\int\rho_0\left(\frac{\partial U}{\partial x}u^2+\frac{\partial V}{\partial x}uv+\frac{\partial U}{\partial y}uv+\frac{\partial V}{\partial y}v^2\right)d\Omega \\ &-\int\rho_0\left(\frac{\partial U}{\partial z}uw+\frac{\partial V}{\partial z}vw\right)d\Omega \\ &-\int\rho_0\left(\frac{\partial B}{\partial x}\left(\frac{\partial B}{\partial z}\right)^{-1}ub+\frac{\partial B}{\partial y}\left(\frac{\partial B}{\partial z}\right)^{-1}vb\right)d\Omega \end{aligned} \tag{3}$$

where the first element to the right side represents contribution of barotropic instability and the second one is that of K-H instability, and the third one represents that of baroclinic instability.

Through applying the derived formula (3) to the above mentioned frontal wave (one Kuroshio frontal wave to the east of Taiwan during Jan. to Feb. 1991), it is found that the contribution of barotropic instability or that of baroclinic instability is more than that of K-H instability by 1~2 order of magnitude, and the contribution of the baroclinic instability is 5 times than that of the barotropic instability. When this front wave moved to the east of Taiwan on Feb.3 1991, the contribution of the baroclinic instability is $7.5\times10^8 W$.Thereby the frontal wave is mainly driven by the baroclinic instability.

At the same period, the flux of Kuroshio to the east of Taiwan, taking 700m as the reference level and the section being from (121.5°E, 24.5°N) to (124.0°E, 24.5°N), decreased from 30Sv on Jan. 16, 1991 to 24Sv on Jan. 31,1991, and came back to 26Sv on Feb. 15 with the variation range of 6Sv. The corresponding KFETW strength weakened from 0.075 °C/km to 0.068 °C/km, and came back to 0.073 °C/km; and width decreased from 41.5 km to 37.4 km, and came back to 50.2 km; and thickness decreased from 300 m to 160 m, and came back to 260m.

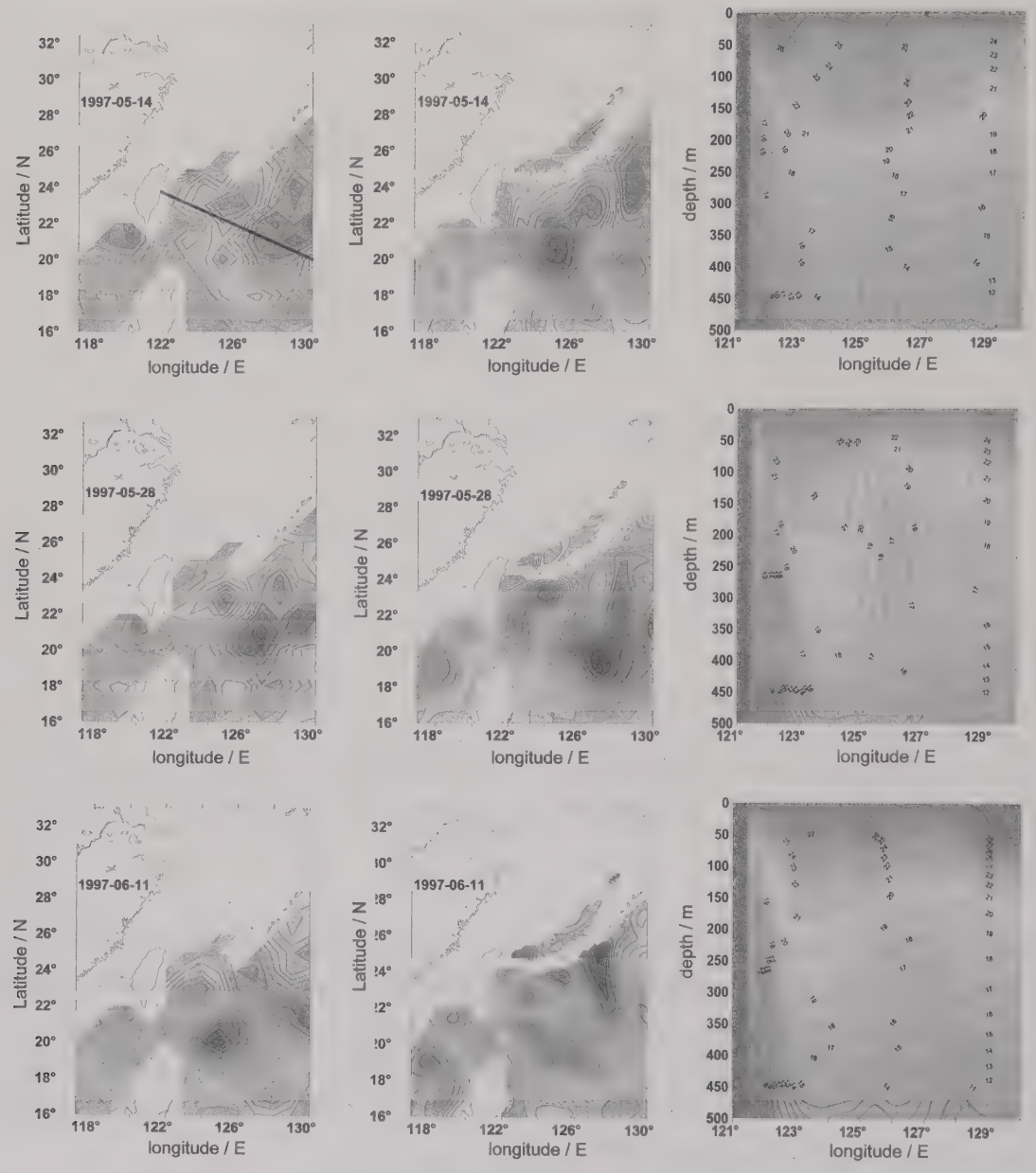

Fig. 3 Influence of anti-cyclonic eddy (warm eddy) on KFETW

(Three upper figures show the results on May 14, 1997, among which the left one is satellite altimetry sea surface height anomaly (unit: m), and the middle one is reanalysis sea surface height anomaly (unit: m), and the right one is reanalysis section temperature (the location of the section is indicated by upper left figure, unit: °C). Three middle figures show the results on May 28, 1997, which have the same indication as three upper figures. Three lower figures show the results on June 11, 1997, which have the same indication as above figures. Blue represents negative anomaly, and red represents positive anomaly, and the broken line is zero value; the interval of sea surface height anomaly isolines is 0.05m, and only areas with depths of more than 1 000 m are drawn.)

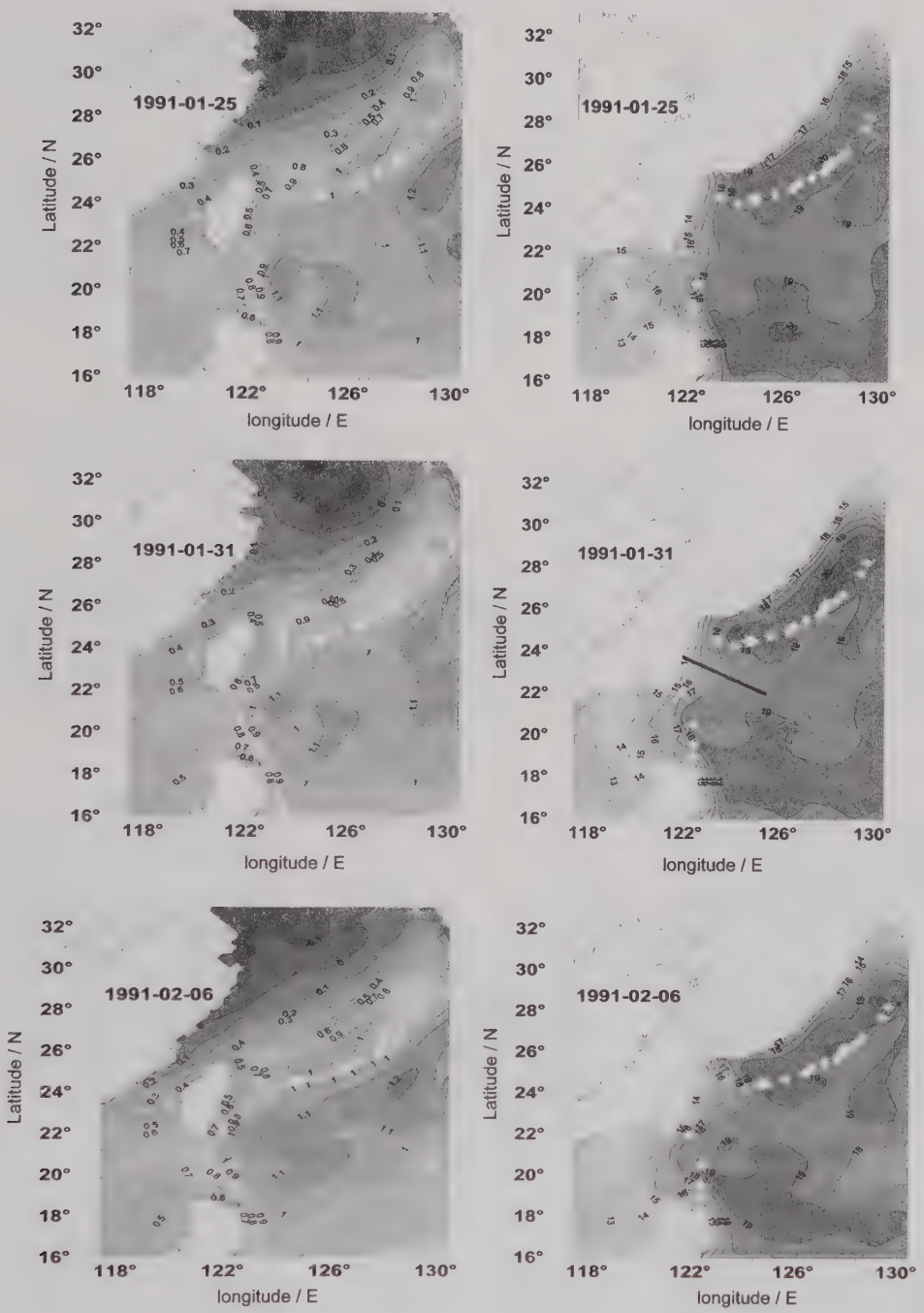

Fig. 4 Frontal wave of KFETW from January to February of 1991 based on the reanalysis results.

The upper figures show the results on Jan. 15, 1991, among which the left one is sea surface height (unit: m), and the right one is water temperature at 200m (unit: °C). The middle figures show the results on Jan. 31, 1991, which have the same indication as the upper maps. The lower figures show the results on Feb. 6, 1991, which have the same indication as above figures.

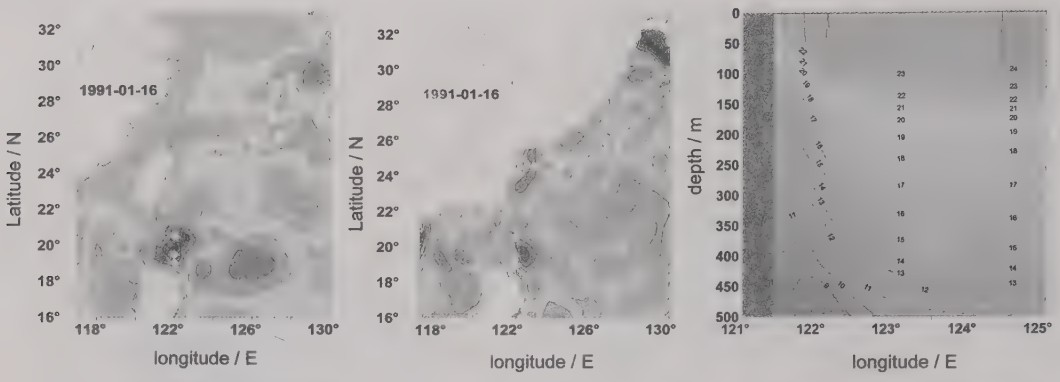
1991-01-16
Latitude / N
longitude / E
1991-01-16
Latitude / N
longitude / E
depth / m
longitude / E

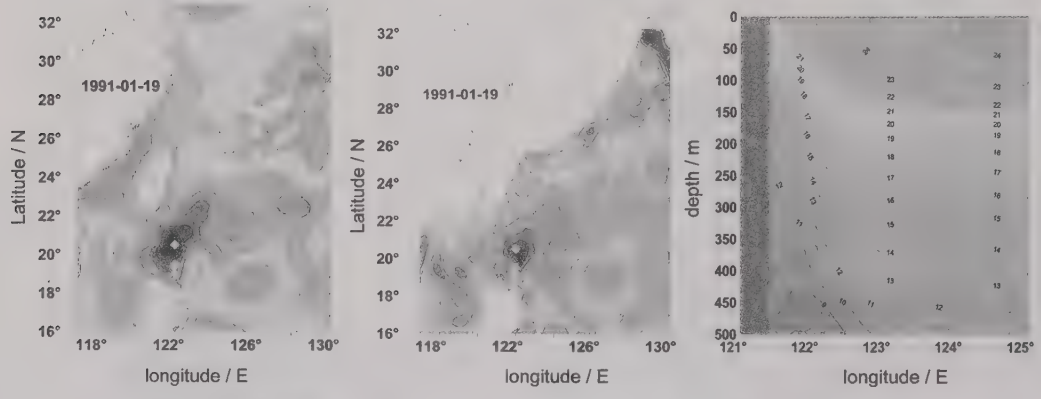
1991-01-19
Latitude / N
longitude / E
1991-01-19
Latitude / N
longitude / E
depth / m
longitude / E

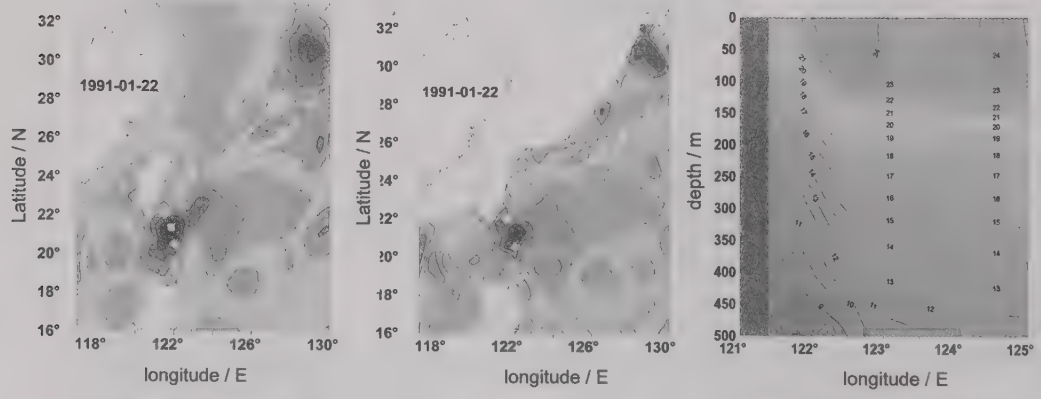
1991-01-22
Latitude / N
longitude / E
1991-01-22
Latitude / N
longitude / E
depth / m
longitude / E

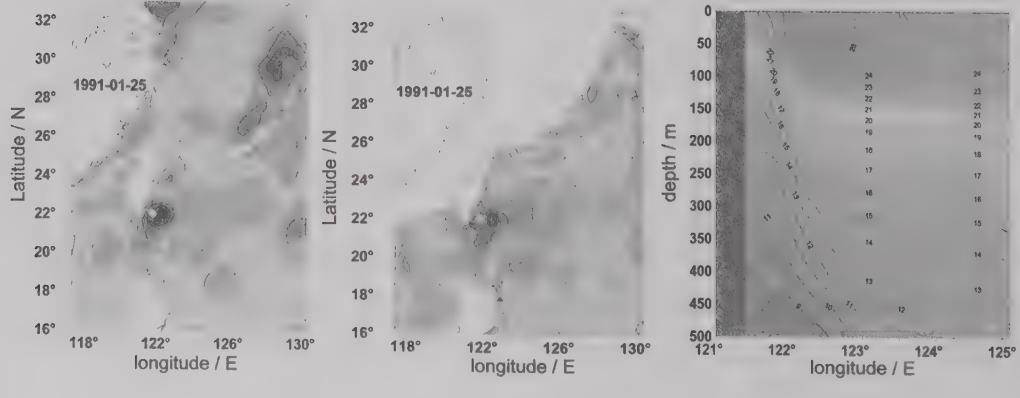
1991-01-25
Latitude / N
longitude / E
1991-01-25
Latitude / N
longitude / E
depth / m
longitude / E

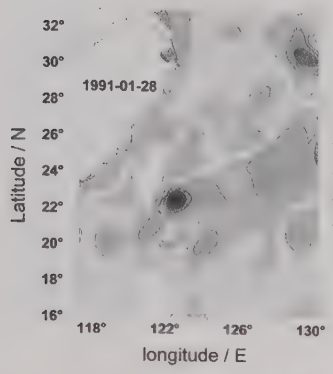
1991-01-28
Latitude / N
longitude / E

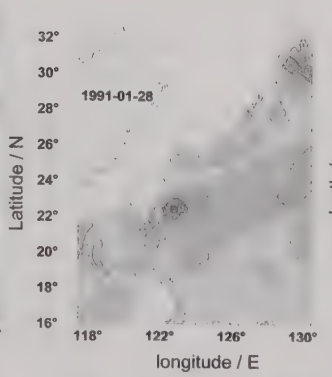
1991-01-28
Latitude / N
longitude / E

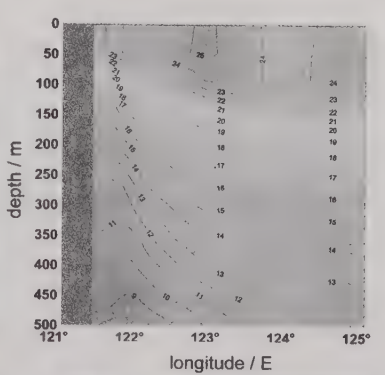
depth / m
longitude / E

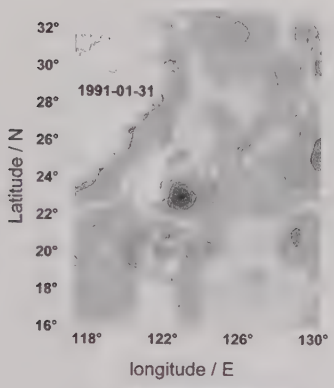
1991-01-31
Latitude / N
longitude / E

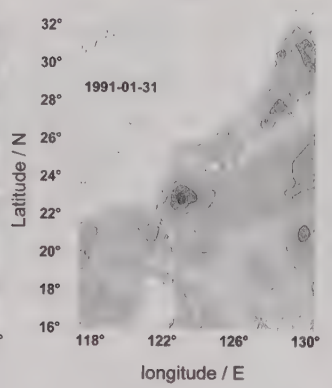
1991-01-31
Latitude / N
longitude / E

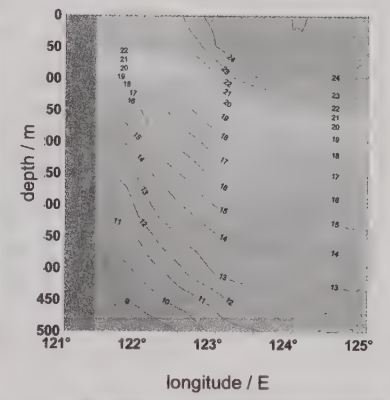
depth / m
longitude / E

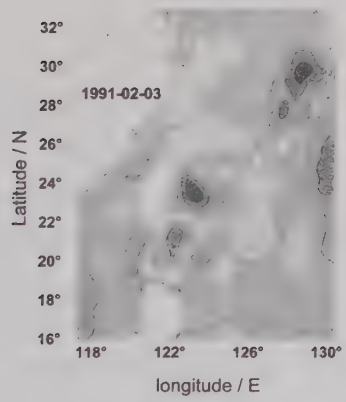
1991-02-03
Latitude / N
longitude / E

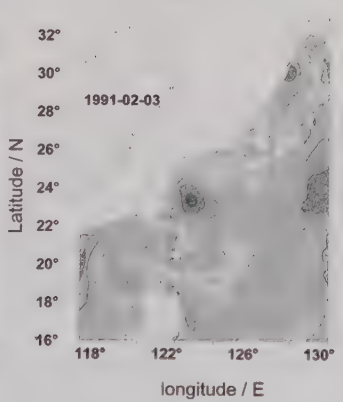
1991-02-03
Latitude / N
longitude / E

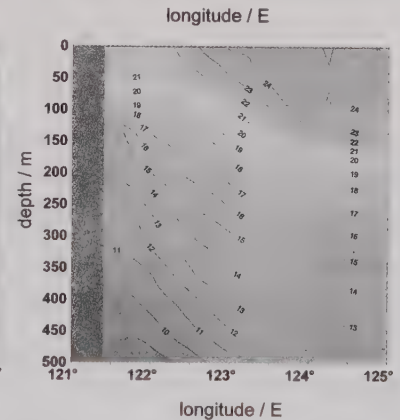
depth / m
longitude / E

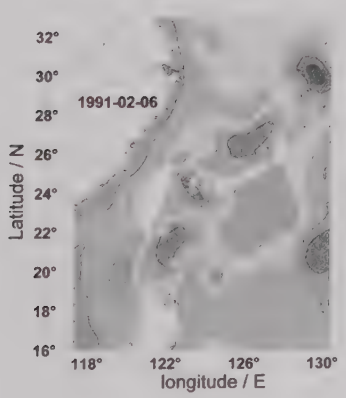
1991-02-06
Latitude / N
longitude / E

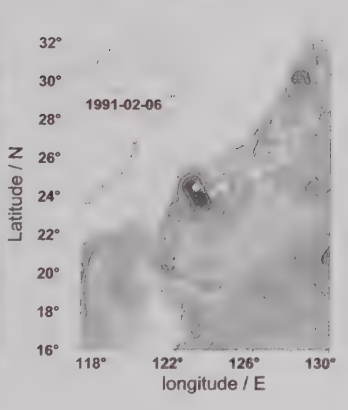
1991-02-06
Latitude / N
longitude / E

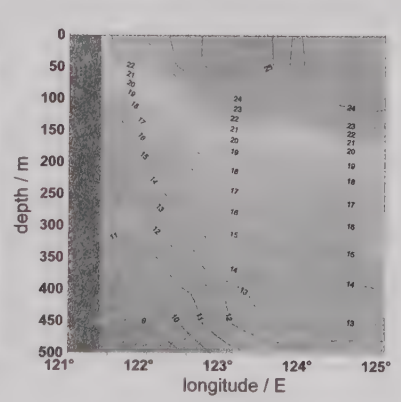
depth / m
longitude / E

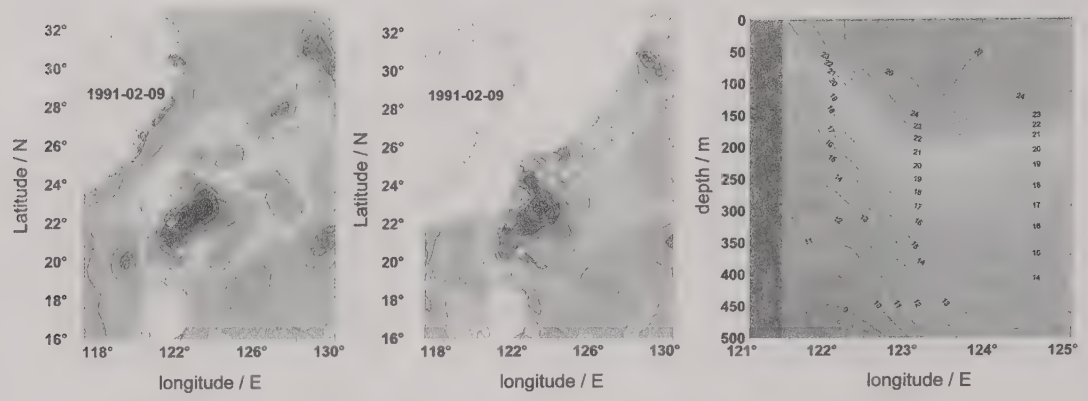

Fig. 5 Frontal wave propagation of KFETW from January to February of 1991 based on the reanalysis results

(The time has been indicated in the figure. The left one is sea surface height anomaly (unit: m), and the middle one is water temperature anomaly at the level of 200 m (unit: °C), and the right one is corresponding section temperature (the location of the section is indicated in Fig. 4, unit: °C). Blue represents negative anomaly, and red represents positive anomaly, and the broken line is zero value; the interval of sea surface height anomaly isolines is 0.05 m, and only areas with depths of more than 1 000 m). are drawn.

4 Conclusion

In this paper, reanalysis was used to study the influence of oceanic eddy and frontal wave on KFETW. This paper takes two cases for discussing the effects of cold eddy and warm eddy on the strength, width, thickness and other features of this thermal front. The result indicates that cold eddies (warm eddies) corresponding to the first baroclinic mode of Rossby wave can reduce (rise) the right side water temperature of KFETW, decrease (increase) temperature gradient of two sides of this front, thus weaken (strengthen) the strength of the KFETW and narrow (widen) the width of this front. However their effects on the front thickness and depth depend on the influential depth of ocean eddy.

One Kuroshio frontal wave was got in the reanalysis process of this paper. It is found through the diagnostic analysis of the energy source of the frontal wave that the contribution of barotropic instability or that of baroclinic instability is more than that of K-H instability by 1 - 2 order of magnitude, and the contribution of the baroclinic instability is 5 times than that of the barotropic instability, thereby the frontal wave is basically driven by the baroclinic instability. When the wave trough (ridge) of frontal wave arrives, the strength of this thermal front weakens (strengthens), and width and thickness decrease (increase).

Reference

[1] Li Wei, Ma Jirui, Han Guijun, et al. The Kuroshio Front to the East of Taiwan: Seasonal Feature, Variability and Mechanism [J]. Submitted to Journal of Marine Systems, 2010.

[2] Mellor, George, S Hakkinen, et al. A Generalization of a Sigma Coordinate Ocean Model and an Intercomparison of Model Vertical Grids. Ocean Forecasting: Conceptual Basis and Applications. Berlin: N. Pinard, J. Woods (Eds.), Springer, 2002: 55 - 72.

[3] Ezer, Tal, George L, et al. A generalized coordinate ocean model and a comparison of the bottom boundary layer dynamics in terrain-following and in z-level grids [J]. Ocean Modelling, 2004, 6: 379 - 403.

[4] Wong, Annie P S, Gregory C, et al. Delayed-Mode Calibration of Autonomous CTD Profiling Float Salinity Data by $\theta - S$ Climatology. Journal of Atmospheric and Oceanic Technology, 2003, 20: 308 - 318.

[5] Li Wei, Yuanfu Xie, Zhongjie He, et al. Application of the Multi-grid Data Assimilation Scheme to the China Seas' Temperature Forecast [J]. Journal of Atmospheric and Oceanic Technology, 2008, 25(11): 2 106 - 2 116.

[6] Troccoli A, Balmaseda M A, Segschneider J, et al. Salinity adjustments in the presence of temperature data assimilation [J]. Mon. Wea. Rev., 2002., 130: 89 - 102.

[7] Zhu J, C X Yan. Nonlinear balance constraints in 3DVAR data assimilation [J]. Science in China (D), 2006, 49: 331 - 336.

[8] Li W., 2008. Numerical study on Kuroshio front to the east of Taiwan. [doctoral thesis]. Qingdao: Ocean University of China.

[9] Sugimoto T, Kimura F, Miyaji K. Meander of the Kuroshio front and current variability in the East China Sea [J]. J. Oceanogr. Soc. Japan, 1988, 44: 125 - 135.

[10] Qiu B, Toda T, Imasato N. On Kuroshio front fluctuations in the East China Sea using satellite and in situ observational data [J]. J. Geophys. Res., 1990, 95: 18 191 - 18 204.

[11] Samelson R M. Linear instability of a mixed-layer front [J]. J. Geophys. Res., 1993, 98: 10 195 - 10 204.

台湾以东黑潮锋的中尺度过程研究

王 琦，李 威，马继瑞，韩桂军，张学峰

（1. 国家海洋信息中心，天津 300171）

摘 要：采用海洋再分析结果，研究了海洋涡旋和锋面波动对台湾以东黑潮锋的影响，结果表明，Rossby 波第一斜压模态形成的冷涡（暖涡），减弱（增强）台湾以东黑潮温度锋强度，减小（加大）锋的宽度。在再分析结果中，捕获到 1991 年 1 — 2 月台湾以东的一次黑潮锋面波动。锋面波动的波槽（波脊）到达时，该温度锋强度减弱（增强），宽度和厚度减小（增大）。使用诊断公式，初步分析了该锋面波动的能量来源，发现正压不稳定的贡献与斜压不稳定的贡献比 K-H 不稳定大 1～2 个数量级，而斜压不稳定的贡献约为正压不稳定的 5 倍，因此该锋面波动基本上由斜压不稳定性提供能量。

关键词：台湾以东；黑潮锋；再分析；海洋涡旋；锋面波动

Freak wave simulation based on nonlinear model and the research on the time-frequency energy spectrum of simulation results

CUI Cheng, ZHANG Ning-chuan, LI Jing-bo

State Key Laboratory of Coastal and Offshore Engineering, Dalian University of Technology, Dalian 116024, Liaoning Province, China

Abstract: VOF (volume of fluid) method has been used to make the numerical simulation of freak wave come true. The comparisons between the numerical results and linear theoretical results corresponding to Eq.(5) have been carried out to show that the numerical results have a better exhibition of nonlinear characteristics. Wavelet analysis method has been adopted to investigate the time-frequency energy spectrum of simulation freak waves and the results reveal strong nonlinear interaction enables energy to be transferred to high harmonics during the progress of its formation. Varying water depth can enhance the nonlinear interaction, making much more energy be transferred to high harmonics and freak waves with higher asymmetry be generated.

Keywords: freak wave, numerical simulation, wavelet analysis, varying water depth, time-frequency energy spectrum

Introduction

The freak wave is a type of large and transient water wave which can bring serious damage to vessel and maritime structure, as well as to other facilities in the ocean. Although scholars have conducted a certain amount of research on freak wave, the occurrence probability, physical mechanics, especially with regard to the frequency composition and its impact factors are still unclear. The dynamic response of engineering structure can be affected by wave frequency composition. Therefore, the study of the frequency composition and its impact factors carries important theoretical and engineering significance.

After Klinnting and Sand (1987) proposed a widely accepted definition, scholars have put forward a lot of simulation methods to study freak wave. The method, in which deterministic component waves are focused, is used extensively. Kriebel (2000) developed

Received on Apr. 20, 2011

Corresponding author: chengcui1984@163.com

that method and proposed a highly effective dual superposition model. Pei (2007) imitated measured freak waves by using it and the results are satisfying. Zhao (2008) was enlightened and proposed a new superposition model (transient wave train + regular wave train) for freak wave simulation. However, the non-linear interaction can not be explored in-depth with the models mentioned above. Pei (2007) did an experimental investigation in which dual superposition model is used to produce freak wave. Soomere and Engelbrecht (2006) simulated freak wave in shallow water through the interaction of solitary waves. Dyachenko and Zakharov (2005) obtained freak wave by evolving Stokes wave based on the Benjamin-Feir instability. Brandini and Grilli (2001), Fochesato et al. (2007) implemented the numerical simulation of freak wave with Boundary Element Method (BEM) solving fully nonlinear potential flow equations. Although the non-linear characteristics are touched on, the internal structure of freak wave is not mentioned.

Grilli et al. (2001) investigated the numerical simulation phenomenon in which waves overturn and break up over varying topography and discovered that varying water depth could induce wave energy centralization. It indicates that varying water depth will have an impact on freak wave.

The VOF technique is a common method used to track free fluid surfaces and can simulate highly nonlinear wave. Wavelet analysis, a relatively new time-frequency analysis method, can be used to study transient and unstable signal. Lin and Liu (2004) introduced interrelated application to freak wave research. Chien et al. (2002) studied the frequency composition of measured freak wave by wavelet analysis method and discovered that the wavelet spectrum of measured freak wave covered a wide frequency range. Kwona et al.. (2005) also utilized the wavelet analysis method to obtain the wavelet cross-spectral of freak wave and their horizontal impact on cylindrical structure. Although freak wave frequency composition is covered, the influence of metamorphic topography is not touched on.

In this paper, VOF method is used to make the numerical simulation of freak wave come true. This method in which the fully nonlinear N-S equations are solved can take into account the fluid viscosity and nonlinearity. On this basis, wavelet analysis method is used to analyse the freak wave frequency composition and help understand the relationship between the freak wave frequency composition and varying water depth.

2 Governing equations and boundary conditions

2.1 Governing equations

The continuity equation and N-S equations are used as governing equations of VOF

method (Hirt and Nichols, 1981).

Continuity equation:

$$\frac{\partial}{\partial x}(\theta u)+\frac{\partial}{\partial y}(\theta v)=0 \tag{1}$$

N-S equations:

$$\frac{\partial u}{\partial t}+u\frac{\partial u}{\partial x}+v\frac{\partial u}{\partial y}=-\frac{1}{\rho}\frac{\partial p}{\partial x}+g_x+v(\frac{\partial^2 u}{\partial x^2}+\frac{\partial^2 u}{\partial y^2}) \tag{2}$$

$$\frac{\partial v}{\partial t}+u\frac{\partial v}{\partial x}+v\frac{\partial v}{\partial y}=-\frac{1}{\rho}\frac{\partial p}{\partial y}+g_y+v(\frac{\partial^2 v}{\partial x^2}+\frac{\partial^2 v}{\partial y^2}) \tag{3}$$

Where u and v are velocity components in x and y direction, respectively; p is the pressure, ρ the fluid density, υ the coefficient of kinematic viscosity; θ is the parameter of the part cell, the value of which is between 0 and unity.

2.2 Boundary conditions

The free surface is treated by introducing a function F(x, y, t) that is defined to be unity at any point occupied by fluid and 0 elsewhere (Hirt and Nichols, 1981).The time dependence of F is governed by:

$$\frac{\partial F}{\partial t}+\frac{\partial(uF)}{\partial x}+\frac{\partial(vF)}{\partial y}=0 \tag{4}$$

The freak wave can be obtained by the dual superposition model (Kriebel, 2000).

$$\eta(x,t)=\eta_1(x,t)+\eta_2(x,t)$$

$$=\sum_{i=1}^{M}a_{1i}\cos(k_i x-\omega_i t+\varepsilon_i)+\sum_{i=1}^{M}a_{2i}\cos[k_i(x-x_c)-\omega_i(t-t_c)] \tag{5}$$

Where η is the surface elevation at a distance x from the wave generator in the wave tank; M is the number of component wave; k_i and ω_i are the wave number and frequency of the ith component wave, respectively; ε_i is the random wave phase distributed uniformly in the range (0 - 2π); a_{1i} , a_{2i} are the amplitudes of the random and transient waves (80% of the energy went into the random wave while just 20% went into the transient wave); The remaining parameters, x_c and t_c, represent the distance and time at which the transient waves will converge.

From wave-making theory, the horizontal velocity of the wave-maker paddle for freak waves $U_0(t)$ can be written as:

$$U_0(t)=\sum_{i=1}^{M}\frac{\omega_i\eta(t)}{W_i} \tag{6}$$

Here, W_i is the transfer function associated with *ith* component of propagating wave:

$$W_i = \frac{4\sinh^2 k_i d}{\sinh 2k_i d + 2k_i d} \tag{7}$$

To limit the computational domain, an absorbing damping zone is applied on the right end of the channel to absorb the outgoing waves and on the other end of the channel, and an absorbing wave-maker boundary is set to cancel out the reflected wave that reaches the numerical paddle (Wang, 1995).

3 Nonlinear model-based for freak wave's occurrence

3.1 Performance proof of numerical tank

The computation region is shown in Fig. 1. A mesh of 1 200 cells in the *x*-direction and 30 cells in the *y*-direction are used, and the spatial increment is dx = 5 cm in *x* direction and dy = 3 cm in *y* direction. The water depth d = 50 cm. The wave gauge is placed at the station 2 002.5 cm (more than 6 times of significant wavelength) away from the wave-maker. The computing time is 200s, and the time step dt = 0.02s. The water density ρ = 1 g/cm^3, and the gravitational acceleration g = 980 cm/s^2, the kinematic viscosity υ = 0.010 02 cm^2/s, and the modified PM spectrum (ITTC, 1972) is chosen as the incident wave spectrum and is expressed by Eqs.(8) - (10). Fig. 2 (1) and (2) show the excellent comparisons of the target and the simulated irregular wave profiles as well as their Fourier spectrums.

$$S(f) = Af^{-5}\exp(-Bf^{-4}) \tag{8}$$

$$A = 0.0177 H_s{}^2 T_{0.1}{}^{-4} \tag{9}$$

$$B = 0.4443 T_{0.1}{}^{-4} \tag{10}$$

A freak wave is also simulated in the numerical tank as an example in order to prove the effectiveness of freak wave simulation. The simulated results are shown in Fig. 3. It is obtained that a freak wave which is in accordance with the definition that its height should exceed the significant wave height, wave height before and after it in 2 times ($\alpha_1 = H_j / H_s > 2$, $\alpha_2 = H_j / H_{j-1} > 2$, $\alpha_3 = H_j / H_{j+1} > 2$) , and its crest height should exceed 65% of its wave height ($\alpha_4 = \eta_j / H_j > 0.65$).

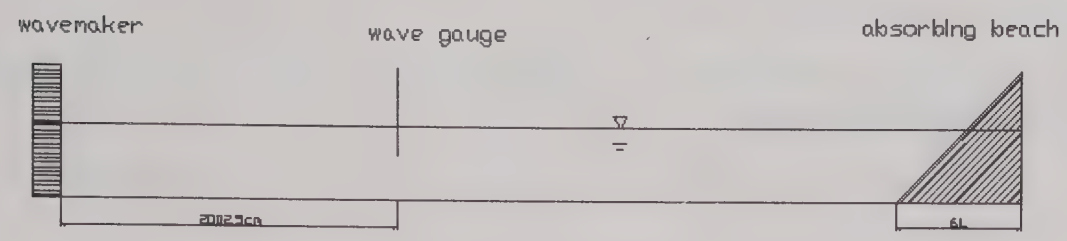

Fig. 1 Sketch of the computation domain (unit / cm)

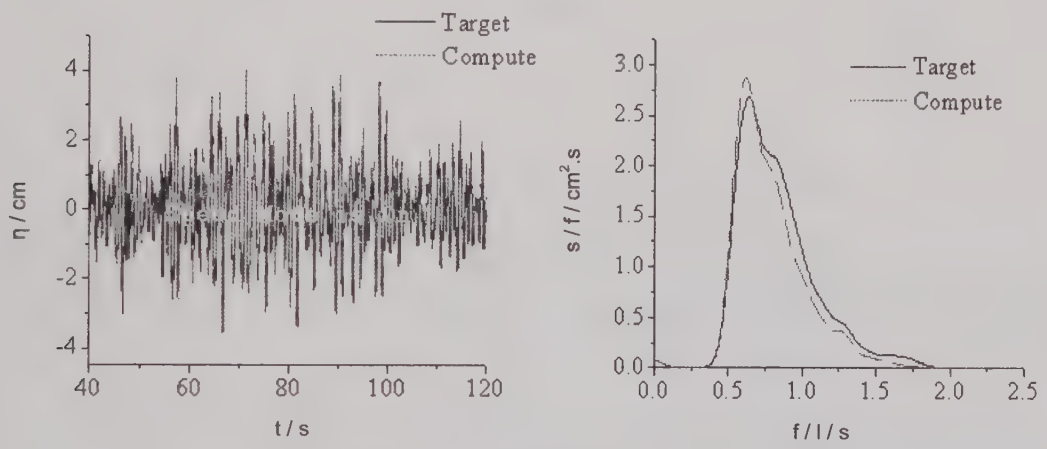

Fig. 2 Comparison of target wave surface elevation and computed wave surface elevation (left) as well as comparison of target spectrum and computed spectrum (right) (H_s = 5 cm, T_p = 1.5 s)

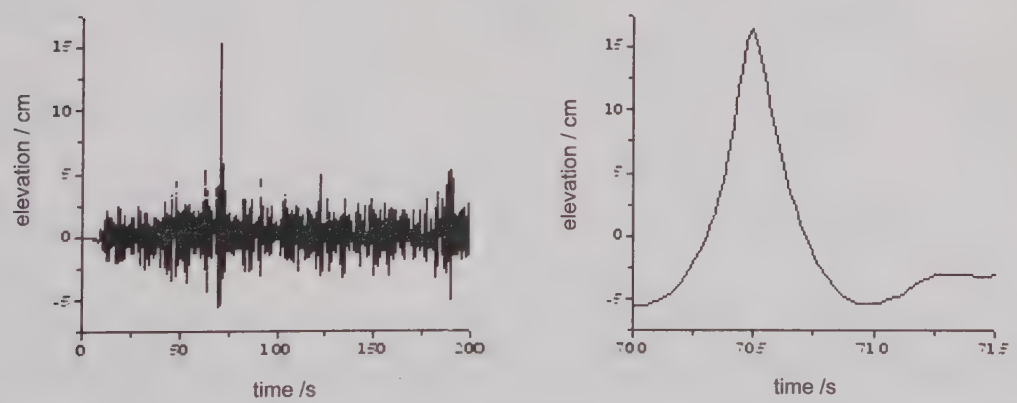

Fig. 3 Simulated freak wave (left) as well as instantaneous wave profile at selected instance (right)

(α_1=3.72, α_2=2.28, α_3=2.90, α_4=0.75)

It is seen that our numerical method can not only well model a common random wave train but also model a freak wave.

3.2 Comparison of the nonlinear results (model in this paper) and linear results (dual superposition model)

The incident wave conditions for three cases, listed in Tab. 1, are adopted here for numerical simulation.

Tab. 1 Incident wave conditions used in the simulation

Case number	T_p / cm	H_s / cm
Case1	1.4	5
Case2	1.5	5
Case3	1.6	5

Fig. 4a, b, and c depict the comparisons of the nonlinear wave surface elevations and the linear wave surface elevations at the focal points for Case1, Case2 and Case3. The relevant freak wave parameters are listed in Tab.2, where $T^* = (t - t_c) / T_p$ is the normalized time and $\eta^* = \eta / H_s$ is the normalized wave surface elevation.

The results suggest that the nonlinear freak waves exhibit a larger degree of crest-trough asymmetry due to nonlinear wave–wave interactions.

Tab. 2 Freak wave parameters of two models

	T_p= 1.4 s, linear model	T_p= 1.4 s, Nonlinear model	T_p= 1.5 s, linear model	T_p= 1.5 s, Nonlinear model	T_p= 1.6 s, linear model	T_p= 1.6 s, Nonlinear model
α_1	3.07	3.95	3.47	3.54	3.37	3.72
α_2	2.09	2.55	2.36	2.12	2.17	2.87
α_3	8.35	4.43	7.98	4.13	4.78	2.68
α_4	0.65	0.70	0.65	0.66	0.65	0.66

3.3 The impact of water depth variation and spectral peak period on freak wave

The computation region shown in Fig. 5 is used to research on the impact of water depth variation on freak wave. It is the same as the previous flat bottom example except for

the change of water depth from the minimum depth of d_2 to the maximum depth of $d_1 = d =$ 50 cm through a bottom slope, starting at x = 2 402.5 cm and truncated at 2 562.5 cm. Three different bottom slopes, s = 1:15, 1:10 and 1:8, are used in the computations, with the normalized water depth variations $\Delta d / d_1 = (d_1 - d_2) / d_1$ = 0.21, 0.32 and 0.40 respectively (d_2 = 39.3 cm, 34.0 cm and 30 cm)

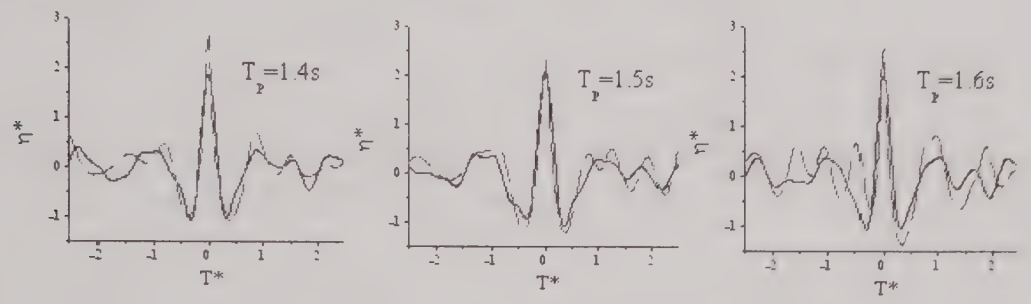

Fig. 4 Normalized surface elevation at the focal point

(- - - - nonlinear model, —— linear model)

In addition, the simulation results in the previous flat bottom example are also used for the research, and the normalized water depth variation is set to $\Delta d / d_1$ = 0.00.

The normalized water depth variation is successively set to $\Delta d / d_1$ = 0.00, 0.21, 0.32 and 0.40 for three different spectral peak periods which are listed in Tab. 1, thus defining twelve different computational cases (Case1(a) - (d) T_p = 1.4s, $\Delta d / d_1$ = 0.00 - 0.40, Case2 (a) - (d) T_p = 1.5s, $\Delta d / d_1$ = 0.00 - 0.40 and Case3 (a) - (d) T_p = 1.6s, $\Delta d / d_1$ = 0.00 - 0.40).

The position of freak wave genesis will be changed due to the uneven bottom. Therefore, 151 sampling points are set for collection.

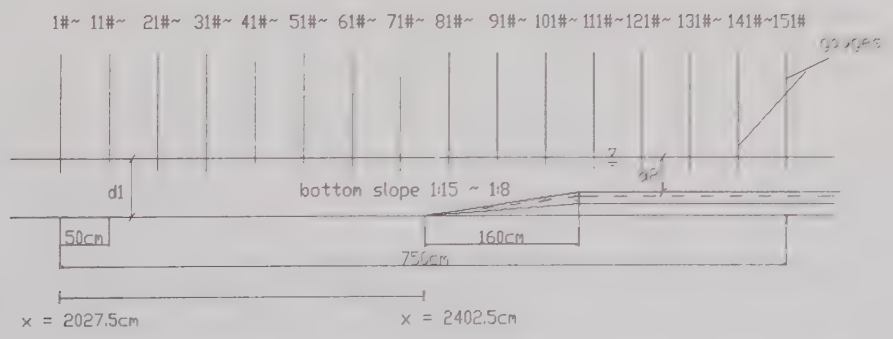

Fig. 5 Sketch of the computation domain with uneven bottom (unit / cm)

Because the wave may overturn during the process of wave propagation, the

maximum wave event may not satisfy the freak wave definition selected to represent each case. Additionally, the program would stop when waves overturn. The wave phase is reset until freak wave's occurrence.

The calculations demonstrate that the waves are breaking events in Cases 1(c) (T_p=1.4s, $\Delta d / d$ = 0.32), 1(d) (T_p=1.4s, $\Delta d / d$ = 0.40) and 2(d) (T_p=1.5s, $\Delta d / d$ = 0.40). It is absolutely true that as the period grows less or the normalized water depth variation grows larger, the wave breaks up more easily.

Fig. 6(a) to 6(e) show the nonlinear calculations in each case and the relevant freak wave parameters are listed in Tab.2. Fig.7 shows the variation of α_4 (the ratio of freak wave crest height over wave height) with $\Delta d / d$ (normalized water depth variation) corresponding to each case.

From Fig. 7, it can be seen that for the non-breaking cases, α_4 grows large (the degree of crest-trough asymmetry get higher) with increase of $\Delta d / d_1$ under the same spectral peak period condition.

Tab. 2 Freak wave parameters corresponding to all cases

	$\Delta d / d$	0.00	0.21	0.32	0.40
T_p=1.4s	α_1	3.95	3.96	3.31#	2.79#
	α_2	2.55	2.81	2.00#	2.07#
	α_3	4.43	2.50	2.49#	3.37#
	α_4	0.70	0.72	0.66#	0.66#
T_p=1.5s	α_1	3.54	4.07	3.74	4.15#
	α_2	2.12	2.00	2.03	2.59#
	α_3	4.13	3.45	3.78	2.90#
	α_4	0.66	0.68	0.77	0.66#
T_p=1.6s	α_1	3.72	3.96	3.83	3.65
	α_2	2.87	2.15	3.04	2.13
	α_3	2.68	2.86	5.47	3.39
	α_4	0.66	0.68	0.72	0.75

presents the wave phase-modified freak wave parameters

4 Time-frequency energy spectrum of freak wave and analysis

4.1 Calculation method of time-frequency energy spectrum

In order to investigate the time-frequency domain energy structure of freak wave, wavelet analysis method is used to calculate the time-frequency energy spectrum.

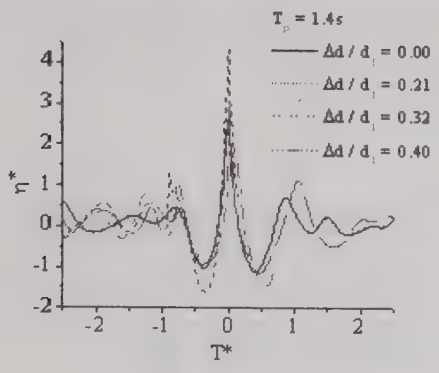

(a) uniform wave phase

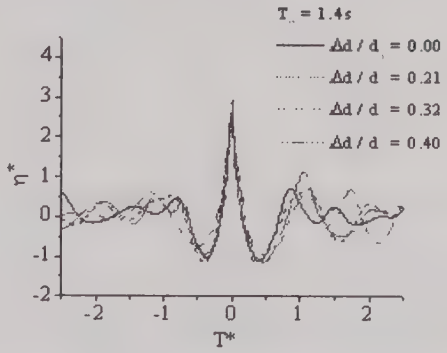

(b) $\Delta d / d_1 = 0.32, 0.40$ wave phase-modified

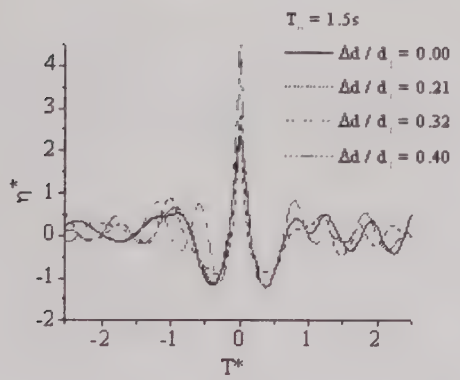

(c) uniform wave phase

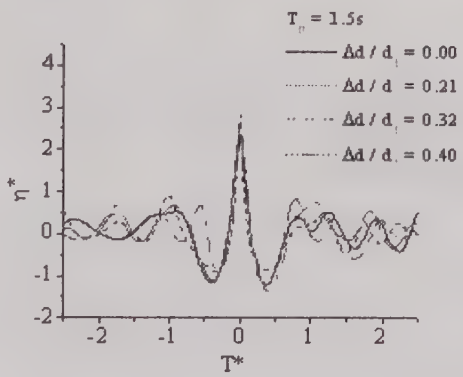

(d) $\Delta d / d_1 = 0.40$ wave phase-modified

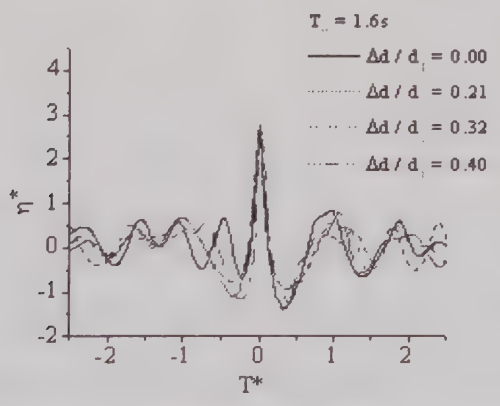

(e) uniform wave phase

Fig. 6 Dimensionless surface elevation corresponding to all cases

The Morlet wavelet is selected as the mother wavelet and the wavelet function can be expressed as:

$$\Psi(t) = \pi^{-1/4} e^{-t^2/2} e^{i\omega_0 t} \tag{11}$$

The continuous wavelet transform of a discrete sequence x_n is defined as the convolution of x_n with a scaled and translated version of $\psi_0(\eta)$:

$$W_n(s) = \sum_{n'}^{N-1} x_{n'} \Psi^* \left[\frac{(n'-n)\delta t}{s} \right] \tag{12}$$

Where the (*) indicates the complex conjugate. Although it is possible to calculate the wavelet transform using (12), it is considerably faster to approximate the continuous wavelet transform in Fourier space. By the convolution theorem, the wavelet transform is the inverse Fourier transform of the product (Torrence and Compo, 1998):

$$W_n(s) = \sum_{k=0}^{N-1} \hat{x}_k \hat{\psi}^*(s\omega_k) e^{i\omega_k n \delta t} \tag{13}$$

Where $k = 0 \ldots N-1$ is the frequency index, n is the time index, δt is time step, ω is angular frequency, s is wavelet scale, "^"represents Fourier transform, the "*" indicates the complex conjugate.

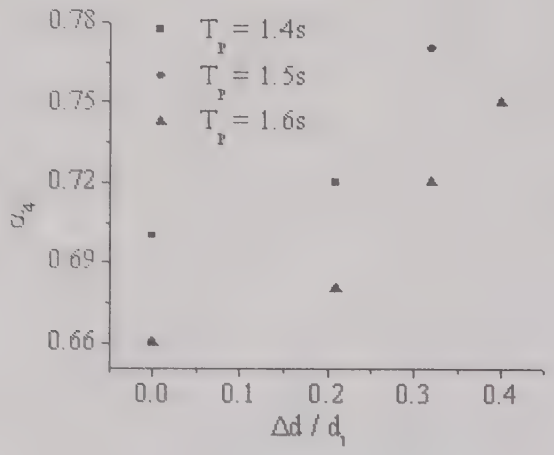

Fig. 7 Variation of α_4 with $\Delta d / d_1$

4.2 Time-frequency energy spectrum comparison of linear and nonlinear models

Fig. 8 (a) to 8(f) show the wavelet spectrum of the freak waves which are described in Fig. 4.

Fig. 8 (g) shows the wavelet spectrum of the irregular wave train including no freak wave.

Where $f^* = f / f_p$ is the normalized frequency and $T^* = (t - t_c) / T_p$ is the normalized time. The average energy per wave ($\bar{E}_{ave}{}^* = \sum_i \sum_j S_{i,j} * \Delta f_j * \Delta t_i * / N$) is used as the energy

minimum in the wavelet spectrum.

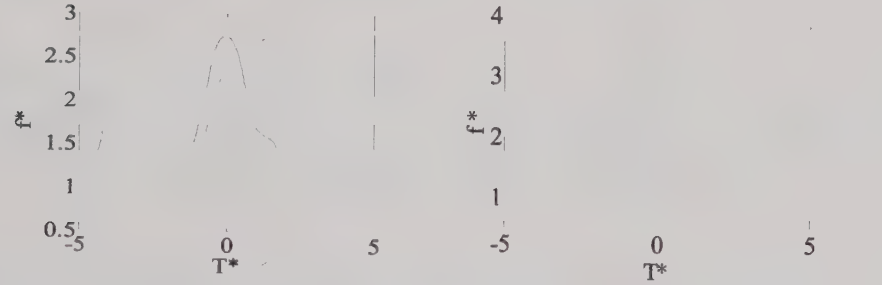

(a) Linear model, T_p=1.4s, α_4= 0.65 (b) Nonlinear model, T_p= 1.4s, α_4= 0.67

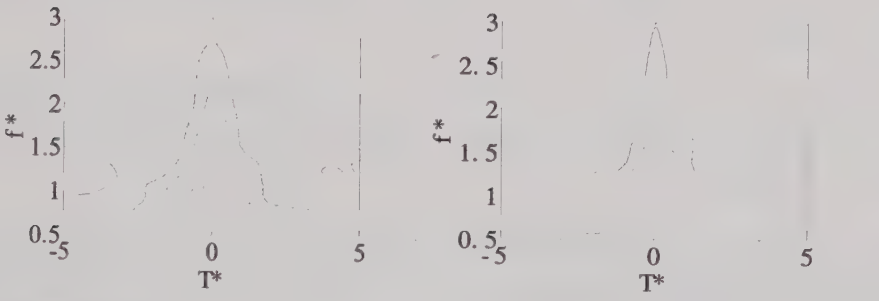

(c) Linear model, T_p= 1.5s, α_4= 0.65 (d) Nonlinear model, T_p= 1.5s, α_4= 0.66

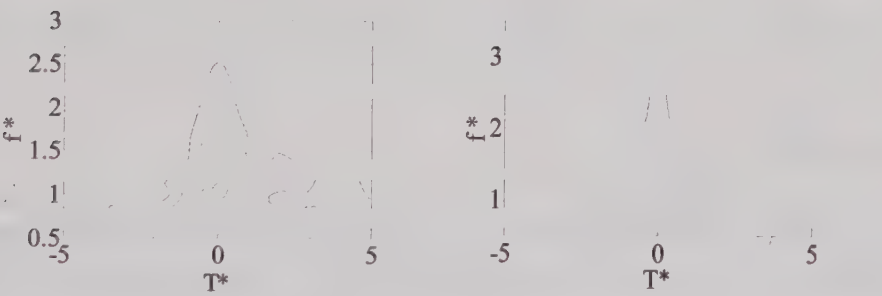

(e) Linear model, T_p= 1.6s, α_4= 0.65 (f) Nonlinear model, T_p= 1.6s, α_4= 0.66

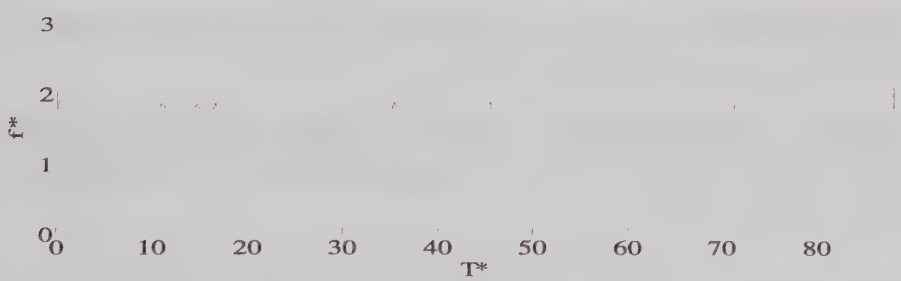

(f) Irregular wave train with no freak wave

Fig. 8 Time-frequency energy spectrum of linear and nonlinear wave records

Note that the wave train including freak wave has much more high frequency energy than the one including no freak wave and the peak in freak wave wavelet spectrum

deviates from the spectral peak frequency to high frequency direction at the onset of freak wave.

Compared with the linear freak wave wavelet spectrum (Fig. 8(a), 8(c) or 8(e)), the nonlinear freak wave wavelet spectrum (Fig. 8 (b), 8(d) or 8(f)) where more energy carries over to high harmonics at the instant the freak wave occurs, in each case (T_p=1.4s, 1.5s and 1.6s).

4.3 Impact of water depth variation on freak wave time-frequency energy spectrum

Fig.9 (a) to 9(l) demonstrate the wavelet energy spectrums of the freak waves described in Fig.6.

In each case (T_p=1.4s, 1.5s and 1.6s), the relationship between the maximum frequency component in wavelet spectrum and normalized water depth variation is considered in Fig. 10.

It can be seen from Fig. 10 that with the same spectral peak period, the increase of normalized water depth variation produces an energy transfer to high harmonics. The maximum frequency component can go far above the spectral peak frequency in 5 times.

In term of Fig.9 (h), the maximum frequency component is 7 times greater than spectral peak frequency for the breaking case (T_p = 1.5s, $\Delta d / d$ = 0.40).

5 Conclusion

In this paper, using VOF method to numerically simulate freak wave and wavelet analysis method is applied to the numerical freak wave records to investigate the energy distribution in the time-frequency domain. The following conclusion can be drawn:

The model presented in this paper can generate freak waves having larger degree of asymmetry than the dual superposition model.

The strong energy density in the wavelet spectrum appears instantly surged at the onset of the freak wave and the energy density seemingly carried over to the high frequency components at the freak wave instant.

The wave crest-trough asymmetry grows with increase of normalized water depth variation under the same spectral peak period and non-breaking condition. Change of wave phase can obtain a freak wave instead of the breaking wave. The wave phase can affect the freak wave's occurrence.

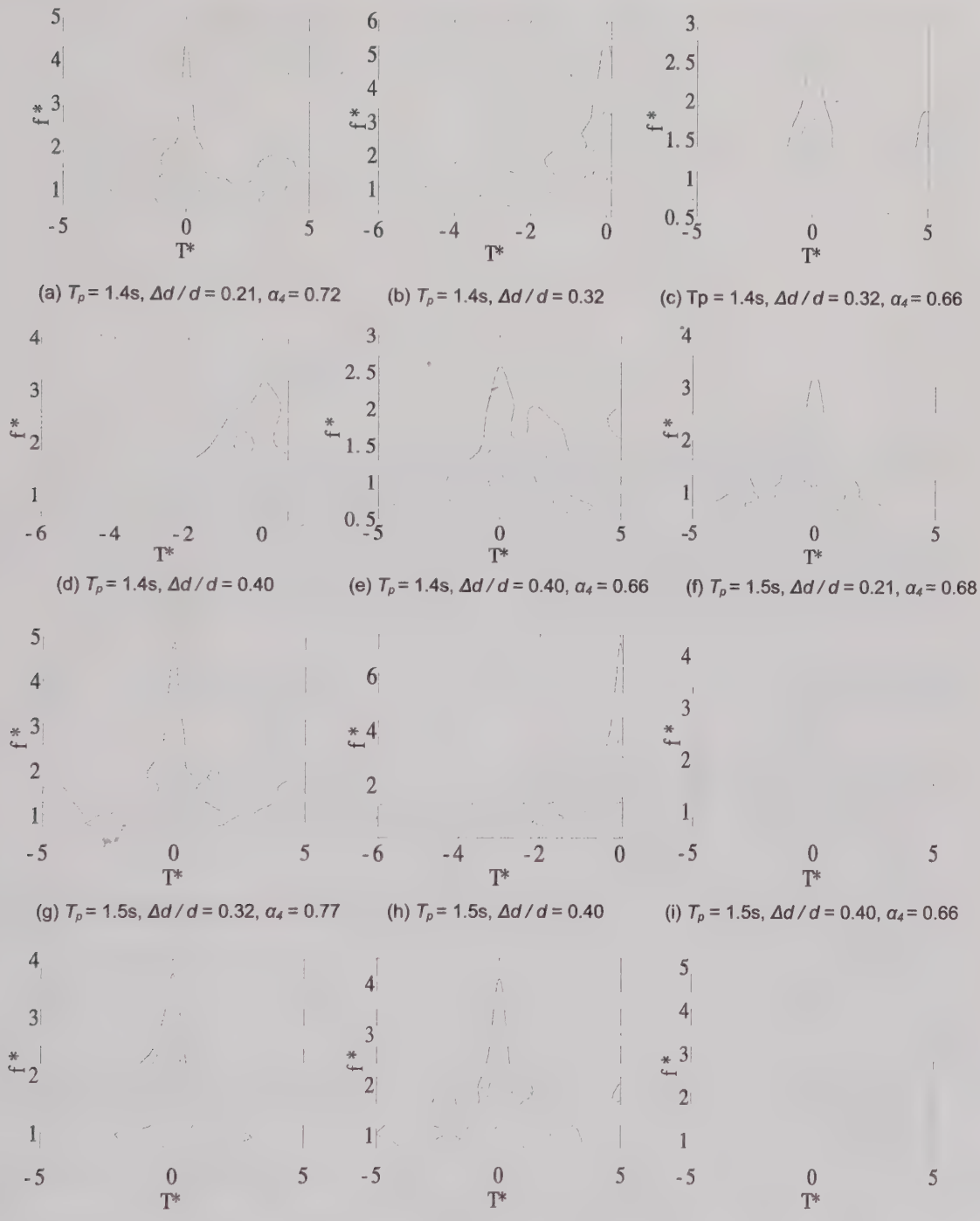

(a) T_p = 1.4s, $\Delta d / d$ = 0.21, α_4 = 0.72 (b) T_p = 1.4s, $\Delta d / d$ = 0.32 (c) Tp = 1.4s, $\Delta d / d$ = 0.32, α_4 = 0.66

(d) T_p = 1.4s, $\Delta d / d$ = 0.40 (e) T_p = 1.4s, $\Delta d / d$ = 0.40, α_4 = 0.66 (f) T_p = 1.5s, $\Delta d / d$ = 0.21, α_4 = 0.68

(g) T_p = 1.5s, $\Delta d / d$ = 0.32, α_4 = 0.77 (h) T_p = 1.5s, $\Delta d / d$ = 0.40 (i) T_p = 1.5s, $\Delta d / d$ = 0.40, α_4 = 0.66

(j) T_p = 1.6s, $\Delta d / d$ = 0.21, α_4 = 0.68 (k) T_p = 1.6s, $\Delta d / d$ = 0.32, α_4 = 0.72 (l) T_p = 1.6s, $\Delta d / d$ = 0.40, α_4 = 0.75

Fig. 9 Time-frequency energy spectrum corresponding to all cases

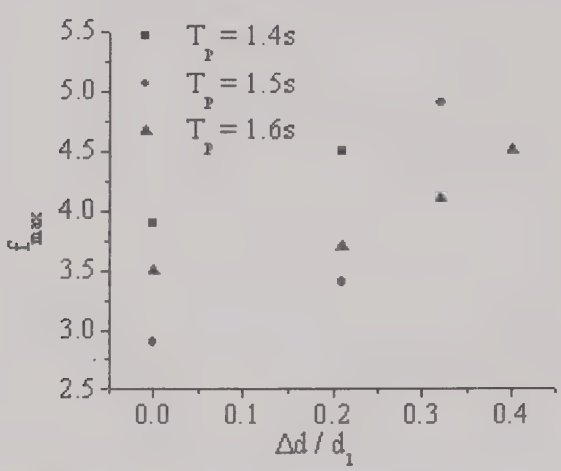

Fig. 10 Normalized water depth variation and maximum frequency component dependence

In case of identical spectral peak period, the increase in normalized water depth variation results high frequency energy accretion. The maximum frequency component can go far above the spectral peak frequency in 5 times. Under the breaking condition, the maximum frequency component can be 7 times greater than spectral peak frequency.

References

[1] Brandini C, Grilli S. Modeling of freak wave generation in a 3D-NWT, Proc.Of the 11th International Offshore and Polar Engineering Conference, Stavanger, 2001: 124 - 131.

[2] Chien H, Kao C C, Chuang L Z H. On the characteristics of observed coastal freak waves [J] Coastal Engineering Journal, 2002, 44(4): 301 - 319.

[3] Dyachenko A I, Zakharov V E. Modulation instability of Stokes wave → freak wave [J]. JETP Letters, 2005, 81(6): 255 - 259.

[4] Fochesato C, Grilli S, Dias F. Numerical modeling of extreme rogue waves generated by directional energy focusing [J]. Wave Motion, 2007, 44(5): 395 - 416.

[5] Grilli S T, Guyenne P, Dias F. A fully non-linear model for three-dimensional overturning waves over an arbitrary bottom [J]. International Journal for Numerical Methods in Fluids, 2001, 35(7): 829 - 867.

[6] Hirt C W, Nichols B D. Volume of fluid (VOF) method for the dynamics of free boundaries [J]. Journal of Computational Physics, 1981, 39(1): 201 - 225.

[7] Klinting P, Sand S E. Analysis of prototype freak waves [A]. Conf. on Coastal Hydrodynamics, ASCE, New York, 1987: 618 - 632.

[8] Kriebel D L. Efficient simulation of extreme waves in a Random Sea [A]. Abstract for Rogue waves 2000 workshops [C]. Brest, 2000: 1 - 2.

[9] Kwon S H, Lee H S, Kim C H. Wavelet transform based coherence analysis of freak wave and its impact [J] Ocean Engineering, 2005, 32(13): 1 572 - 1 589.

[10] Lin E B, Liu P C. A discrete wavelet analysis of freak waves in the ocean [J] Journal of Applied Mathematics, 2004(5): 379 - 394.

[11] Ren B, Wang Y X. Numerical simulation of random wave slamming on structures in the splash zone [J]. Ocean Engineering, 2004, 31(5 - 6): 547 - 560.

[12] Soomere T, Engelbrecht J. Interaction of shallow-water solitons as a possible model for freak waves. ICMS Workshop on Rogue Waves, Edinburgh 6, 2006.

[13] Torrence C, Compo G P. A practical guide to wavelet analysis [J] Bulletin of the American Meteorological Society, 1998, 79(1): 61 - 78.

[14] Wang Y X. Numerical wave channel with absorbing wave-maker [J]. China Ocean Engineering, 1995, 9(2): 79 - 88.

[15] Yan S, Ma Q W. Nonlinear simulation of 3D freak waves using a fast numerical method [J]. The International Society of Offshore and Polar Engineer, 2009, 19(3): 168 - 175.

[16] Zakharov V E, Dyachenko A I, Prokofievb A B. Freak waves as nonlinear stage of stokes wave modulation instability [J]. European Journal of Mechanics B/Fluids, 2006, 25(5): 677 - 692.

基于非线性模型的畸形波模拟及其时频能量谱研究

崔 成，张宁川，李靖波

（大连理工大学 海岸及近海工程国家重点实验室，辽宁 大连 116024）

摘 要：采用 VOF(volume of fluid)方法实现了畸形波的数值模拟。将数值结果与线性理论（方程（5））计算结果进行了对比，发现数值模拟结果更能够反映非线性特征。使用小波分析方法研究了畸形波的时频能量谱，发现形成畸形波的过程中存在很强的波浪非线性相互作用，使得波浪的能量向高频端转化。变水深地形可以加强波浪的非线性相互作用，使得转化到高频端的能量更多，产生畸形程度更大的畸形波。

关键词：畸形波；数值模拟；小波分析；变水深；时频能量谱

Characteristic analysis of Tianjin offshore tide

LI Xi-bin [1, 2], SUN Xiao-yan [3], WANG Shi-fu[3], YE Feng-juan [1, 2], LI Yu-jie [1, 2], LI Xiu-yan [1, 2]

1. *Tianjin Marine Environmental Monitoring Central Station, State Oceanic Association (SOA), Tianjin* 300451, *China;*

2. *Tianjin Marine Environmental Monitoring and Forecasting Center, Tianjin* 300451, *China;*

3. *National Marine Data and Information Service, Tianjin* 300171, *China;*

Abstract: Tidal data of Tanggu marine environment monitoring stations for 59 years (1950-2008) was processed by using harmonic analysis, harmonic constants curves were discussed. And by using FFT spectral analysis periodicity and causation of its harmonic constants were analyzed. After astronomic tide signal was eliminated, residual water level was decomposed by using FFT spectral analysis, and then we got the periodic variation of mean residual water level over the past 50 years and discussed mean sea level changing trends of Tianjin offshore. The results show that variety of amplitude of M_2 tidal constituent reveals 20 years, 4-6 years, 2-3-year periods, and it was obviously influenced by engineering construction since reform and opening age. Residual water level fluctuations reveal 20 years, 5-6 years, 2-3 years and 1 year periods. Sea level of Tianjin offshore displays a progressive ascending trend with rate about 3.4mm/a, which was influenced mainly by sea level rise and land subsidence.

Keywords: Tianjin, tide, harmonic analysis, spectral analysis, sea level

1 Introduction

Tide is a common phenomenon of the oceans which attractes people's attention for a long time. It affects production, living and military activities of human beings. And it is the main factor that affects maritime traffic, marine engineering construction, sea port safe operation as well as sea-route design and maintenance. Along with the ocean exploration and utilization constantly deepen, human's dependency on the oceans increases. Observation, analysis and utilization of tide are hot topics of scientific researches.

Tanggu which locates at Bohai seaside and belongs to Tianjin municipality is the door of Beijing and Tianjin on the sea. Harbor bureau built tidal observation well at Liumi dock and began to be put into use in January 1950. A temporary tidal observation station

Received on Jan. 13, 2011

Corresponding author: lixb_tj@yahoo.com.cn

located at the connection point of the 20 and 21 sections of Tianjin Xingang was used by marine environment monitoring station of Tanggu during period from July in 1986 to August in 1994. A permanent tidal observation station was put into use at jetty service boat dock (38°59'N, 117°47'E) which lies in the east of Tianjin Harbor since August 1994. Tidal data lasting for 59 years had been accumulated since January 1950. These data was systemic, consecutive and with high resolution. Although the observation well was once moved, the locations were close and all in the harbor. So these tidal data were regarded well enough to reveal Change event of Tianjin offshore tide for 59 years and was valuable for scientific research and engineering exploration.

Fig. 1 Location of Tanggu marine environmental monitoring station

In recent years, many tidal analysis methods were applied. Ou and Chen [1] studied sea level periodic variation and changing trend of Guangdong offshore by using wavelet transformation method. Yang and Wu [2] studied sea level changing trend by using low pass digital filtering method. Wang and Jiang [3] analyzed tidal data of Xiamen and Dongshan by using spectral analysis of single tidal station. Fan and Zhang [4] studied correlativity of sea level change, extremum value and sea surface wind of Tanggu marine environment monitoring station. However, less study was carried on about periodical variation and sea level changing trend of Tianjin offshore tidal data. This paper aims to make further study of tidal change and reveal sea level secular changing trend of Tianjin offshore for the last 59 years by using tidal level data analysis.

2 Tidal data analysis

Firstly, Tidal data of Tanggu marine environment monitoring station for 59 years (from 1958 to 2008) was processed by using statistical analysis method. The result shows

that tidal type value of the study area is about 0.6, which belongs to irregular semi-diurnal tide, with extreme high water level 581 cm appeared on September 1 in 1992 and extreme low water level -108 cm appeared on December 18 in 1957, annual mean high water level 374 cm and annual mean low water level 134 cm, annual mean tidal range 240 cm and annual extreme tide range 437 cm appeared in October 1980.

2.1 Harmonic Analysis

Harmonic constants along with time series were calculated by analyzing tidal data of Tanggu marine environmental monitoring center harmonically and annually for 59 years [5, 6]. The uppermost six tidal constituents were discussed in this paper. They are semidiurnal constituent M_2 and S_2, diurnal constituent K_1 and O_1, adlittoral tidal constituent M_4 and MS_4, results see Fig. 2 - 13.

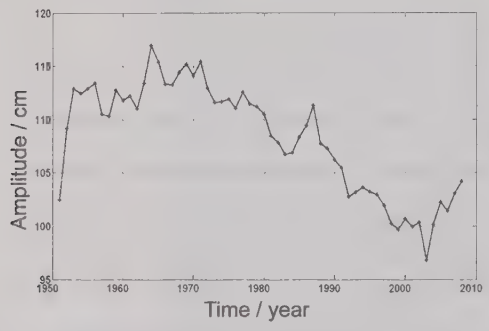

Fig. 2 Amplitude variety of M_2 tidal constituent

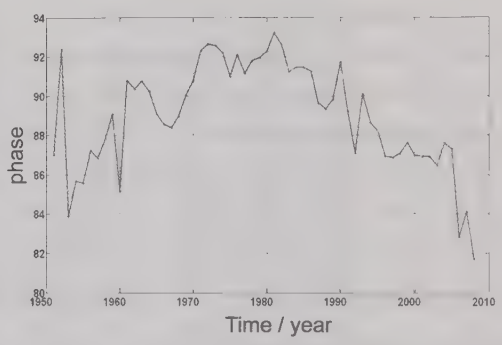

Fig. 3 Phase variety of M_2 tidal constituent

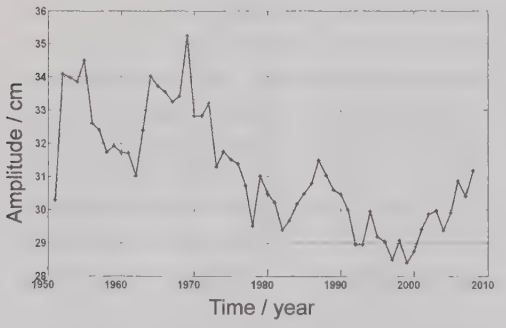

Fig. 4 Amplitude variety of S_2 tidal constituent

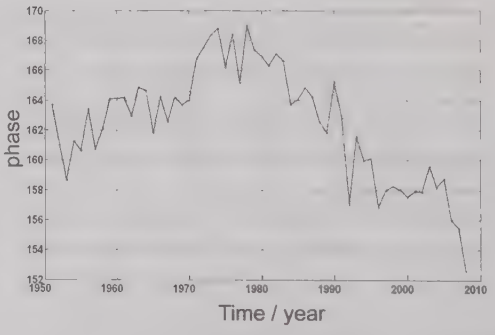

Fig. 5 Phase variety of S_2 tidal constituent

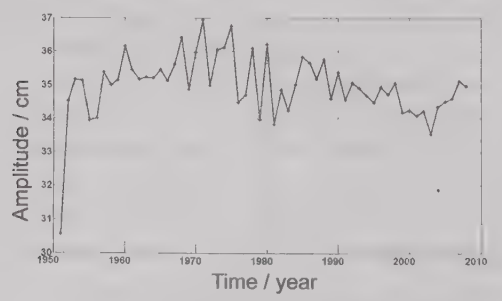

Fig. 6 Amplitude variety of K_1 tidal constituent

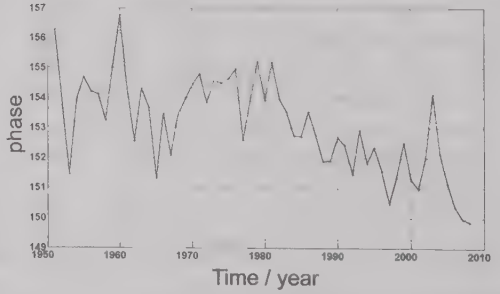

Fig. 7 Phase variety of K_1 tidal constituent

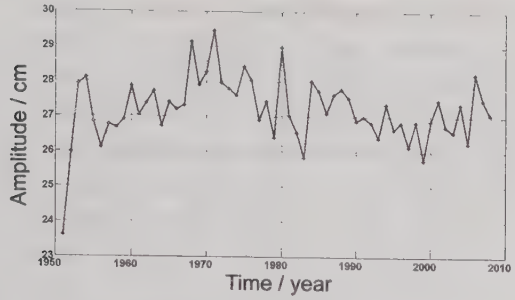

Fig. 8 Amplitude variety of O_1 tidal constituent

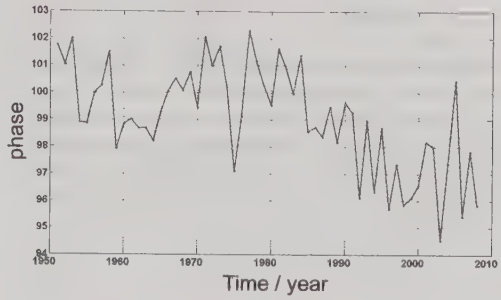

Fig. 9 Phase variety of O_1 tidal constituent

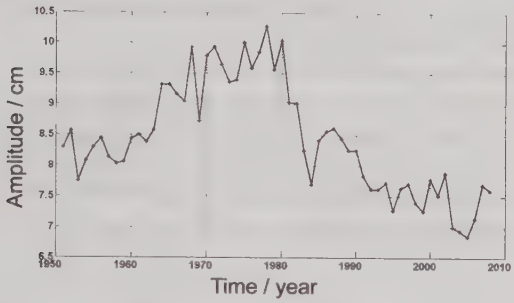

Fig. 10 Amplitude variety of M_4 tidal constituent

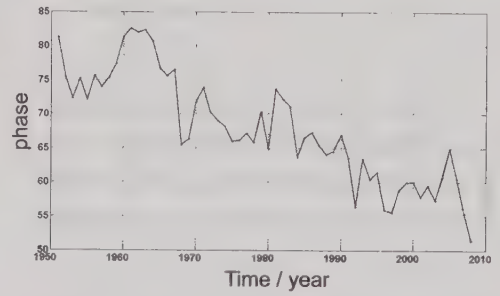

Fig. 11 Phase variety of M_4 tidal constituent

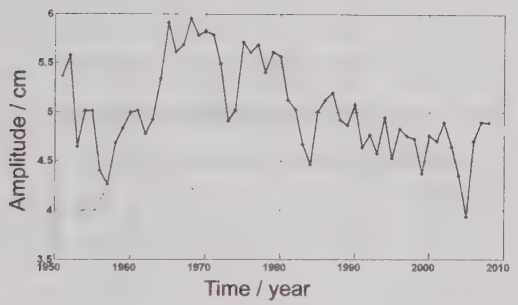

Fig. 12 Amplitude variety of MS_4 tidal constituent

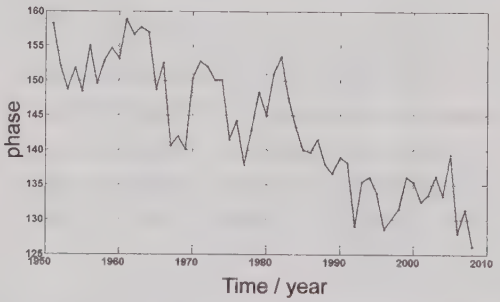

Fig. 13 Phase variety of MS_4 tidal constituent

(a) From these amplitudes and phases figures, we see that amplitudes and phases of semidiurnal constituents M_2 and S_2 displayed similar changing trend. Amplitudes of semidiurnal constituent M_2 and S_2 presented a gradually ascending trend from 1960-1970s to 2000s and gradually descending after 2000s with little vibration. Maximum amplitude of M_2 tidal constituent was 117 cm presented in 2003 and minimum value was 97 cm presented in 2003. Maximum amplitude of S_2 partial tide was 35.2 cm presented in 1969 and minimum value presented in 2003. Phases of M_2 and S_2 display gradually ascending trend since 1950s with maximum value around 1970-1980s. Of which maximum phase value of M_2 was 93.2° appeared in 1981, maximum phase value of S_2 was 168.9°appeared in 1978. Phases of M_2 and S_2 displayed gradually descending trend since 1980 with the

minimum value 81.7°and 152.6°all appeared in 2000.

(b) Amplitudes and phases of diurnal constituent K_1 and O_1 all displayed vibrant trend with about one year period. Of which amplitude of K_1 tidal constituent was about 35cm with maximum value 36.9 cm presented in 1971. Amplitude of O_1 tidal constituent was about 27cm with maximum value 29.5 cm presented in 1971. Phases of K_1 and O_1 tidal constituents kept vibrant trend before 1980, and phases value of K_1 kept around 154°and O_1 around 100°. Of which, maximum phase value of K_1 was 156.8° in 1960, maximum phase value of O_1 is 102.3° in 1977. Phases of K_1 and O_1 tidal constituents all displayed descending with vibration trend after 1980, and minimum values of K_1 and O_1 tidal constituents were 149.9° in 2008 and 94.5° in 2003 respectively.

(c) Amplitudes and phases of adlittoral tidal constituents M_4 and MS_4 displayed similar changing trend. Amplitudes of M_4 and MS_4 all displayed ascending trend with vibration during period from 1950 to 1980 and descending trend with vibration after 1980. Maximum amplitude value of M_4 tidal constituent was 10.3 cm in 1978 and minimum value was 6.8 cm in 2005. Maximum amplitude value of MS_4 was 5.95 cm in 1968 and minimum value was 3.9 cm in 2005. Phases of M_4 and MS_4 displayed descending with vibration trend since 1950. Maximum phase values of M_4 and MS_4 were 82.6° and 158.9° in 1961 and minimum phase values were 51.5° and 126.2° in 2008. Calculation of tidal energy indicated that the proportion of potential energy of M_2 tidal constituent to the whole tidal constituents was about 70 % (tidal energy was calculated by square of amplitude in harmonic constant) and its amplitude variation was nearly 20 cm which was much larger than other tidal constituent. Therefore, M_2 tidal constituent was selected to analyze annual amplitude change along with time by using spectral analysis method. The results are shown in Fig.14.

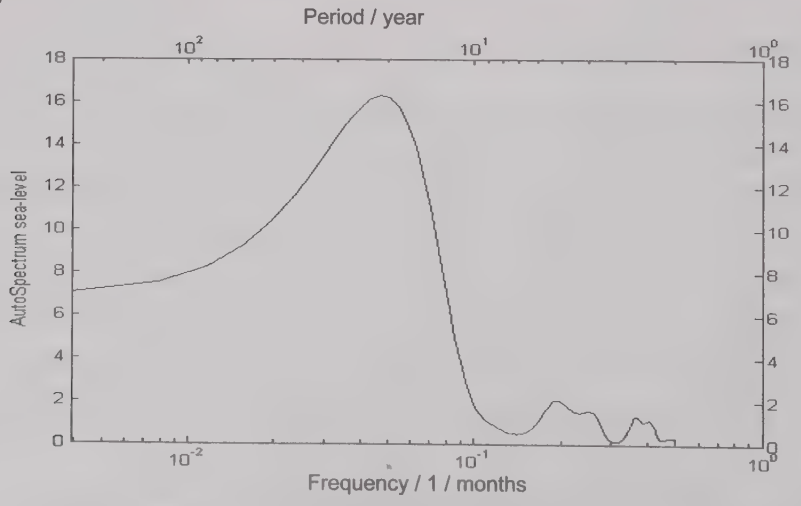

Fig. 14 Spectrum of amplitude variety of M2 tidal constituent

From Fig. 14, results of spectral analysis showed that amplitude variety of M_2 tidal constituent displayed 20 years, 4-6 years and 2-3 years periods. Maximum value of spectral analysis presented around 20 years period, which included 18.61 years period caused by ascending node westward movement and other low frequency or long time sea level changing signals. The evident 4-6 years and 2-3 years periods were similar with 2-7 years cycle of ENSO phenomena, which indicated that atmosphere forcing affected tide signal to a certain extent [1, 2]. Additionally, tidal signal was affected obviously by changes of runoff flux from Yellow River and Hai River. Wang et al[7] reported that runoff flux of Yellow River presented 2-3 years and 4-5 years periods, which resulted in variety of tidal signals of the study area. Changes of coastline and topography caused by erosion and sedimentation of Yellow River and Hai River also leaded to this variety. Additionally, in recent years, large scale of reclamation of Tianjin offshore also resulted in variety of tidal signals and consequently leaded to variety of amplitudes and phases of tidal constituents. By using least square method we calculated that amplitude of M_2 tidal constitute displayed ascending trend before 1980 with rate about 0.068 cm/a and descending trend with rate about 0.345 cm/a after 1980. Meanwhile, as a result of reclamation and port construction large scale tidal flat was filled and harbor approach was dredged which also affected adlittoral tidal constituents heavily. Amplitudes of M_4 and MS_4 all displayed ascending trend with the rates of 0.075 cm/a and 0.029 cm/a respectively before 1980, and amplitudes of the two adlittoral tidal constituents displayed descending trend with the rates of about 0.058 cm/a and 0.015 cm/a after 1980.

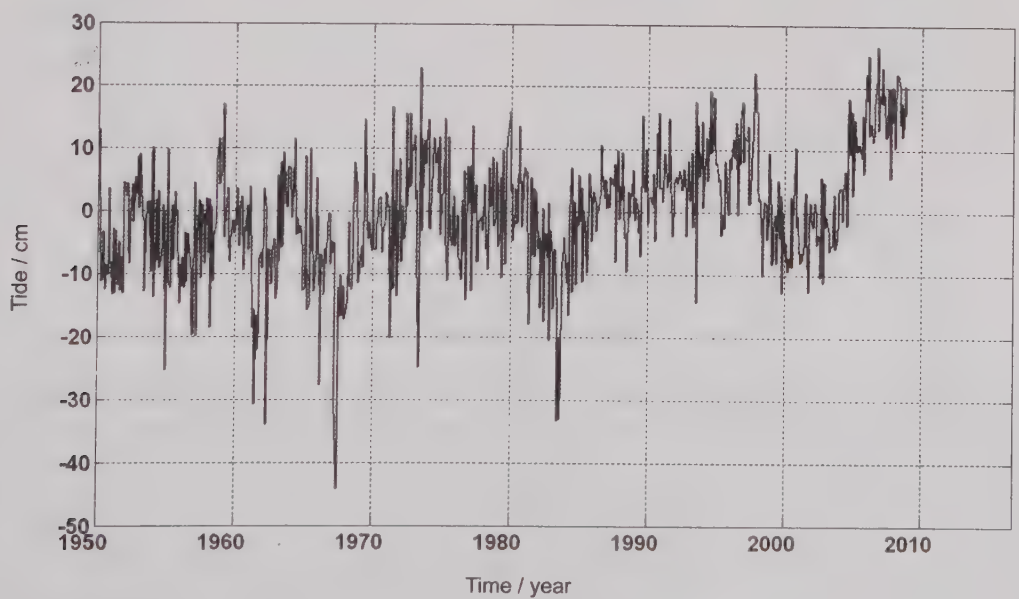

Fig. 15 Time series of monthly mean residual water level

2.2 Residual water level analysis

As we have discussed, sea level changes of Tianjin offshore were mainly caused by tidal waves transmitted from open sea. In addition, local atmosphere forcing also brought changes of sea level with amplitude about 0.5 m or even larger. Therefore, study of time series and abnormal residual water level fluctuation was necessary. From results of harmonic analysis, after sea level change caused by tidal wave was eliminated from the original data, sea level changes along time series caused by non-tidal factor were calculated, and it is so called residual water level. See results in Fig.15

From Fig.15, maximum residual water level was 26.7 cm in November 2006 and minimum value was -44.2 cm in May 1967. The residual water level along with time series documented obvious variety with large periodic waves and small amplitude vibration. In order to further study periodicity of residual water level in the study area, spectral analysis was applied. See results in Fig.16

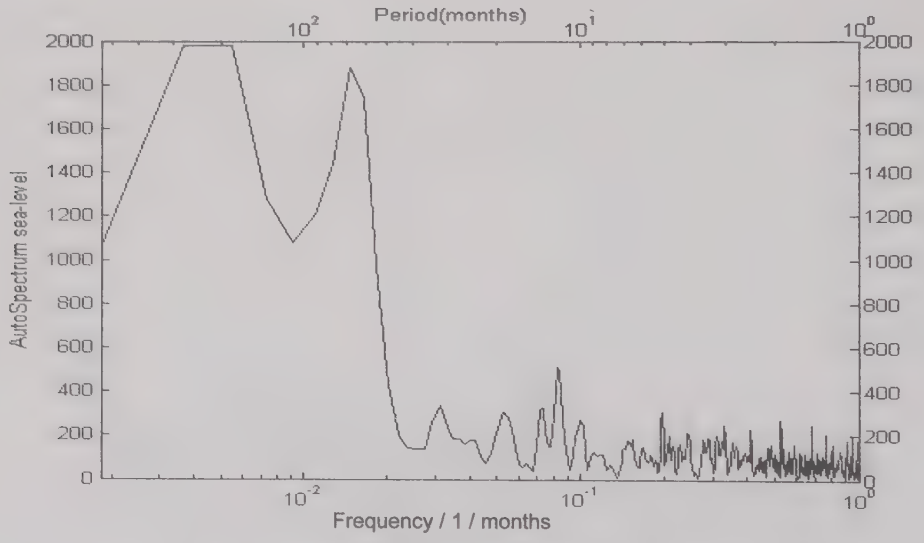

Fig. 16 Spectrum of residual water level variety

Similar to Fig.14 period of 20 years which reflected long time variety of sea level and other low frequency signals can be ignored. From Fig. 16, periods of sea level changes included 5-6 years, 2-3 years and 1 year cycle, among which signal of 5-6 years period was much more stronger. Variety of residual water level was mainly dominated by atmosphere forcing especially wind field and air pressure field. To some extent, 5-6 years period reflected variety of atmosphere forcing such as ENSO phenomena, changes of atmosphere forcing induced variety of wind field and air pressure field, consequently influenced residual water level of study area. Furthermore, periodical variation of macula

also affected residual sea level changes. And the obvious 1 year period reflected influence by monsoon transition. Southward monsoon prevailed during summer time induced low sea level in the south China offshore and high in the north and reversed in winter. Period of 2-3 years reflected influence by changing of river flux. As discussed, Yellow River had a 2-3 changing cycle. So that periodic variety of river flux influenced sea level can be got from residual sea level analysis.

2.3 Analysis of sea level change

Sea level changes influence economic development of coastal area directly, and sea level rising will threaten safety and development of this area. Study and prediction of sea level change is of significance. Commonly, annual mean sea level along with time displays some trend pattern.

Mean sea level(y) correlates with time (t) as following equation y(t)=a+bt. By using annual sea level change and least square method, rate of sea level change of Tianjin offshore was calculated. Results can be seen in Fig. 17.

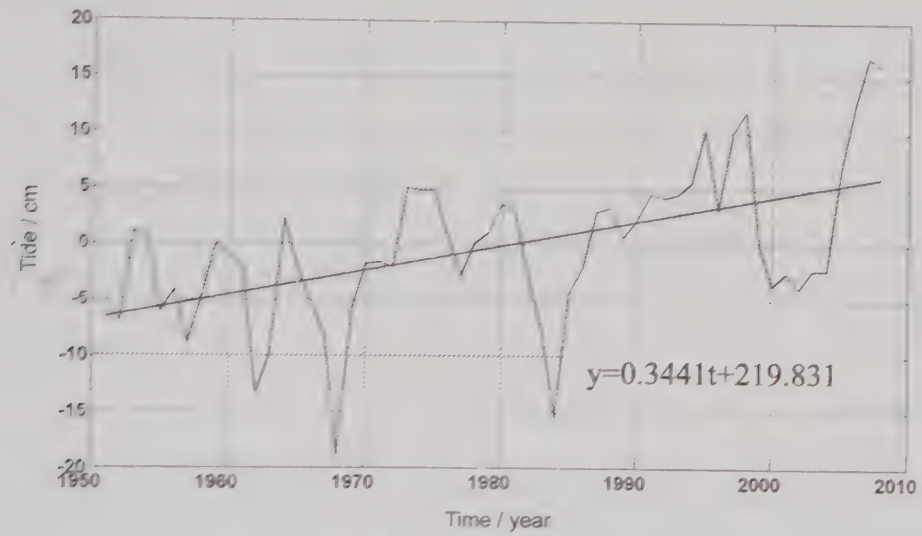

Fig. 17 Sea level changing trend of Tianjin offshore

From Fig. 17, annual sea level of Tianjin offshore raised slowly with rate about 3.4 mm/a. This ascending trend attributed to two factors, one was sea level rising and the other was subsidence of Tianjin harbor area. especially after the tidal station moved to the newly dock which located at built up area in 1986 where the subsidence was reasonable. Sea level change was comparatively stable before 1986 and intensified after 1986, which nicely explained the above situation. By averaging and fitting of tidal data from 1950 to 1986 and from 1986 to 2008 respectively. we see that mean sea level from 1950 to 1986 was

225.422 cm with ascending rate about 1.4mm/a, and mean sea level reached 236.923 cm from 1986 to 2008 with ascending rate about 4.7 cm. Compare to previous period, mean sea level was 11.501 cm higher and ascending rate was 3.3 cm/a higher which also indicated that the subsidence. However, the conclusion was got only from data of one signal observation station, plentiful sea level observation data from the surrounding area was needed to compare and to prove the subsidence of the whole Tianjin offshore area.

3 Conclusions

(1) Harmonic constants along with time series were analyzed by processing tidal data of Tanggu marine environmental monitoring station for 59 years. Calculations of tidal energy and amplitude variation indicate that M_2 is the primary tidal constituent in our study area.

(2) By using spectral analysis periodicity of residual water level of Tianjin offshore was studied. The results indicated that variety of residual sea level displayed 20 years, 5-6 years and 1 year periods. Among which, 5-6 years cycle was the leading period. Atmosphere forcing such as ENSO phenomena, monsoon transition and changing of river flux were three main factors that induced changes of residual water level in Tianjin offshore.

(3) Sea level changing rate of the study area was fitted linearly by using least square fitting method. The results indicate that sea level display ascending trend year after year with rate about 3.4 mm/a, which was influenced mainly by sea level rise and land subsidence.

References

[1] Ou S Y, Chen Z S. Application of wavelet transform to relative sea level research [J]. Scientia Geographica Sinica, 2004, 24(3):358-364.

[2] Yang Q S, Wu C Y. Application of low pass filtering to determination of secular trend in relative mean sea level change [J]. Marine Science Bulletin, 1996, 15(1):7 - 14.

[3] Wang X D, Jiang G R, Wang Y J. Spectral analysis forecast of single station tide [J]. Marine Forecasts, 2008, 25(3):53 - 59.

[4] Fan W J, Zhang A J. Study on water level variations and interrelations of its extremes and surface wind at tanggu station [J]. Marine Science Bulletin, 2006, 25(4):29 - 35.

[5] Huang Z K, Huang L. Tidal theory and calculation [M]. Qingdao: Press of Ocean University of China, 2005: 12 - 88.

[6] Wang C H. A model of the harmonic analysis of tides [J]. Marine Forecasts, 1995, 12(4):71 - 76.

[7] Wang H L, Li G S. Multi-scale analysis of runoff and sediment flux distribution of the Yellow River during the last 50 years [J]. Progress in Natural Science, 2006, 16(12):1 639 - 1 644.

[8] Zuo J C, Chen Z Y, Zhou T H. Eigenanalysis and prediction of relative sea level changes along the China coast [J]. Oceanologia et Limnologia Sinica, 1995, 26(3): 331 - 337

天津近海潮汐特征分析

李希彬[1,2]，孙晓燕[3]，王世福[3]，叶风娟[1,2]，李玉杰[1,2]，李秀艳[1,2]

（1. 国家海洋局天津海洋环境监测中心站，天津 300451；2. 天津市海洋环境监测预报中心，天津 300451；
3. 国家海洋信息中心，天津，300171）

摘 要：对塘沽海洋环境监测站从1950年 — 2008年，59年的潮汐资料进行调和分析，分析了其分潮调和常数的变化曲线，并利用FFT谱分析方法对其调和常数的变化周期和原因进行了分析；之后应用FFT谱分析方法对去除天文潮后的余水位进行分解，分析了近 50 多年来年平均余水位的多层次周期分布，进而利用最小二乘法进行线性分析，分析了天津近海平均海平面的变化趋势。结果表明，天津沿岸潮汐M2分潮振幅变化存在 20 年、4 — 6年、2 — 3年的周期，且明显受到改革开放后工程建设的影响；余水位变化包含着 20 年、5 — 6年、2 — 3年、1年等不同周期的时间尺度变化，天津近海海平面呈逐渐上升趋势，上升幅度约为3.4 mm/a，主要受海平面上升和地面沉降两部分因素影响。

关键词：天津；潮汐；调和分析；谱分析；海平面

Distribution of dissolved cadmium in Prydz Bay, Antarctica

SUN Wei-ping[1, 2], HU Chuan-yu[2], HAN Zheng-bing[2], XUE Bin[2], PAN Jian-ming[2]

1. *Institute of Environment and Biogeochemistry, Zhejiang University, Hangzhou* 310027, *Zhejiang Province, China ;*

2. *The Second Institute of Oceanography, State Oceanic Administration, Hangzhou* 310012, *Zhejiang Province, China;*

Abstract: In order to better understand the spatial and temporal distribution of dissolved cadmium in Prydz Bay, east Antarctica , seawaters were sampled by CTD during the CHINARE-25 cruise (Oct. 2008 – Apr. 2009) and the concentrations of cadmium were analyzed by AAS (Atomic Absorption Spectrometry) in the clean laboratory. Together with the data of macronutrients and chl.a from the same cruise, the relationship between cadmium and biological process was studied. The results showed that the concentrations of Cd in the surface water had a good relationship with chl.a and biologicl process was the important factor that influenced the distribution of dissolved Cd in the surface water. Linear relationship was found between dissolved Cd and phosphate in the surface water and the high ratio of Cd/P at the edge of ice shelf was most probably due to ice melting. vertical distribution of Cd was similar to those of macronutrient such as phosphate and was affected by decomposition of organic particals. The temporal change of dissolved Cd in upper layer was slight and tide probably had influence on the change.

Keywords: dissolved cadmium, micronutrient, Prydz Bay, Antarctica

1 Introduction

Over the past decades, cadmium was considered to be a priority pollutant, a nonessential or even toxic metal to organisms. But increasing evidences indicate that cadmium could actively be taken up by marine phytoplankton and substitute into the metalloenzyme carbonic anhydrase (CA), which catalyses the uptake of bicarbonate (HCO_3^-) from seawater and provides a source of inorganic carbon for photosynthesis （Morel, 2003）. In zinc limited seawater, cadmium could substitute for zinc in CA and lead

Received on Apr. 20, 2010

Corresponding author: sunwp1998@hotmail.com

to an increasing in cellular CA activity and growth rate (Price, 1990; Morel, 1994; Lane, 2000; Lee, 1995). As the substitute of essential element, cadmium could also be taken up by halobios (Boyle, 988; Bruland, 1980; Frew, 1992) because of its similar geochemical character with calcium (Weng, 1996). The ratios of Cd/P or Cd/Ca were also regarded as the important indicators for biogeochemical cycling of macronutrients and paleooceanography.

Prydz Bay is one of the biggest bays around the Antarctic Continent besides Weddell Sea and Ross Sea, but researches about micronutrients in this area had little been done. Investigation about distributions of micronutrients in the surface water of Prydz Bay has been carried out utilizing water samples from CHINARE-24 Survey (Sun, 2009). In this paper we discussed the spatial and temporal distribution of dissolved cadmium in the water column of Prydz Bay utilizing the data from CHINARE-25 Survey.

2 Materials and methods

During the CHINARE-25 Survey (from October 2008 to April 2009), twenty five sampling stations were settled in Prydz Bay (Fig.1) and the spatial and temporal distributions of dissolved cadmium were monitored. For the temporal continuing observation, we selected the one near Zhongshan station and sampled almost every three hours from 8 to 21 clock in 9 December and from 0 to 12 clock in 10 December 2009. For the spatial monitoring, IS stations near Amery Ice Shelf, P2, P3 and P4 sections between Fram Bank and Four Ladies Bank, including seasonal polynyas and outside continent shelf were conducted from 23 January to 18 February 2009 (Fig. 1). The water depth was more than 1500 meters for the stations outside continent shelf and not more than 900 meters for the residuals.

Water samples were obtained from Niskin bottles deployed on the CTD-Rosette and filtered through a 0.45μm diameter polycarbonate filter. After acidification with suprapure nitric acid to pH<2.0, waters were stored in polyethylene bottles with clean plastic bags encapsulation and analyzed in domestic laboratory. Dissolved cadmium was analyzed by graphite atomic absorption spectrometry (Perkin Eimer 800, American) according to national criterion of oceanic monitoring GB17378.4-2007. All the glassware and sampling bottles were dipped in the nitric acid (1:3) for more than 24 hours and washed with MILLI-Q purified water repeatedly; the standard solution was offered by the Centre of Standard Substance from the Second Institute of Oceanography, State Oceanic Administration. All the analytical work was conducted in the clean laboratory and utilized analytical purity or suprapure reagents. The precision estimated by replicate analysis (n = 10) at 0.2 nM was

±3.2%. Other parameters such as macronutrients and chlorophyll a were also analyzed according to GB 17378.4-2007.

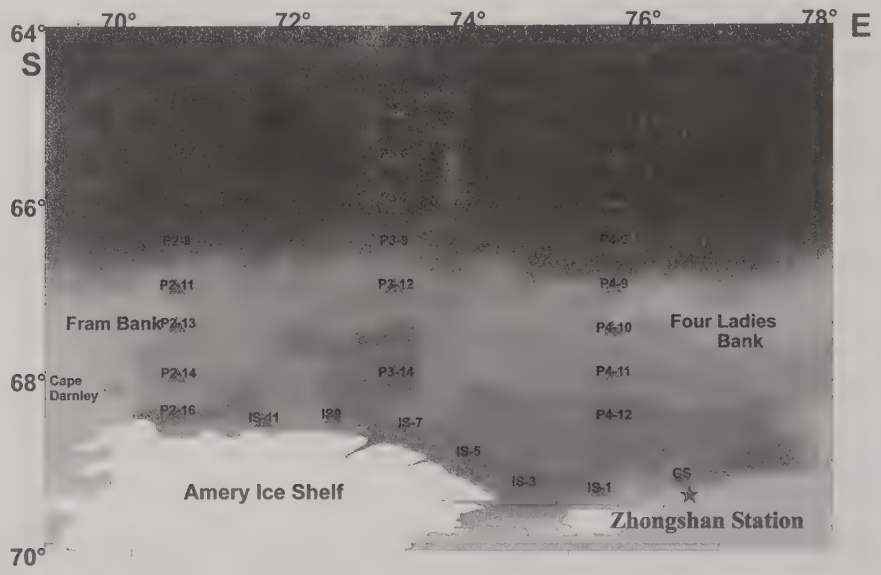

Fig. 1 Sampling stations in Prydz Bay

3 Results and discussion

3.1 Dissolved cadmium in the surface water

3.1.1 Distribution of dissolved cadmium

The concentration of dissolved cadmium in Prydz Bay ranged from 0.08nM to 0.55nM, the average concentration was 0.22nM, similar to those in the Southern Ocean with the concentration range from 0.12nM to 0.28 nM. (Frew, 2001), but somewhat lower than those in Weddell Sea with the range from 0.5nM to 0.8 nM (Westerlund, 2001). According to hydrogeological conditions, three different study areas were partitioned, i.e. edge of Amery Ice Shelf (IS stations), polynyas (P2-11,P2-13, P2-14, P3-14, P4-9, P4-10, P4-11, P4-12) and outside the continental shelf (P2-8, P3-5,P3-6, P3-7, P3-9, P4-4, P4-5, P4-6). The station P2-16 was near the Amery Ice Shelf and obviously had higher concentration of cadmium than other P2 stations (Fig. 1), it was probably influenced by continental influx from Amery Ice Shelf, so that would be discussed together with IS stations in the following text.

During Antarctic summer, ice melting at the margin of Amery Ice Shelf schlepped a lot

of weathering productions in the ocean. A part of particles from the continent, including trace metals, dissolved in the water during sedimentation, the majority of particles settled in the bottom and became part of the sediments. Through resuspend and redissolve input more dissolved trace metals in water column. So the content of dissolved cadmium at the margin of ice shelf should be higher than that in open sea area and the concentration would gradually decrease from near shore to open sea in theory. But in fact, the average concentrations of the three areas were 0.20nM, 0.17nM and 0.29nM, respectively. Instead of margin of ice shelf, outside the continental shelf had the highest concentration of dissolved cadmium and polynays had the lowest as shown in the Fig. 2, which might due to biological uptake by phytoplankton. Chlorophyll a (chl.a) presents biomass of phytoplankton in the ocean and its average concentrations in three study areas were 3.92 μg/L, 1.35 μg/L, 0.29 μg/L, respectively. The biomass was highest at the margine of ice shelf, which contribute to the highest uptake of cadmium by phytoplankton and lead to rapid decrease of cadmium. So the content of dissolved cadmium at the margin of ice shelf was lower than that outside continental shelf despite the highest input from ice melting. Certainly, the relative lower input and higher uptake led to the lowest concentration in polynays. Negative correlation between dissolved cadmium and salinity was found in open sea, but there was only ambiguous relationship in this study by selecting two transects outside continent shelf, i.e. P3 and P4 sections, so we suggested that biological process was the most important factor affecting the distribution of dissolved cadmium in the surface water of Prydz Bay.

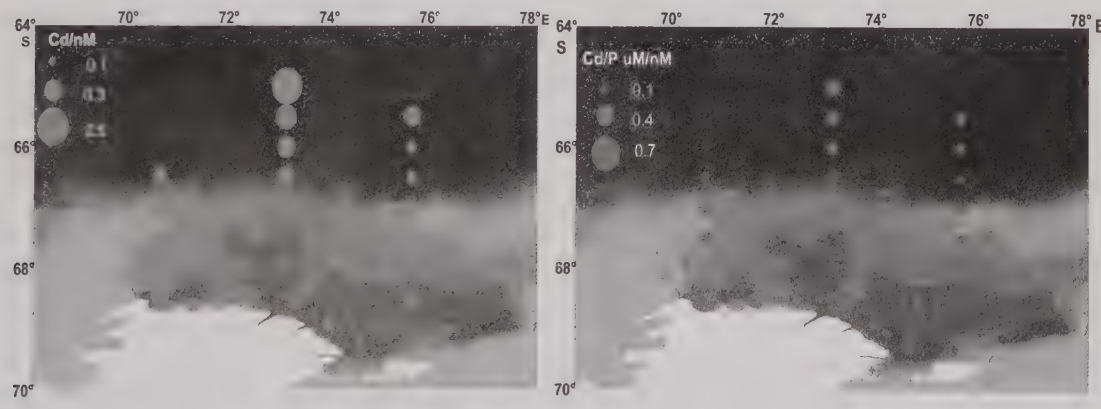

Fig. 2 Distribution of dissolved Cd and Cd/P Ratio in the surface water of Prydz Bay

3.1.2 Relationship between cadmium and phosphate

Boyle (1988)found out, when the concentration of phosphate below 1.3 μM, the Cd-P relationship had a slope of about 0.21 nmol /μmol(Cd/P), passing only slightly below the origin at zero P. Above 1.3 μM, the Cd-P relationship had a slope of about 0.40 nmol /μmol

(Cd/P) and a zero P intercept at Cd=—0.25 nM. Selecting two study areas, one including stations near Amery Ice Shelf and another outside the continental shelf, the average concentrations of the two areas were 1.0 μM and 1.5 μM, respectively, and the calculated slopes were 0.27 nmol /μmol and 0.43 nmol /μmol, respectively. It was similar to that Boyle had reported（Fig. 3）, suggesting that marine biological process may the important factor that influences the distribution of dissolved cadmium in the surface water of Prydz Bay.

Comparing the ratios of Cd/P in three areas, margin of ice shelf（0.35 nmol /μmol）>outside continental shelf（0.19 nmol /μmol）> polynyas（0.17 nmol /μmol）. There are mainly three possibilities answering for the high ratio of Cd/P in water column: (1) mixing of external waters with high Cd/P ratio; (2) different population structures; and (3) continental input and regeneration from sediments. Prydz Bay is rather a closed bay because of Fram Bank and Four Ladies Bank, which prevent external waters entering Prydz Bay, and the Cd/P ratios in water colum of Southern Ocean are commonly lower (Frew, 1992), so the influence of external waters could be neglected. Diatom is the most popular phytoplankton in Prydz Bay and there's not too much difference in biological population (Sun, 2003). But the diatom biomass could also influence Cd/P ratio. The uptake of cadmium and phosphate by phytoplankton is always in the definitive molar ratio, which was 0.001 nmol /μmol suggested by Morel (1985) and was far away lower than the Cd/P ratio in the seawater, so higher biomass only led to lower Cd/P ratio in seawater. So the high ratio of Cd/P at the margin og ice shelf was not possibly due to high biomass,it was most probably caused by the input from ice melting or/and regeneration from sediments. Additional input of cadmium from ice and sediments increased original Cd/P ratio in seawater and it remained high despite high uptake by phytoplankton. The regeneration of sediments could affect the Cd/P ratio at the water-sediment interface and definitive depth above the interface, and it would have slight influence on the surface water. So the high Cd/P ratio at the margin of ice shelf was most probably due to ice melting.

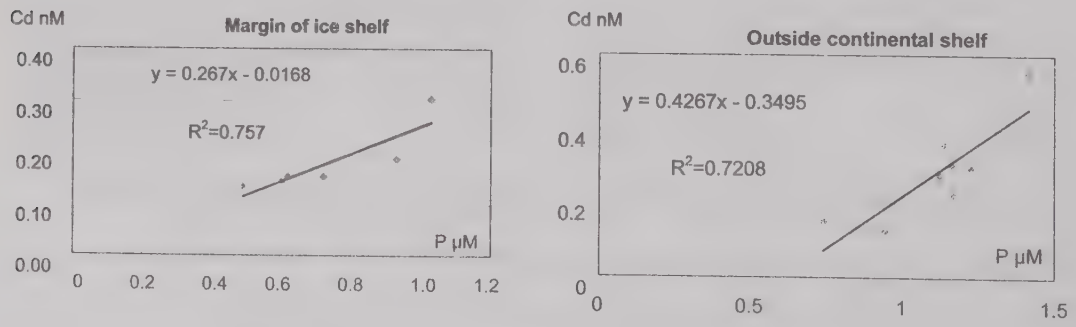

Fig. 3 Cd-P diagram in the surface water of Prydz Bay

3.2 Vertical distribution of dissolved cadmium above 200 m

P3-14 station in polynyas, P3-5 and P3-7 stations outside the continental shelf were selected to study the vertical distribution of dissolved cadmium in water column above 200 meters. The analytical results showed (Fig. 4a) that the concentration of dissolved cadmium was lower in near-surface water and achieved the minimal concentration in the depth of (25 - 50) meters, subsequently rose again with the depth and reached the highest concentration in 100 meters deep. From 100 m to 200 m, the concentration changed slightly.

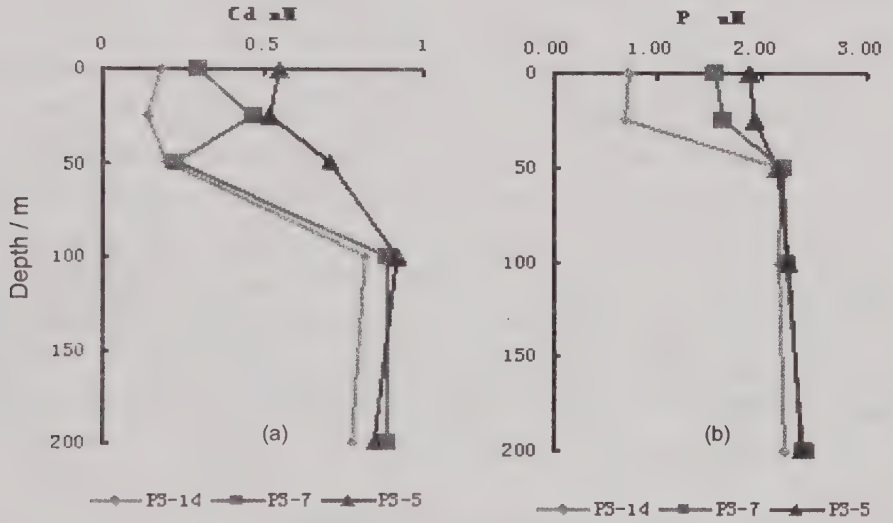

Fig. 4 Vertical profiles of dissolved Cd

(a) and phosphate (b) in the water column above 200 m

The characteristic vertical distribution of dissolved cadmium was probably due to the biological activity in euphotic zone. Photosynthesis is the most intense in euphotic zone near 25 meters and so do the biological activity. According to the report (Qin, 2004), most cells of phytoplankton lived in near-surface water in Prydz Bay, especially in the inner bay, i.e. south of 67°S. With the uptake of dissolved cadmium as micronutrient by phytoplankton, its content dropped down most rapidly and got the lowest concentration in this layer. The uptake was then decreasing with the depth and declined photosynthesis; the content of cadmium in water column rose again and got the highest concentration at 100 m depth without significant change below this layer. Phosphate, silicate and nitrate are the most important macronutrients for the organisms and closely linked to the biological process. The abundance of phytoplankton cells in Prydz Bay was also closely related to the concentration of nutrients such as nitrate (Sun, 2003). Selecting three sections (P3-5, P3-7

and P3-14) and calculation the linear correlation coefficient r between cadmium and phosphate. The result showed that r=0.71(n=15) with the probability level p=0.003, which meant that the relationship between dissolved cadmium and phosphate in the vertical water column was significant. The good relationship between dissolved cadmium and phosphate suggested once again that dissolved cadmium was affinitive to biological process. Fig.4b showed the vertical distribution of phosphate, which was almost similar to that of cadmium except the points of the appearance of the highest concentrations. Different from the cadmium, whose highest concentration appeared at 100 m depth, the highest concentration of phosphate was at 50 m depth. We suggested that this difference was probably due to different decomposition time of cadmium and phosphate in debris and feces of plankton. The uptake of cadmium and phosphate from the water column by phytoplankton occurred at the same time, but the decomposition of cadmium was slowler than that of phosphate. Once the debris and feces of plankton were decomposed, phosphate released to the water column firstly and then did cadmium slowly. So the highest concentration of phosphate in water column appeared in upper layer than that of cadmium. Tsunogai(1991) summarized that particulate fluxes in polar were one or two orders of magnitude larger than that in the greater part of the pelagic ocean, among these mostly were organic particals. Those organic particals carrying cadmium and phosphor decomposed during sedimentation from surface to deep water and played a much more important role in the vertical distribution of dissolved cadmium and Cd/P ratio in water column in Prydz Bay compared to other ocean areas.

3.3 Temporal change of dissolved cadmium above 25 m

The continuous monitoring of dissolved cadmium in the surface, 10 meters and 25 meters depth in Prydz Bay near Zhongshan station was conducted during 24 hours in Antarctic summer. The result showed that the content of cadmium in water column was relatively steady and changed slightly during monitoring. It ranged from 0.7nM to 1.1nM and appeared relative lower concentration during 6:00 - 9:00 a.m, even no cadmium could be detected at 25 m depth. Wang (2008) suggested, when the concentration of bivalent cadmium was not higher than 1.0 nM, the uptake of cadmium by phytoplankton was proportion to the content of dissolved cadmium and light intensity. The light intensity changed slightly during study time and only had little effect on the uptake, and the relative lower concentration was probably due to the mixing of water mass with different cadmium content caused by tide.

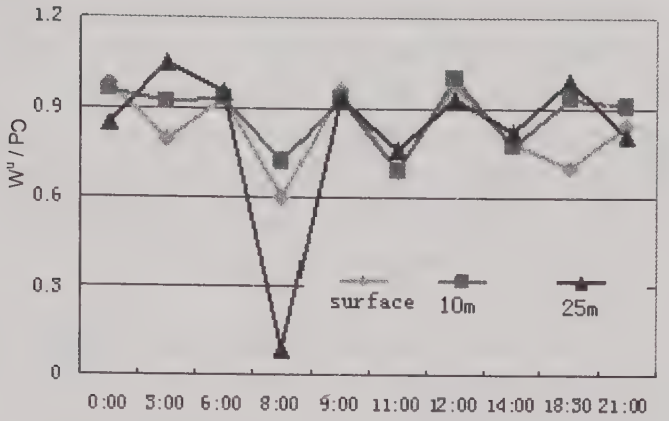

Fig.5 Temporal change of dissolved Cd in the water column above 25 m

4 Conclusions

The spatial and temporal distribution of dissolved cadmium was studied during CHINARE-25 survey. The results showed that the distribution of dissolved cadmium in the surface water of Prydz Bay had a good relationship with chl.a, and biological process was the important factor that influenced the distribution of dissolved cadmium in the surface water. The vertical distribution of dissolved cadmium was similar with phosphate in the water column above 200 meters and was affected by decomposition of organic particals. The concentration of dissolved cadmium in Prydz Bay changed slightly during day and night and the temporal change was most probably due to tide. Next we will focus on the micronutrients in the sediments, inter-surface and marine food chain in Prydz Bay, in order to understand the transformation mechanism of micronutrients and the relationship between micronutrients and biological activities in marine environment.

Acknowledgement

This research is supported by the National Natural Science Foundation of China No. 41076134.

References

[1] Boyle E A. Cadmium: Chemical tracer of deep water paleoceanography [J]. Paleoceanography, 1988, 3: 471 - 489.

[2] Bruland K W. Oceanographic distributions of cadmium, zinc, nickel, and copper in the North Pacific.

[J] Earth and Planetary Science Letters, 1980, 47: 176 - 198.

[3] Frew R D, Hunter K A. Influence of Southern Ocean waters on the cadmium phosphate properties of the Global Ocean [J]. Nature, 1992, 360: 144 - 146.

[4] Frew R D, Bowie A, Croot P, et al. Macronutrient and trace-metal geochemistry of an in situ iron-induced Southern Ocean bloom [J]. Deep-Sea Research II, 2001, 48: 2 467 - 2 481.

[5] Lane T W, Morel F M M. A biological function for cadmium in marine diatoms [C]. Proceedings of the National Academy of Sciences of the United States of America, 2000, 97: 4 627 - 4 631.

[6] Lee J G, Morel F M M. Replacement of zinc by cadmium in marine phytoplankton [J]. Marine Ecology, Progress Series 1995, 127: 305 - 309.

[7] Morel F M M, Hudson R J M. The geobiological cycle of trace elements in the aquatic system: Redfield revisited. In: W. Stumm (Editor), Chemical Processes in Lakes. Wiley-Interscience, New York, NY, 1985: 251 - 281.

[8] Morel F M M. Zinc and carbon co-limination of marine phytoplankton [J]. Nature, 1994, 369: 740 - 742.

[9] Morel F M M, Price N M. The biogeochemical cycles of trace metals in the oceans [J]. Science, 2003, 300: 944-947.

[10] Price N M, Morel F M M. Cadmium and cobalt substitution for zinc in a marine diatom [J]. Nature, 1990, 344: 658 - 660.

[11] Weng H X, Presley B J. Bioaccumulation of heavy metals in oyster (Crassostrea virginica) [J]. Acta Scientiae Circumstantiae, 1996, 16(1): 51 - 58.

[12] Qin Y, Huang Y, Liu G, et al. Spatial and temporal variations of primary productivity in Prydz Bay and its adjacent sea area, Antarctica [J]. Journal of Xiamen University (Natural Science), 2004, 43(5): 676 - 681.

[13] Sun J, Liu D Y, Ning X R, et al. Phytoplankton in the Prydz Bay and the adjacent Indian sector of the Southern Ocean during the austral summer 2001/2002 [J]. Oceanologia et limnologia sinica, 2003, 34(5).

[14] Sun W P, Hu C Y, Xue B, et al. Distribution of copper, cadmium and zinc in the surface water of Prydz Bay [J]. Chinese Journal of Polar Research, 2009, 21(1): 25 - 32.

[15] Tsunoga S, Noriki S. Particulate fluxes of carbonate and organic carbon in the ocean. Is the marine biological activity working as a sink of the atmospheric carbon [J]? Tellus, 1991, 43B: 256-266.

[16] Wang M J, Wang W X. Cadmium toxicity in a marine diatom as predicted by the cellular metal sensitive fraction [J]. Environ.Sci.Technol, 2008, 42: 940 - 946.

[17] Westerlund S, Oehman P. Cadmium, copper, cobalt, nickel, lead, and zinc in the water column of the Weddell Sea, Antarctica [J]. Geochimica et Cosmochimica Acta, 2001, 55(8): 2 127 - 2 146.

南极普里兹湾溶解态镉的分布

孙维萍[1,2]，扈传昱[2]，韩正兵[2]，薛 斌[2]，潘建明[2]

（1. 浙江大学 环境与生物地球化学研究所，浙江 杭州 310027；
2. 国家海洋局第二海洋研究所，浙江 杭州 310012）

摘 要：利用 25 次南极科考获得的海水样，采用原子分光光度法（AAS）测定了海水中溶解态镉的含量，研究了东南极普里兹湾不同空间与时间尺度下海水中溶解态镉的分布特征。并利用同航次相关的营养盐、叶绿素 a 等数据，分析了影响海水中溶解态镉分布的主要因素。研究结果显示，普里兹湾表层海水中溶解态镉的分布与叶绿素 a 具有良好的相关性，生物过程是影响普里兹湾表层海水中溶解态镉平面分布的主要影响因素。表层海水中镉与磷具有良好的线性关系，冰架边缘的海冰融化可能是造成冰架边缘 Cd/P 比值高的主要原因。溶解态镉在垂直分布上表现出近似磷酸盐等营养盐的分布趋势。普里兹湾海水中溶解态镉的浓度在时间序列上的变化不大，潮汐可能是影响海水中镉浓度微弱变化的主要因素。

关键词：溶解态镉；微量营养元素；普里兹湾

Preliminary screening of antimicrobial and antitumor activities from cultivated microalgaes

DENG Wei, WANG Xue-qing*, SONG Wen-jun

The Tianjin Key Laboratory of Food and Biotechnology; Tianjin University of commerce, College of Biotechnology and Food Science, Tianjin, 300134, *China*

Abstract: Hydrophilic and lipophilic extracts were prepared from 8 microalgal strains, and screened for antimicrobial and antitumor activities. Antimicrobial activity was determined by observing bacterial (*S. aureus*, *Bacillus subtilis* and *Escherichia coli*) and fungal(*Aspergillus niger* and *Penicillium chrysogenum*) growth inhibition. All the microalgae had different degrees of antimicrobial activity against one or more microbe – tested, and 56.47% of the extracts showing the *anti-S.aureus* activity exhibited the antibacterial activity against (MRSA). Cytotoxic activities were measured in vitro against human cancer cell lines HeLa by the MTT assay. Most of these extracts showed potent activity against the growth of the tumor cells, especially the intracellular lipophilic extracts from *Isochrysis galbana* Parke 3011 and *Isochrysis galbana* Parke H29, which exhibited strong antitumor activity against HeLa cell lines. The overall results of this study indicate that the extracts from microalgae represent a potential sources of medicine for the treatment of infectious and cancer diseases.

Keywords: microalgae, screening, antimicrobial, antitumor

1 Introduction

Microalgae, micro-phytoplankton with large quantity of species and rapid propagating, are the primary of food chain, playing an extremely important role in material and energy circulation in waters. An increasing evidence showed that actual producers of some novel active substances of marine organisms were microalgae, but for themselves, such as tetrodotoxin [1]. Moreover, microalgae accounting for about a half of the marine species, remain to be further researched and developed, provide potential natural resources for novel active substances[2].

The commercial manufacture of antibiotics has made great contributions to the health of human beings from 1950s to 1960s. However, with the wide use of antibiotics, the

Received on Aug. 18, 2008

*Corresponding author: wxqing@tjcu.edu.cn

mortality and morbidity of infectious diseases and increased again by the end of the twentieth century, owing to the pathogen bacteria acquired drug resistance. At the same time, fast-paced and undesirable-lifestyle increase the morbidity of tumor and cardiovascular disease, threatening the human health seriously. So screening and development of new antibacterial and antitumor drugs from microalgae, has become one of the hot spot fields in medicines research and development.

In this study, the antibacterial and antifungal activity of 8 microalgae extracts by different solvents were conducted, and cytotoxicities of the chosen extracts were also determined by MTT assay for new drug development.

2 Materials and methods

2.1 Culture of microalgae

Eight microalgal strains: *Chlorella pyrenoidosa Chick.*; *Isochrysis galbana* Parke 8701; *Isochrysis galbana* Parke 3011; *Isochrysis galbana* Parke H29; *Chaetoceros muelleri*; *Chaetoceros gracilis*; *Phaeodactytum tricornutum*; *Chroommonas salina,* provided by the Ocean University of China.

The strains were cultivated batchwise in flasks with f/2 medium, illuminating alternately with 12 h/12 h under 26 °C.

2.2 Preparation of microalgal extracts

2.2.1 Preparation of extracellular hydrophilic phase samples

The suspension, which was cultured for 8-10 days, was harvested in their exponential growth phase by centrifugation (4 500 rpm, 15 min). Culture supernatants of microalgae were collected, and then desalted by dialysis. After evaporation in vacuum, all the concentrated solutions were sterilezed by filtration through a 0.22 μm membrane filter. Collect the extracts as samples.

2.2.2 Preparation of intracellular lipophilic phase samples

The microalgae sediment prepared by centrifugation (4 500 rpm, 15 min) was washed with distilled water twice. Through repeated freezing, thawing and ultrasonic disruption, cells were crushed. Collect the supernatant by centrifugation after cell crush, freeze-dry them into powder for exhaustive extraction. In general, the extraction was carried out separately with ethanol, methanol/toluene (3:1, v/v), acetone, ethyl ether, ethyl acetate and 1-pentanol. After evaporation in vacuum, the extracts dissolved by Dimethyl

Sulfoxide (DMSO) respectively were sterilezed by filtration through a 0.22 μm membrane filter and stored at 4 °C until use.

2.3 Antibacterial activity assay

The antibacterial activities of all samples were tested against standard *S. aureus*, *Bacillus subtilis* and *Escherichia coli*. The extracts had the anti-*S. aureus* activity were further investigated for their antibacterial activities against five strains of MRSA isolated from the clinic. The *invitro* antibacterial test, which utilized for the investigation, is based on the agar diffusion method [3]. Therefore, nutrient agar was inoculated with a standardized quantity of a suspension of the respective organism. Sterilized paper disks (Ø 9 mm) containing the extracts (2 mg) or DMSO were transferred to the prepared agar dishes, referring to the samples or control, respectively. The diameters of resulting inhibition zones (diameter minus diameter of the paper disk) of bacteria were measured after 24 h incubation at 37 °C. Additionally, and for comparative purposes, standard vancomycin HCl was used as the positive control samples, while ampicillin was used as the negative control samples. In order to increase the sensitivity of the test system a pre-diffusion for 1 h at 4°C was granted. All the assays were carried out in duplicate.

2.4 Antifungal activity assay

Antifungal activity was determined against of both *Aspergillus niger* and *Penicillium chrysogenum*, using the paper disk assay method as previously described in the antibacterial assay (see Section 2.3). However, the diameters of resulting inhibition zones of fungi were measured after 48 h incubation at 28 °C. In order to increase the sensitivity of the test system a pre-diffusion for 1 h at 4°C was granted. All the assays were carried out in duplicate.

2.5 Antitumur activity assay

Antitumor activity was determined using MTT assay against the established cell line HeLa. In MTT (3-[4,5-dimethylthiazol-2-yl]-2,5-diphenyltetrazolium bromide) assay, the MTT substance is reduced by mitochondrial dehydrogenases in living cells to a blue-magentacolored formazan precipitate, but not in dead cells and red blood cells. Either dimethyl sulfoxide, or acidified isopropanol solution is added to dissolve the insoluble purple formazan product into a colored solution. The absorption of dissolved formazan in the visible region correlates with the number of intact alive cells, to calculate survival and inhibition rate of tumor cells.

Cells were seeded at 5×10^3 cells/well in 96-well plate and pre-incubated for 24 h to allow adhesion to the substrate. Each well was either treated with 100 μL samples

solutions or without. Negative control group (without sample), blank group (a blank containing complete medium without cells), sampling groups (treat with samples) were set. All the assays were carried out in triplicate. Following 24 h incubation with samples, 10 μL of 5 mg/ml MTT solution reagent was added to each well and incubated for 4 h. The purple-blue MTT formazan precipitate was dissolved in 150 μL/well of DMSO. The absorbance was determined using microplate reader at 570 nm.

3 Results

3.1 Antibacterial and Antifungal activity

All the extracellular hydrophilic phase extracts didn't show any antibacterial or antifungal activities. The results of the antimicrobial screening assays of intracellular lipophilic phase extracts are presented in Tab. 1. The results showed that all the microalgae had different degrees of antibacterial activity against one or more microbe-tested.

As shown in Tab. 1, the selected gram-positive bacteria proved to be more susceptible than the gram-negative ones to be inhibited. Of the 48% microalgal samples, approximately 68.75% and 77.08% of the extracts showed the antibacterial activity against *S. aureus* and *Bacillus subtilis*, respectively. Contrary to this, only 31.25% of the extracts showed the antibacterial activity against *Escherichia coli*. Nevertheless the extracts of *Phaeodactytum tricornutum*, *I. galbana* Parke 8701 and *Chroommonas salina* also showed considerable effects against gram-negative bacteria *E. coli*. Otherwise, the effects against bacteria were better pronounced than those against the fungi (Tab. 1). Nevertheless there were some effects for the 1-Pentanol extracts of *Isochrysis galbana* Parke 3011, *Isochrysis galbana* Parke H29 and *Chaetoceros* muelleri also against both *Aspergillus niger* and *Penicillium chrysogenum*.

The results of the anti-MRSA screening assays are presented in Tab. 2. As shown in Tab. 2, seven microalgaes with the exception of *Chaetoceros gracilis* exhibited variable degrees of anti-MRSA activity against one or more of the tested organisms. The results indicated that 56.47% of the extracts had the *anti-S. aureus* activity as well as against MRSA. In particular, the extracts of *Chaetoceros muelleri* , *Isochrysis galbana* Parke H29 and *Chroommonas salina* could display the considerable antibacterial activity against MRSA, and the acetone extracts of *Isochrysis galbana* Parke H29 showed the strongest activity (18 mm).

Tab. 1 Antibacterial activity of the crude extracts of 8 microalgaes in a concentration of 2 mg per paper disk[—a]

Microalgae	Extract method	*S.aureus*	*B.subtilis*	*E.coli*	*A.niger*	*P.chrysogenum*
Chlorella pyrenoidosa Chick.	Ethanol	+	+	—	—	—
	Methanol/Toluene (3:1,v/v)	+	+	—	—	—
	Acetone	+	—	—	—	—
	1-Pentanol	—	+	+	—	—
	Ethyl acetate	—	+	—	—	—
	Ethyl ether	+	—	—	—	—
Phaeodactytum tricornutum	Ethanol	—	+	—	—	—
	Methanol/Toluene (3:1,v/v)	—	+	—	—	—
	Acetone	—	+	—	—	—
	1-Pentanol	+	++	++	—	—
	Ethyl acetate	+	+	—	—	—
	Ethyl ether	—	—	—	—	—
Chaetoceros muelleri	Ethanol	+	—	—	—	—
	Methanol/Toluene (3:1,v/v)	+	—	—	—	—
	Acetone	+	++	—	—	—
	1-Pentanol	—	+	+	—	—
	Ethyl acetate	+	+	—	—	—
	Ethyl ether	+	+	—	—	—
Chaetoceros gracilis	Ethanol	+	+	—	—	—
	Methanol/Toluene (3:1,v/v)	+	+	—	—	—
	Acetone	+	+	—	—	—
	1-Pentanol	—	+	+	—	—
	Ethyl acetate	—	—	—	—	—
	Ethyl ether	+	+	—	—	—
Isochrysis galbana Parke 3011	Ethanol	—	—	—	—	—
	Methanol/Toluene (3:1,v/v)	—	+	—	—	—
	Acetone	+	+	—	—	—
	1-Pentanol	++	++	+	++	+
	Ethyl acetate	+	+	—	—	—
	Ethyl ether	—	+	—	—	—
Isochrysis galbana Parke 8701	Ethanol	++	+	+	—	—
	Methanol/Toluene (3:1,v/v)	++	++	+	—	—
	Acetone	+	+	+	—	—
	1-Pentanol	—	+	+	—	—
	Ethyl acetate	++	+	—	—	—
	Ethyl ether	+	+	+	—	—
Isochrysis galbana Parke H29	Ethanol	++	+	—	—	—
	Methanol/Toluene (3:1,v/v)	++	+	—	—	—
	Acetone	++	+	+	—	—
	1-Pentanol	++	++	+	++	++
	Ethyl acetate	+	+	—	—	—
	Ethyl ether	+	+	—	—	—
Chroommonas salina	Ethanol	++	—	—	—	—
	Methanol/Toluene (3:1,v/v)	++	—	—	—	—
	Acetone	++	+	+	—	—
	1-Pentanol	+	+	+	—	—
	Ethyl acetate	—	—	++	—	—
	Ethyl ether	—	—	—	—	—

—a: (—) No activity, (+) weak activity (3–8-mm halo), (++) good activity (8–20-mm halo).

3.2 Detection of anti-tumor activity

The cytotoxicity detection results of 6 kinds of concentrated extracellular hydrophilic extracts on HeLa cell line are presented in Tab. 3. All the assays were carried out in triplicate. To draw comparisons, each sample's OD value were converted to inhibition rate as the following equation.

$$\text{Growth inhibition rate of tumor cells} = \left(1 - {}^{A}/_{B}\right) \times 100\%$$

A: experimental wells OD value; B: controlled wells OD value.

As shown in Tab. 3, among 6 microalgal extracts, hydrophilic extracts of *Isochrysis galbana* Parke 3011 had strongly inhibited the growth of Hela cells. While the extracts of *Chlorella pyrenoidosa Chick* and *Phaeodactytum tricornutum* also showed considerable effects against this tumor cell line. Therefore, these 3 microalgaes secrete active substances in metabolic process.

The cytotoxicity detection results of 7 kinds of extractions of intracellular lipophilic phase on HeLa line are presented in Tab. 4. As shown in Tab. 4, methanol/toluene extracts of *Isochrysis galbana Parke* 8701, ethanol extracts and methanol/toluene extracts of *Chaetoceros muelleri*, exhibited certain extent cytotoxicity against HeLa cell line. Lipophilic samples of *Chroommonas salina*, *Phaeodactytum tricornutum* and *Chaetoceros gracilis* didn't show any cytotoxicity against this tumor cell line. 80% extracts of *Isochrysis galbana* Parke H29 and *Isochrysis galbana* Parke 3011 showed comparative cytotoxicities. Especially five extracts of *Isochrysis galbana* Parke H29, and 1-pentanol extract of *Isochrysis galbana* Parke 3011, exhibited considerable strong antitumor activities against HeLa.

4 Discussions

4.1 Antibacterial and Antifungal activity

A lipophilic antibacterial substance named chlorellin produced by *Chlorella fulgaris* was reported to be an autoinhibitor of the algae when it was excreted in the culture medium [4]. Afterward, the screening of antimicrobial activity on Cyanobacteria, Chlorophyta, Diatom and Dinoflagellate were studied [5-7]. In particular, some antimicrobial compounds have been identified with for instantly polysaccharide, chlorellin, phenols, peptide, et al. [8]. We were able to show that eight microalgal strains cultivated under laboratory conditions produce substances with antibacterial activity. The ability of the

microalgae to produce antibiotic compounds could be an advantage for their survival in their natural environment [9]. Several solvents were used for the extraction of lipophilic phase in this study. Our data revealed that considerable inhibition zones were observed for the ethanol, acetone, 1-Pentanol, ethyl acetate, and methanol/toluene extracts. Therefore, the compounds responsible for the antibacterial activity are lipophilic but not hydrophilic. And the results indicated that the different antibacterial/antifungal compounds are depending on the different solvents extraction.

Tab. 2 Anti-MRSA activity of the crude extracts of 7 microalgaes in a concentration of 2 mg per paper disk[-b]

Microalgae	Extract method	MRSA1	*S.sciuri*	MRSA3	MRSA4	MRSA12
Chlorella pyrenoidosa Chick	Ethanol	—	—	—	—	+
	Methanol/Toluene (3:1, v/v)	—	—	—	—	+
	Acetone	—	—	—	—	+
Phaeodactytum tricornutum	Ethyl acetate	—	—	—	—	+
Chaetoceros muelleri	Ethanol	++	+	++	—	++
	Methanol/Toluene (3:1, v/v)	++	—	+	—	++
	Acetone	—	—	—	—	+
	Ethyl acetate	++	—	+	—	++
Isochrysis galbana Parke 3011	Ethyl acetate	—	+	—	—	+
Isochrysis galbana Parke 8701	Ethyl acetate	—	—	+	—	++
Isochrysis galbana Parke H29	Ethanol	—	—	—	+	—
	Methanol/Toluene (3:1, v/v)	++	—	++	++	++
	Acetone	++	++	++	++	++
	Ethyl acetate	++	++	++	++	++
Chroommonas salina	Ethanol	+	++	++	++	++
	Methanol/Toluene (3:1, v/v)	++	+	++	—	++
	Acetone	++	+	++	+	++

-b: (- No activity, (+) weak activity (3-8-mm halo), (++) good activity (8-20-mm halo).

Tab. 3 Antitumor activity of extracellular hydrophilic phase extracts against HeLa cells[-c]

8	HeLa cell line
	Inhibition rate / %
Chlorella pyrenoidosa Chick	65.87%
Phaeodactytum tricornutum	60.20%
Chaetoceros muelleri	—
Chaetoceros gracilis	—
Isochrysis galbana Parke 3011	90.63%
Isochrysis galbana Parke 8701	—

-c: (-) No activity

Summarizing the results it can be concluded that these microalgaes are an interesting source for biologically active compounds that may be applied for prophylaxis and therapy of bacterial diseases additionally or instead of commercial antibiotics. In

particular, *Isochrysis galbana* Parke 3011, *Isochrysis galbana* Parke H29, *Chaetoceros muelleri,* and *Chroommonas salina* exhibited considerably antibacterial activity against MRSA, proved to be a new potential source of anti-MRSA substances.

Tab. 4 Antitumor activity of intracellular lipophilic phase extracts against HeLa cells[-d]

Microalgae	Extract method	HeLa
Isochrysis galbana Parke H29	Ethanol	90.83%
	Methanol/Toluene (3:1, v/v)	—
	Acetone	96.45%
	1-Pentanol	95.91%
	Ethyl acetate	93.79%
	Ethyl ether	90.16%
Isochrysis galbana Parke 3011	Ethanol	23.86%
	Methanol/Toluene (3:1, v/v)	60.14%
	Acetone	20.80%
	1-Pentanol	96.21%
	Ethyl acetate	28.85%
	Ethyl ether	—
Isochrysis galbana Parke 8701	Ethanol	—
	Methanol/Toluene (3:1, v/v)	25.52%
	Acetone	—
	1-Pentanol	—
	Ethyl acetate	—
	Ethyl ether	—
Chaetoceros muelleri	Ethanol	14.39%
	Methanol/Toluene (3:1, v/v)	21.70%
	Acetone	—
	1-Pentanol	—
	Ethyl acetate	—
	Ethyl ether	—
Chaetoceros gracilis	Ethanol	—
	Methanol/Toluene (3:1, v/v)	—
	Acetone	—
	1-Pentanol	—
	Ethyl acetate	—
	Ethyl ether	—
Phaeodactytum tricornutum	Ethanol	—
	Methanol/Toluene (3:1, v/v)	—
	Acetone	—
	1-Pentanol	—
	Ethyl acetate	—
	Ethyl ether	—
Chroommonas salina	Ethanol	—
	Methanol/Toluene (3:1, v/v)	—
	Acetone	—
	1-Pentanol	—
	Ethyl acetate	—
	Ethyl ether	—

-d: (-) No activity

4.2 Detection of anti-tumor activity

Nowadays there are many reports about antitumor activity of *Porphyridium cruentum.* Wen's study indicates that *Porphyridium cruentum* can synthesize various valuable bioactive substances, including Phycobiliproteins, high unsaturated fatty acid and extracellular polysaccharide [10]. There are a lot of reports about antitumor activity of these

three substances. In this study, three extracellular hydrophilic phase samples showed considerable inhibitory effect on proliferation of HeLa cells. It may be extracellular polysaccharide, chlorellin or other active substance in *Chlorella pyrenoidosa Chick*, *Phaeodactytum tricornutum*, and *Isochrysis galbana* Parke 3011. In particularly, *Isochrysis galbana* Parke 3011, which exhibited the best inhibition, may secrete the most efficient active substances in metabolic process.

In previous study, it is indicated that abundant fatty acids, such as DHA and EPA, were contained in *Isochrysis galbana*, *Phaeodactytum tricornutum* and *Chaetoceros* muelleri[11, 12]. Currently, little study has been reported about the effect antimicrobial or antitumor activity of *Isochrysis galbans*, while only some works about growth conditions and cultivation had been researched [13, 14]. Out experimental results indicate that the intracellular lipophilic extracts of *Isochrysis galbans* Park H29 and *Isochrysis galbans* Park 3011 both showed considerable cytotoxicity against the target tumor cells. Since *Isochrysis galbans* grows easily, it can not only be used as a source of high unsaturated fatty acid, but also be used as a source of antitumor drugs probably.

Current cancer treatments have many harmful side effects, since commonly used antineoplastic drugs target all rapidly dividing cells, rather than solely cancerous cells. Our data revealed that several extracts of these strains showed extraordinary cytotoxicity against HeLa cells. Obviously, further research is needed to evaluate their properties fully.

The overall results of this study indicate that the extracts from the microalgae represent a potential source of marine drugs. At this stage of our study, we can deduce that the extracellular hydrophilic and intracellular lipophilic extracts appeared to be the most promising part to be considered as antimicrobial and antitumor medicines. However, further investigations will be necessary to confirm our hypothesis. Prior further research regarding toxicity, stability and metabolism of microalgae and microalgae components must be undertaken.

Acknowledgements

This work is supported by the Natural Science Foundation of Tianjin (Grant No. 08JCZDJC16600). We also would like to thank Key Development Programs of Tianjin in Science and Technology (Grant No. 06YFGZNC04200).

References

[1] Hikmet K, Beril S A, Tahir A, et al. characteristics and importance [J]. African Journal of Biotechnology, 2004, 3(12): 667 - 674.

[2] Molina E, Grima E H, Belarbi F G, et al. Recovery of microalgal biomass and metabolites: process options and economics [J]. Biotechnology Advances, 2003, 20: 491 - 515.

[3] Collins C M, Lyne P M, Grange J M. Antimicrobial sensitivity and assay tests [M]. London: Collins and Lyne's Microbiological Methods. Butterworths, UK, 1989.

[4] Scutt J E. Autoinhibitor production by chlorella vulgaris [J]. Amer. Jour. Bot., 1964, 51(6): 581 - 584.

[5] Ordog V, Stirk W A, Lenobel R, et al. Screening microalgae for some potentially useful agricultural and pharmaceutical secondary metabolites [J]. Journal of Applied Phycology, 2004, 16: 309 - 314.

[6] Zhang C W. Active substances in microalgae [J]. Chinese Journal of Marine Drugs, 1992, 3: 20 - 29.

[7] Paul G K, Matsumori N, Konoki K, et al. Chemical structures of amphidinols 5 and 6 isolated from marine dinoflagellate *Amphidinium klebsii* and their cholesterol-dependent membrane disruption [J]. J. Mar. Biotechnol, 1997, 5: 124 - 128.

[8] Jang H X. Antimicrobial activity and biochemical analysis of lipophilic extracts from microalgae [D]. Fuzhou: Fujian Normal University, 2003, 10 - 12.

[9] Teuscher E, Lindequist U, Mundt S. Cyanobakterien, Quellen biogener Wirkstoffe [J]. Pharm. Ztg. Wiss, 1992, 137: 57 - 69.

[10] Wen S H, Wang C H. Effect of light and culture time on the fatty acid composition of *Porphyridium cruentum* PUFA [J]. Chinese Journal of marine drugs, 2000, 73(1): 47 - 50.

[11] Viso A C, Marty J C. Fatty acids from 28 marine microalgae [J]. Phytochemistry, 1993, (6): 1 521 – 1 533.

[12] Volkman J K, Jeffrey S W, Nichols P D, et al. Fatty acid and lipid composition of 10 species of microalgae used in marine culture [J]. J. ExpMar. Biol. Ecol., 1989, 128: 219 - 240.

[13] Wang C L. Semi-continuous cultivating for *Isochrysis galbans* in sealed plastic bag [J]. Fishery Modernization, 2002, 5: 14 - 16.

[14] Li Z X, Liu X P. The effect of different nitrogen sources to the growth characteristics of *Isochrysis galbana* Parke [J]. Chinese Agricultural Science Bulletin, 2010, 26(1): 303 - 307.

从培养的微藻中初步筛选抗菌和抗肿瘤活性物质

邓 伟，王雪青，宋文军

（天津食品与生物技术重点实验室，天津商业大学 生物技术与食品科学学院，天津 300134）

摘 要：从 8 种微藻中制备水溶和脂溶性的提取物，用来筛选抗菌和抗肿瘤活性。抗菌活性是用抑菌圈法（细菌用金黄色葡萄球菌，枯草芽孢杆菌和大肠杆菌为指示菌，真菌用黑曲霉和产黄青霉为指示菌）。实验选用的所有的微藻均有不同程度的抗一种或多种菌活性，抗金黄色葡萄球菌微藻提取物中的 57.14%有抗耐甲氧西林金黄色葡萄球菌活性，采用 MTT 法体外检测藻提取物对 HeLa 肿瘤细胞系的细胞毒活性：大多数的提取物有抑制肿瘤细胞增长的作用，尤其是球等鞭金藻 3011 和 H29 显示有强的抗 HeLa 生长的作用，结果表明，微藻是一种十分有潜力用来筛选抗菌和抗肿瘤的新药源。

关键词：微藻；筛选；抗菌；抗肿瘤

Heavy metal distribution patterns and environmental quality assessment of the mariculture areas in Nanao, Shantou

ZHOU Yan-hui [1], BAI Yan [1*], LI Lian-sheng [1], YANG Yu-feng [2*]

1. *Department of Chemistry, Jinan University; Guangzhou* 510632, *Guangdong Province, China;*
2. *Institute of Hydrobiology of Jinan University, Key Laboratory of Eutrophication and Red Tide Control, Education Department of Guangdong Province, Guangzhou* 510632, *Guangdong Province, China*

Abstract: The Fe, Zn, Mn and Pb concentrations in the seawater dissolved phase were investigated in the sea-surface microlayer (SML), subsurface water (SSW) and bottom water (BW) samples collected at of three mariculture areas of the Nanao Island ocean zone. The results showed that the SML and the BW were important compartments for these heavy metals in the mariculture areas and the concentrations varied from 23.0 μg/L to 268.0 μg/L(Fe), 11.0 μg/L to 82.2 μg/L(Zn), 1.5 μg/L to 11.0 μg/L(Mn) and 6.0 μg/L to 40.5 μg/L(Pb) in SSW, while a clear enrichment is observed in the SML, where these ranged from 27.5 μg/L to 286.5 μg/L(Fe), 13.5 μg/L to 89.0 μg/L(Zn), 3.0 μg/L to 12.0 μg/L(Mn) and 7.0 μg/L to 46.0 μg/L(Pb). The enrichment factors were in the range of 1.07 - 1.39 which showed a slight enrichment. The average enrichment factors of Fe, Zn, Pb and Mn were 1.18, 1.13, 1.12 and 1.30, respectively. The average enrichment factors in shellfish, fish and gracilaria lemaneaformis farming areas were 1.26, 1.19 and 1.11, respectively, which showed that the surface activity was highest in the shellfish farming area. Furthermore, the heavy metals concentrations were lowest in the gracilaria lemaneaformis farming area. The results of single factor contamination index showed that the investigated areas were slightly contaminated with Zn, while the partial farming areas were seriously contaminated with Pd during a certain period of time.

Keywords: sea-surface microlayer, enrichment factors, heavy metal, single factor contamination index

The seawater environment is closely related to the organism activities. The effect of seawater environment quality on the organism activities has attracted scientists' attentions [1-3]. The trace elements, such as Fe, Mn, Pb, Zn and so on, play an important role in the seawater eutrophication and the organisms metabolism [3, 4]. Fe is one of the transition elements which are utilized frequently by the biosphere. Moreover, Fe is basic nutrient for

Received on Sep. 10, 2010

*Corresponding author: tbaiyan@jnu.edu.cn, tyyf@jnu.edu.cn

eukaryon and has promotion action on the phytoplankton growth [5]. At a certain concentration, Mn can enhance the growth of phytoplankton, and has synergistic effect with Fe [6]. The high concentration of Zn and Pb will induce toxicity to the organisms [7, 8].

The sea-surface microlayer is the interface between the world's atmosphere and hydrosphere where important physical, chemical, and biological processes take place. Some of its characters are different from main body of seawater, so the sea-surface microlayer can be consider as a specific micro-ecosystem [9]. The concentrations of chemicals in the sea surface microlayer, such as nutrient salts, organic compounds and traces metals, are different from main body of seawater, and these chemicals show different degrees of enrichment [10-12]. A majority of phytoplankton and secondary metabolism products amplified by organism has surface activity and can complex with trace metals. Some marine bacteria and epiphytes can produce ligands which also has surface activity and complex with trace metals. Moreover, after the ligand-metal complexes formed, their surface activity would not disappear, and the complexes would still give rise to surface enrichment by Gibbs adsorption, which results in the enrichment of dissolved trace metal-organic complexes in the sea-surface microlayer [13, 14].

In this study, the heavy metal concentrations in the seawater dissolved phase were investigated in the sea-surface microlayer (SML), subsurface water (SSW) and bottom water (BW) of three mariculture areas in Nanao, Shantou. The objective of this study was to investigate the enrichment effect of heavy metals in the SML and assess the environmental quality in shellfish, fish and gracilaria lemaneaformis farming areas.

1 Materials and methods

1.1 Sample collection and preparation

Sampling sites were in the mariculture areas of Nanao, Shantou (Fig. 1). The depths of seawater at the sampling sites were listed in the Tab. 1. The samples were collected during the periods of May 2 to May11, 2007 and Feb. 26 to Mar. 8, 2008.

Tab.1 Conditions of sampling sites

Area	Gracilaria lemanea formis farming area / St.A	Fish farming area / St.B	Shellfish farming area / St.C
Location	N23°29.080′, E117°06.222′	N23°28.621′, E117°06.137′	N23°28.114′, E117°05.846′
Depth / m	5.04	4.77	2.00

Sea-surface microlayer (SML) samples were collected by pulling the glass plate (60 cm × 40 cm × 0.5 cm) at the rate of 20 cm/s. The sampling thickness was about 50 μm.

Sub-surface water (SSW) samples were collected by immerging 5 L organic glass water collectors to 1 m depth. Bottom water (BW) samples were collected by using 5 L organic glass water collectors at 1 m above the seabed sediment.

The polyethylene bottles were dipped in nitric acid solution (HNO_3: H_2O = 1:1) for 24 hours, then cleaned thoroughly with deionized water and dried in air prior to use. All samples were acidified with nitric acid to a pH of 1.5 - 2.0 after sampling. All samples were airproofed in the polyethylene bottles and were stored in ice onboard and at low temperature (4 °C - 15 °C) in the laboratory.

Fig.1 The location of sampling sits

(1.Tayu Island; 2.Lieyu Island; 3.Nan'ao Island; 4.Shen'ao Salt Field; 5. Ring Road)

1.2 Analysis

A volume of 1 mL 5 mol/L nitric acid was added into 500 mL water sample, and then diluted the sample with deionized water to 10.00 mL. The concentrations of heavy metals were determined by inductively coupled plasma atomic emission spectrometer (Optima 2000 DV). The relative standard deviation (RSD) and the recovery were used to control the precision and accuracy of measurements. The RSD was lower than 5%, and the recovery was 90% - 125%.

Enrichment factors (*EF*) were calculated as the ratio of concentrations in the SML

sample to that of the corresponding SSW sample [15], according to following formulas:

$$EF = c_{SML} / c_{SSW}$$

where c_{SML} and c_{SSW} were the concentrations of heavy metals in the SML and in the SSW, respectively.

Single factor pollution index (p_i) were calculated, according to following formulas: $p_i = c_i / s_i$ [3], where c_i was the concentration of heavy metals measured, and s_i was the standard value or the background value. In this paper, Sea Water Quality Standard (GB 3097-1997) was used as the assessment standard, that is Pb< 0.005 mg/L and Zn< 0.050 mg/L (the second category, the mariculture area), i.e. S_{Pb}=0.005 mg/L, S_{Zn}=0.050 mg/L.

2 Results and discussion

2.1 Distribution patterns of heavy metals in the mariculture areas

Dissolved heavy metals, Fe, Zn, Mn and Pb were detected in different seawater levels of three mariculture areas. The data were treated by the Grubbs methods. After discarding the abnormal values, the results were listed in the Tab. 2. The concentrations of the heavy metals in the SML were higher than those in the SSW, which showed the enrichment effect in the SML. These heavy metals enrichments in the SML were generally low with *EF* values from 1.07 to 1.39. The *EF* values were low with mean of 1.26, 1.19 and 1.11 in shellfish, fish and gracilaria lemaneaformis farming areas, respectively. The enrichment phenomenon in the shellfish farming area was the most obvious, which indicated the surface activity of shellfish farming area was highest. The average *EF* values of Fe, Zn, Pb and Mn were 1.18, 1.13, 1.12 and 1.30, respectively, which showed that the enrichment effect of Mn was the most obvious.

During the period of May 2 to May 11, 2007, the order of heavy metals concentrations (except Pb) for differential seawater levels was shellfish farming area >fish farming area >gracilaria lemaneaformis farming area. However, during the period of Feb. 26 to Mar. 8, 2008, these metals did not distribute in the same pattern. In general, the spatial variability of concentrations of Fe, Zn and Mn was very high when sampling dates from different mariculture areas were compared. These heavy metals concentrations (except Pb) for differential seawater levels were lower in the gracilaria lemaneaformis farming area than those in the other farming areas, which results from the fact that algae possess metal biosorption [16]. Both marine microalgae and macroalgae could adsorb heavy metals, such as Co, Cd, Ag, Cu, Zn, Mn, Pb, Au and so on. Thus, marine microalgae and macroalgae are potentially excellent heavy metal biosorbents due to their high sorption capacity and their ready availability in practically unlimited quantities in the seas and oceans[16-19].

Because of the metal sorption capability of gracilaria lemaneaformis, the metals concentrations were lower in the gracilaria lemaneaformis farming area than those in other farming areas. However, significant different patterns were found for Pb. It was detected only in the gracilaria lemaneaformis and shellfish farming areas during the period of Feb. 26 to Mar. 8, 2008, and the concentrations of Pb in differential seawater levels were much higher in the gracilaria lemaneaformis farming area than that in the shellfish farming area. It indicated that the effects of time and environment on the concentration of Pb were great in sampling farming areas.

Tab. 2 Distribution patterns of heavy metals and their enrichment factors in the mariculture areas

Element	Time	Seawater level	St.A	St.B	St.C
Fe	May 2 to May 11, 2007	SML / μg/L	38.7 ± 6.8	67.3 ± 12.3	85.4 ± 22.7
		SSW / μg/L	34.7 ± 3.9	52.7 ± 9.9	63.7 ± 9.1
		BW / μg/L	79.2 ± 13.6	79.6 ± 10.3	-
		EF	1.11	1.28	1.34
	Feb. 26 to Mar. 8, 2008	SML / μg/L	174.1 ± 27.4	180.8 ± 57.7	183.1 ± 26.6
		SSW / μg/L	157.0 ± 36.3	163.5 ± 35.8	160.3 ± 18.9
		BW / μg/L	202.3 ± 16.7	281.4 ± 47.8	-
		EF	1.11	1.11	1.14
Zn	May 2 to May 11, 2007	SML / μg/L	22.8 ± 6.3	31.6 ± 8.9	63.9 ± 14.6
		SSW / μg/L	21.1 ± 3.7	27.8 ± 7.7	52.2 ± 18.8
		BW / μg/L	31.7 ± 7.1	38.4 ± 9.3	-
		EF	1.08	1.14	1.22
	Feb. 26 to Mar. 8, 2008	SML / μg/L	21.5 ± 4.7	37.8 ± 12.5	22.3 ± 3.7
		SSW / μg/L	20.1 ± 2.3	34.8 ± 16.7	19.4 ± 3.0
		BW / μg/L	24.8 ± 7.4	47.8 ± 21.2	-
		EF	1.07	1.09	1.15
Mn	May 2 to May 11, 2007	SML / μg/L	NA	6.9 ± 0.6	9.3 ± 1.3
		SSW / μg/L	NA	5.4 ± 0.8	7.2 ± 1.2
		BW / μg/L	NA	7.6 ± 1.3	-
		EF	NA	1.28	1.29
	Feb. 26 to Mar. 8, 2008	SML / μg/L	6.1 ± 1.7	4.9 ±1.2	7.8 ± 1.0
		SSW / μg/L	5.0 ± 0.6	3.8 ± 1.2	5.6 ± 0.7
		BW / μg/L	6.8 ± 1.4	8.3 ± 1.5	-
		EF	1.21	1.32	1.39
Pb	May 2 to May 11, 2007	SML / μg/L	32.8 ± 7.2	9.6 ± 1.3	NA
		SSW / μg/L	29.8 ± 16.8	8.5 ± 1.6	NA
		BW / μg/L	34.1 ± 7.5	10.6 ± 2.3	-
		EF	1.10	1.13	
	Feb. 26 to Mar. 8, 2008	SML / μg/L	NA	NA	NA
		SSW / μg/L	NA	NA	NA
		BW / μg/L	NA	NA	-

P=0.95, n = 6-8; NA: Not Available; The bottom data wasn't detected in the St.C.

2.2 Statistics characters of the concentrations of heavy metals in the mariculture areas

The results of statistical analysis were listed in Tab. 3. The varieties of Zn and Pb

concentrations were large with a coefficient of variation around 55% and 60%, respectively, with the changes of time and location. The concentration ranges were 60.0 - 391.0 (mean170.7) μg/L for Fe, 15.0 - 116.5 (mean 38.1) μg/L for Zn, 4.5 - 14.5 (mean 7.7) μg/L for Mn and 8.5 - 47.0 (mean 22.3) μg/L for Pb in SSW, 27.5 - 286.5 (mean 122.0) μg/L for Fe, 13.5 - 89.0 (mean 34.3) μg/L for Zn, 3.0 - 12.0 (mean 7.2) μg/L for Mn and 7.0 - 46.0 (mean 23.4) μg/L for Pb in the SML, 23.0 - 268.0 (mean 115.7) μg/L for Fe, 11.0 - 82.0 (mean 29.3) μg/L for Zn, 1.5 - 11.0(mean 5.6) μg/L for Mn and 6.0 - 40.5 (mean 20.9) μg/L for Pb in the SSW. The highest concentrations of these heavy metals were found in the BW and the concentrations of these heavy metals in the BW were close to those in the SML. These results suggested that the SML and the BW were important compartments for these heavy metals in the mariculture areas. Furthermore, the statistics characters of the concentrations of heavy metals showed a clear enrichment effect in the SML.

Tab.3 Summary statistics of heavy metals concentrations in the mariculture areas

Element	Seawater level	Minimum / μg/L	Maximum / μg/L	Mean / μg/L	Standard deviation / μg/L	Variance coefficient / %
Fe	SML	27.5	286.5	122.0	38.5	31.6
	SSW	23.0	268.0	107.8	35.8	30.9
	BW	60.0	391.0	170.7	42.7	25.0
Zn	SML	15.5	89.0	34.3	17.8	51.9
	SSW	13.5	82.0	29.3	14.9	50.9
	BW	15.0	116.5	38.1	19.1	50.1
Mn	SML	3.0	12.0	7.2	2.1	29.2
	SSW	1.5	11.0	5.6	1.8	32.1
	BW	4.5	14.5	7.7	2.4	31.2
Pb	SML	46.0	7.0	23.4	13.6	58.0
	SSW	40.5	6.0	20.9	12.5	59.9
	BW	47.0	8.5	22.3	13.7	61.3

P=0.95, n = 15-20; The bottom data wasn't detected in the St.C.

2.3 Environment quality assessment on the Zn and Pb in the mariculture areas

The environment quality in the mariculture areas was assessed by single factor contamination index of Zn and Pb (Tab. 4). The pollution grades were low-level pollution p_i < 1, medium-level pollution 1≤ p_i < 3, high-level pollution 3 ≤ p_i < 6 and severe-level pollution p_i≥ 6 [3]. As shown in Tab. 4, the average contamination index p_{Zn} was lower than 1 in the three farming areas, which suggested the low level pollution. However, during the

period of May 2 to May 11, 2007, the contamination index p_{Zn} was slightly higher than 1 in the shellfish farming area, which indicated that the Zn pollution was close to the medium-level pollution. It was worthy of note that Pb had already polluted the seawater, though it was only detected in the gracilaria lemaneaformis and fish farming areas during the period of May 2 to May 11, 2007. The average contamination index p_{Pb} was 1.91 in the shellfish farming area, which suggested the medium-level pollution. In the gracilaria lemaneaformis farming area the exceeding standard rate of Pb concentration was 100% and p_{Pb} was 6.45, which suggested severe-level pollution.

Tab. 4 Single factor contamination index of Zn and Pb in the mariculture areas

Time	Seawater level	St.A		St.B		St.C	
		p_{Zn}	p_{Pb}	p_{Zn}	p_{Pb}	p_{Zn}	p_{Pb}
May 2 to May 11, 2007	SML	0.456	6.56	0.632	1.92	1.28	NA
	SSW	0.422	5.96	0.556	1.70	1.04	NA
	BW	0.634	6.82	0.768	2.12	-	-
Feb. 26 to Mar. 8, 2008	SML	0.430	NA	0.756	NA	0.446	NA
	SSW	0.402	NA	0.696	NA	0.388	NA
	BW	0.496	NA	0.956	NA	-	-
Average		0.473	6.45	0.727	1.91	0.792	NA

NA: Not Available; The bottom data wasn't detected in the St.C.

3 Conclusions

The concentrations of four heavy metals (Fe Zn Mn and Pb) in different seawater levels were variant among different farming areas, and were higher in the SML than those in the SSW. The enrichment factors were in the range of 1.07 - 1.39 which showed a slight enrichment. The SML and the BW were important compartments for these heavy metals in the mariculture areas. The concentrations of heavy metals were lower in the gracilaria lemaneaformis farming area than those in fishing and shellfish farming areas. Environmental assessment with single factor contamination index indicated that Zn pollution was slight, while Pb pollution was severe during a certain period of time.

Acknowledgement

This research was financially supported by the National Natural Science Foundation of China (No.40673062).

Reference

[1] Zhang H J, Zhang J Y, Chen Y X, et al. Research on microcystins in freshwaters with relation to environmental factors [J]. Environmental Science, 2006, 27(10):1 969 - 1 973.

[2] Wang C Y, Wang X L. Spatial distribution of dissolved Pb, Hg, Cd, Cu and As in the Bohai Sea [J]. Journal of Environmental Sciences, 2007, 19(9): 1 061 - 1 066.

[3] Sheng J J, Fan D J, Yang D F, et al. Distribution patterns of heavy metals in surface sediments of the Yangtze estuary and its adjacent areas and environmental quality assessment [J]. Environmental Science, 2008, 29(9): 2 405 - 2 412.

[4] Dang T C, Subramanian K, Jeffrey P O. Distribution of heavy metals in the dissolved and suspended phase of the sea-surface microlayer, seawater column and in sediments of Singapore's coastal environment [J]. Environ Monit Assess, 2008, 138: 255–272.

[5] Li R X, Zhu M Y. Impact of iron on the growth of natural phytoplankton community [J]. Advances in Marine Science, 2004, 22(1): 50 - 54.

[6] Li H, Miao J L, Li G Y. Effects of N, P, Fe and Mn on the growth of *Alexandrium sp*. LC3 [J]. Marine Environmental Science, 2006, 25(4): 1 - 3.

[7] Wang C Y, Wang X L, Sun B Y, et al. Ecotoxicological effect of Cu, Pb, Zn and Cd on *Prorocentrum donghaiense* Lu [J]. China Environmental Science, 2008, 28(3): 264 - 268.

[8] Wang Z Z, Liu Z Y, Lü G T, et al. Acute toxic effects of Hg^{2+}, Zn^{2+} and Cr^{6+} on Nibea albif lora juvenile[J]. Journal of Fishery Sciences of China, 2005, 12(6):745 - 750.

[9] Yu Z G, Zhang Z B, Liu L S. Study progresses on sea surface microlayer [J]. Marine Environmental Science, 2000, 19(3): 75 - 80.

[10] Oliver W, Jeffrey P O. A review of pollutants in the sea-surface microlayer (SML): a unique habitat for marine organisms [J]. Marine Pollution Bulletin, 2004, 48:1 016 - 1 030.

[11] Yang Y F. Comparative studies on zooplankt on community between the sea surface microlayer and the subsurface microlayer in Daya Bay [J]. China Progress in Nature Science, 2005, 15(8):53 - 59.

[12] Carlos G, Nuria G F, Josep M, et al. Occurrence and fate of polycyclic aromatic hydrocarbons in the coastal surface microlayer [J]. Marine Pollution Bulletin, 2007, 54: 186 - 194.

[13] Wu Z J, Li J, Ding H B, et al. Effects of plankton on the enrichment of some chemical substances in the sea surface microlayer [J]. Transactions of Oceanology and Limnology, 1997, 1: 43 - 47.

[14] Liu C Y, Zhang Z B, Zhang A H, et al. Study on metal complexing ligands concentrations inseveral waters of China coast [J]. Acta Oceanologica Sinica, 2005, 27(2): 54 - 62.

[15] Oliver W, Michael H. The gelatinous nature of the sea-surface microlayer [J]. Marine Chemistry, 2008, 110: 89 - 97

[16] Wang J L, Chen C. Biosorbents for heavy metals removal and their future [J]. Biotechnology

Advances, 2009, 27: 195 - 226.

[17] Yin P H, Zhao L, Yu Q M, et al. Biosorption of lead, copper and cadmium by marine macroalgae [J]. Marine Environmental Science, 2000, 19(3):11 - 15.

[18] Ilhami T, Guolay B, Emine Y, et al. Equilibrium and kinetic studies on biosorption of Hg(II), Cd(II) and Pb (II) ions onto microalgae Chlamydomonas reinhardtii [J]. Journal of Environmental Management, 2005, 77: 85 - 92.

[19] Wang X, Xu L R, Chen L D, et al. Characteristics and function of macroalgae biosorption technology to metal ion [J]. Journal of Oceanography in Taiwan Strait, 2003, 22(1): 120 - 124.

汕头南澳海水养殖区不同水层重金属的分布和环境质量评价

周艳晖[1]，白 燕[1*]，李联盛[1]，杨宇峰[2*]

（1. 暨南大学化学系，广东 广州 510632；2. 水生生物研究所，水体富营养化与赤潮防治广东省教育厅重点实验室，广东 广州 510632）

摘 要：利用电感耦合等离子发射光谱（ICP-AES）方法测定了汕头南澳海水养殖区溶解态的重金属在不同水层中的分布。在龙须菜、鱼类和贝类养殖水域检出Fe、Zn、Mn、Pb等重金属，其中微表层（SML）和底层（BW）是这些重金属的主要存在区域。这些重金属在微表层（SML）中的浓度（Fe 27.5 – 286.5 μg/L，Zn13.5 – 89.0 μg/L，Mn 3.0 – 12.0 μg/L，Pb 7.0 – 46.0 μg/L）明显高于其在亚表层（SSW）中的浓度（Fe 23.0 – 268.0 μg/L，Zn 11.0 – 82.2 μg/L，Mn1.5 – 11.0 μg/L，Pb 6.0 – 40.5 μg/L），表明微表层发生富集现象，富集系数（EF）在1.07 – 1.39 范围内属于轻微富集，其中Mn的平均富集系数最高（*EF* = 1.30），其他金属相近。平均富集系数以贝类养殖水域最高（1.26），其次为鱼类养殖水域（1.19），龙须菜养殖水域最低（1.11），表明贝类养殖水域表面活性最大。龙须菜养殖水域重金属含量较其他养殖水域低。单因子污染评价显示，南澳养殖海域已经受到Zn低度污染，部分水域在一定时间内Pb的污染严重。

关键词：微表层；富集系数；重金属；单因子污染指数

Seasonal variations in species composition and abundance of tintinnids in Shantou coastal water, China

LIU Hua-xue [1, 3], HUANG Liang-min [1], TAN Ye-hui [1], SONG Xing-yu [1], HUANG Jian-rong [2]

1.*South China Sea Institute of Oceanography ,China Academy of Science, Guangzhou* 510301, *Guangdong Province, China;*

2. *School of Life Sciences, Sun Yat-Sen University, Guangzhou* 510275, *Guangdong Province, China*

3. *Graduate University of China Academy of Science, Beijing* 100049, *China*

Abstract: Two cruises were conducted to study the composition and seasonal variation of tintinnids (Protozoa: Ciliata) in Shantou coast water during spring and fall. Remarkable seasonal variations in environmental parameters, and tintinnids composition were observed. Tintinnids samples were enumerated and identified from 5 stations. 14 species belonging to 7 genuses of tintinnids were identified, and the dominate species was *Leprotintinnus simple* in these season. High tintinnids diversity and low abundance occurred in the fall, and on the contrary, low tintinnids diversity and high abundance occurred in the spring. No significant correlation occurred between tintinnids abundance and nutrients. Tintinnids abundance showed negative relationship with salinity (r^2=0.63, $P < 0.05$), maybe this was due to the cold raised water carried sum nutrients rise to the surface water in the fall, rich nutrients and high phytoplankton biomass decrease the importance of tintinnids in the energy flow of aquatic food web.

Keywords: tintinnids, composition, distribution, Shantou coast

Introduction

Tintinnids ciliates are important component of ciliate community and occur in all the oceans of the world [1]. Investigations of feeding revealed that tintinnids ciliates ingest a large variety of pico- and nano-sized prey, ranging in size from about 2 μm to particles about half the diameter of their lorica oral openings [1]. Due to their ubiquitous distribution, small size, and rapid metabolic and growth rates (Verity, 1985; 1987), they are undoubtedly considered to play an important role in transferring the production in micro food web [2-5].

Received on May 25, 2010

Corresponding author: hxliu@scsio.ac.cn

Shantou is on the southeast end of the mainland of China, includes the mainland part and many islands. As a result of excessively rapid population growth and economic development, the pressure imposed by population on the environment was heightened. To meet the demands of the increasing population, the environment and natural resources were overexploited and destroyed. The composition and seasonal variation of tintinnids in Shantou coast water during spring and fall was still unknown. Here we aimed to determine the community structure and distribution of tintinnids in eutrophic environment, to gain insight into the function of tintinnids in Shantou coast water.

1 Material and method

1.1 Field sampling

5 stations were designed in Shantou coastal water (Fig. 1), and S_1 located at the channel between Nanao Island and Zelin bay; S_2、S_3、S_4 were located at high frequency area of HABs, and S_5 was far away from the Shantou coastal water.

Fig. 1 Sampling station in Shantou coast water

Two cruises were conducted in spring and fall, 2007. Seawater samples for analysis of nutrients and chlorophyll a were taken using 5 L GO FLO bottles from the surface layers, and other samples were collected according to the methods the sampling tools of "The specialties for oceanography survey"(GB12763-91,China). An YSI 6600 Water Quality Monitoring System was employed to collect the data for temperature (*T*) and salinity (*S*). Inorganic nutrients (NO_3^-, NO_2^-, NH_4^+, and PO_4^{3-}) were also analyzed according to the "The

specialties for oceanography survey" (GB12763-91, China). Seawater sample for the analysis of chlorophyll a (Chl a) were immediately filtered through GF/F filters (whatman, 25 mm), which were stored at -20 °C. The phytoplankton pigments retained on GF/F filters was extracted in 90% acetone. The Chl a concentration in the extract was measured before and after acidification with a fluorometer (Turner 10-AU-005). Tintinnids samples were collected from the surface layer, Samples were preserved by adding the acid lugol's solution (final concentration 2%), and then stored at 4 °C in the dark before tintinnids identification.

1.2 Laboratory analysis

For enumeration, tintinnids samples were settled down for 24 h in their bottles in the dark at 4 °C, and the upper 900 ml of the sample was slowly siphoned off. The bottom 100 ml of the sample was transferred into settling chambers to settle for 24 h before examined [6]. Tintinnids were identified using lorica morphology and the species descriptions according to literatures [7-10].

Pearson correlation analysis and multivariate regression were applied to find the potential relationship between the distribution of tintinnids and environmental variable by SPSS 12.0. Diversity index (*H'*) was calculated using the Shannon-Wiener diversity index (Shannon, 1948).

$$H' = \sum_{1}^{i} P_i \log_2 P_i$$

Where *i* was the sample number and P_i is the proportion of the total count represented by the *i* th species.

2 Result

2.1 Environment parameters

In spring, mean surface seawater temperature was 22.9 °C, and mean surface seawater salinity was 29.2, and Mean surface Chl a concentration was 0.59 mg/m^3. In fall, mean surface seawater temperature 21.3 °C, which was lower than in that spring. In fall, mean surface seawater salinity was 31.9, and mean surface Chl a concentration was 1.30 mg/m^3.

In spring, mean nitrate concentration was 13.57 ± 9.96 μm/L, and mean silicate concentration was 22.06 μm/L ± 13.72 μm/L. In fall, mean nitrate concentration was 19.11 μm/L ± 3.45 μm/L, mean silicate concentration was 43.39 μm/L ± 5.45 μm/L, which

were higher than those in spring.

2.2 Tintinnids composition and distribution

14 species tintinnids belonging to 7 genus were identified (Tab. 1), among which, *Tintinnopsis* was the most abundant genus in terms of species (6).

Tab. 1 Tintinnids species identified in Shantou coast

Genus	Species
Codonella	*Codonella rap*
Codonellopsis	*Codonellopsis borealis*
	Codonellopsis morchella
Favella	*Favella companula*
Leprotintinnus	*Leprotintinnus simple*
Stenosemella	*Stenosemella pacifica*
Tintinnopsis	*Tintinnopsis beroidea*
	Tintinnopsis minuta
	Tintinnopsis oriental
	Tintinnopsis radix
	Tintinnopsis schotti
	Tintinnopsis tubulosa
Undella	*Undella ostenfedi*
	Undella turgida

Fig. 2 showed the seasonal variation of tintinnids relative parameters in Shantou coast water. In spring, mean species number was 4.6, and dominate species was *Leprotintinnus simple* (71.82%), followed *Tintinnopsis beroidea* (9.66%). In fall, mean species number was 5.6, which was higher than the spring, and the dominate species was *Leprotintinnus simple* (42.48%), followed *Tintinnopsis tubulesa* (14.72%). In spring, Tintinnids abundance ranged 120 - 2 265 Cell/L, mean abundance was 1 501 Cell/L. In fall, Tintinnids abundance ranged 516 - 1 520 Cell/L, mean abundance was 845.2 Cell/L Mean diversity index in the spring (1.25) was lower than that in fall (2.15).

3 Discussion

3.1 Seasonal variation of tintinnids

Seasonal variation of temperature and salinity were controlled by river runoff and upwelling in Shantou coast. Southwest monsoon prevailed from May to September; northeast monsoon prevailed from November to March. Generally, river runoff was stronger in spring than that in fall, and on the contrary, upwelling phenomena was stronger

in fall than that in spring. In the Shantou coast, surface seawater temperature was lower in the fall than that in spring, and surface seawater salinity was higher in fall. Cold upwelling water rise to the surface, and carries sum nutrients stimulating the phytoplankton growth, and sustains the higher phytoplankton biomass. Tintinnids play more important role in the microbial food web than the classic food web. As rich nutrients and high chlorophyll a concentration occurred in fall, the role tintinids played in fall was not as important as in spring. High tintinnids diversity and low abundance in fall, and on the contrary, low tintinnids diversity and high abundance in spring.

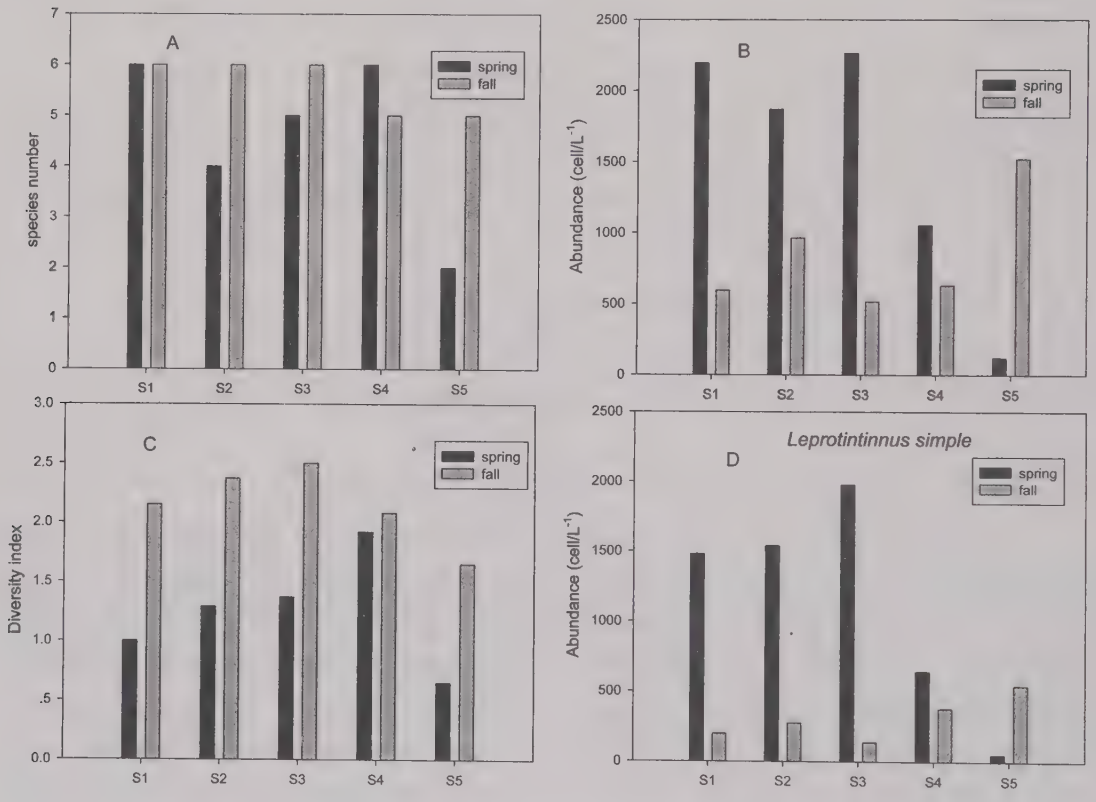

Fig. 2 Seasonal variation of tintinnids in Shantou coastal water

(A) Species number of tintinnids; (B) Abundance of tintinnids; (C) Diversity index of tintinnids; (D) Dominant species of tintinnids

3.2 Relationship between tintinnids and environment parameters

Pearson correlation analysis was carried between environmental parameters and tintinnids. Tintinnids abundance showed negative relationship with salinity (r^2=0.63, $P < 0.05$)(Fig.3), and no significant correlation occurred between tintinnids abundance and other environment parameters, and this may be due to the cold upwelling water carried

sum nutrients rise to the surface water in fall, and rich nutrients and high phytoplankton biomass decrease the importance of tintinnids in the energy flow of aquatic food web.

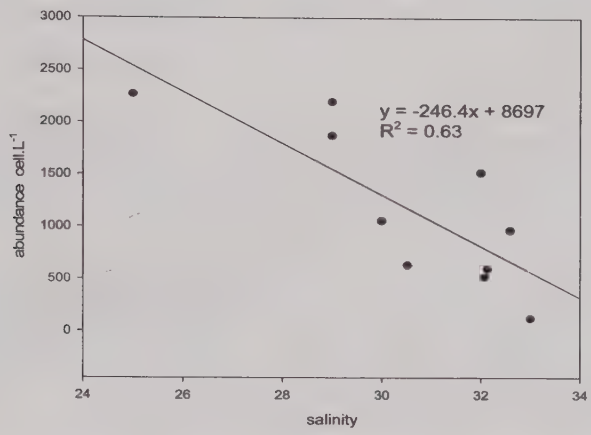

Fig. 3 Relationship between tintinnids abundance and salinity

4 Summary

14 species tintinnids belonging to 7 genus were identified in Shantou coast water, and the dominate species was *Leprotintinnus simple* in spring and fall. High tintinnids diversity and low abundance in fall, and low tintinnids diversity and high abundance in spring. Tintinnids abundance showed negative relationship with salinity, and no significant correlation occurred between tintinnids abundance and other environmental parameters.

Acknowledgements

Financial support of this study was provided by the National Science Committee through Grants NSC U0633007, 40576052.

References

[1] Rassoulzadegan F, Laval P M, Sheldon R W. Partitioning of the food ration of marine ciliates between picoand nanoplankton [J]. Hydrobiologia, 1988, 159: 75 - 88.

[2] Stoecker D K, Michaels A E. Respiration, photosynthesis and carbon metabolism in planktonic ciliates [J]. Marine Biology, 1991, 108: 441 - 447.

[3] Thompson G A. Tintinnid diversity trends in the southwestern Atlantic Ocean (29-60°S) [J]. Aquatic Microbial Ecology, 2004, 35: 93 - 103.

[4] Verity P G. Grazing, respiration, excretion, and growth rates of tintinnids [J]. Limnology and Oceanography, 1985, 30(6): 1 268 - 1 282.

[5] Verity P G. Abundance, community composition, size distribution, and production rates of tintinnids in Narragansett Bay, Rhode Island [J]. Estuarine Coastal and Shelf Science, 1987, 24: 671 - 690.

[6] Safi K A, Griffiths F B, Hall J A. Microzooplankton composition, biomass and grazing rates along the WOCE SR3 line between Tasmania and Antarctia [J]. Deep-Sea Research, 2007, 54: 1 025 - 1 041.

[7] Kofoid C A, Campbell A S. A conspectus of the marine and freshwater ciliata belonging to the suborder Tintinoinea, with descriptions of new species principally from the agassiz expedition to the eastern tropical pacific [M]. 1929: Univ. Calif. Pub. Zool: 1 - 403.

[8] Kofoid C A, Campbell A S. The ciliata: the Tintinnoinea [J]. Bull. Mus. Comp. Zool, 1939, pp 1-473.

[9] Carey P G. Marine Interstitial Ciliates [M]. London: Chapman & Hall, 1992: 314-324.

[10] XU K D, HONG H S, SONG W B, et al. Study on tintinnine ciliates in the Tai wan strait (Cilipohora: Tintinnina) [J]. Acta Zootaxonomica Sinica, 2001, 26(4): 454 - 466.

汕头沿岸水体沙壳纤毛虫季度变化

刘华雪[1,3]，黄良民[1]，谭烨辉[1]，宋星宇[1]，黄建荣[2]

（1. 中国科学院南海海洋所 海洋生物资源可持续利用重点实验室，广东 广州 510301；
2. 中山大学 生命科学学院， 广东 广州 510275；3. 中国科学院研究生院，北京 10049）

摘 要：在 2007 年枯水期（4 月）和丰水期（11 月）期间，对汕头沿岸海区沙壳虫进行了采样研究，探讨了沙壳虫的空间分布和种类组成。调查发现，除了表层海水温度以外，表层海水盐度、硝酸盐浓度、硅酸盐浓度均是春季低于秋季。在两个季节的 5 个采样点共鉴定出 7 属 14 种沙壳纤毛虫，其中优势种均为简单薄铃虫 *Leprotintinnus simple*。秋季沙壳虫丰度低，多样性指数高；春季丰度高，多样性指数低。沙壳虫丰度与水体营养盐含量并无明显的相关性，但同盐度呈显著负相关(r^2=0.63, P < 0.05)，显示出沙壳纤毛虫对汕头海域对不同季节环境特征的响应。

关键词：沙壳纤毛虫；空间分布；种类组成；汕头海域

Research and realization of visual digital ocean system

ZHANG Feng [1, 2], LI Hao-qian [2], LIU Jin [2], LI Si-hai [2]

1. *China University of Geosciences School of the Earth Sciences and Resources, Beijing* 100083, *China*

2. *National Marine Data and Information Service Key Laboratory of Digital Ocean, Tianjin* 300171, *China*

Abstract: Sphere model is the research hotspot in the GIS domain presently. It has become a strong integrated platform of spatial information with its strong abilities of spatial data management and visualization. Based on Skyline software, this paper introduces the framework, functions and technical method of realization of visual digital ocean system. The practice proves that the system has a good future in marine information visualization and sharing.

Keywords: skyline, digital ocean, sphere model, visualization, data sharing

1 Introduction

"Digital Ocean" was born along with the appearance of the "Digital Earth" strategy. It is an integrated ocean system formed by massive solid observed data with multi-resolution, polymorphism, multi-type, and its analysis algorithms and models. It simulates the status of the real ocean, recurs and predicts through the methods of digitalization, visualization and dynamic display, etc. The techniques it uses involve "3S", virtual realization, simulation and interactive operation. "Digital Ocean" provides us a way to understand the ocean most sufficiently, explore and utilize it effectively [1].

The "908" program did some research on visual digital ocean system, including ocean data collection, processing, computation and analysis, also the management of data base and its integrated application. The visual integrated application of marine data is considered as the research's key point and core. The most popular integrated application mode presently is the integration and visualized sharing of multi-source marine information base on sphere system. In China, the polar track geographic information system developed by Polar Research Institute of China integrates various kinds of data by using Skyline platform, which also realize the visual query and display of information. The data integrated by it involve the GPS track data, the stationary data, and the science investigation data on physical oceanography, marine chemistry, biology and geography.

Received on Feb. 27, 2011

Corresponding author: zhangfeng@mail.nmdis.gov.cn

Beyond the sea, the most successful application of integrated spatial information is GoogleEarth software. Base on sphere model, the GoogleOcean published in May 2009 integrates the remote sensing image, the basic geographical data, pictures and the terrain model. Meanwhile it realizes the integrated display of the seawater, the seafloor terrain and the sea level data modules. Thus a real and vivid solid marine environment is out there as the improving of the marine modeling function. Besides Google, the other software platforms such as World Wind by NASA, ArcGlobe by ESRI and Skyline by Skyline company, provide the integrated interface of spatial information based on the earth sphere model, which all supply mature platforms for the integration and visualization sharing of marine spatial information. In this paper, the framework, function design and data arrangement method of visual digital ocean system and its realization are introduced.

2 Skyline platform introduction

Skyline is one of the popular sphere model software platforms, which is an interactive environment established by aero image, satellite data, digital elevation model and other 2D or 3D information sources. It can integrate data rapidly and support large database and real-time information flow communications technique effectively. It is a set of software system with multi-platform and multi-function, which is hardware independent [2].

The Skyline software platform involves 3 major categories of products, and each of category contains several relative software packages. (1) TerraBuilder Suite: It supports multi-format data input, which can create, edit and obtain 3D terrain surface data set and scene. (2) TerraExplorer Suite: This is a set of powerful desktop application, which is used to edit, annotate and publish interactive 3D environment, and can also accept customization. (3) TerraGate Suite: A set of strong network data server software that transmits 3D geography data in real-time, and can be visited through internet.

Skyline is good at redevelopment, and the TerraExplorer API it supplied is a new COM-GIS environment, which is 3D GIS developer oriented. Based on the COM standard and java script standard of Microsoft, powerful 3D GIS functions are provided with ActiveX controls and java script. The TerraExplorer API can be conveniently embedded into the advanced visual development environment to redevelop.

3 Design of visual digital ocean system

3.1 Target of system

This Skyline-based system goes in for establishing a marine information visualization sharing platform for related management departments and researchers in the dedicated

network. The services it provides include the query & download, online computation of analysis model and marine data visualization, and also the display and publication of marine management information.

3.2 Technique and framework

According to the construction target, this system is consistent with SOA framework. Based on B/S model, it adopts AJAX technique and keeps the same style with the standard WEB. It takes Oracle 11G as the background data base management platform, and combines the spatial data and attribute data together for easy management. TerraBuilder is used to edit and produce the 3D sphere scene, while TerraGate is for publication. TerraExplore Pro and ASP.net are the foundational development platform, which is used for redevelopment of functions. A classic three-layer framework is taken for a better serviced and extended system. The framework of the system is illustrated in Fig. 1.

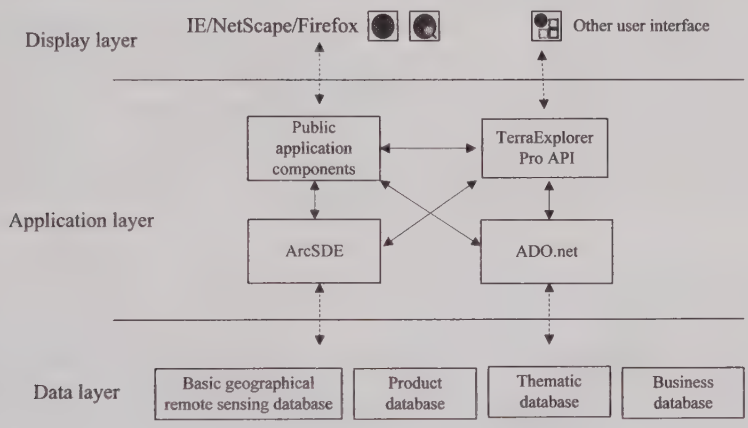

Fig. 1 Framework of the system

3.2.1 Data layer

Data layer is the source of all the data of the system, including basic geography and remote sensing database, production database, thematic database and business database. Through the Goedatabase model, the spatial data can be stored in Oracle by ArcSDE and distributed on several database servers.

3.2.2 Application layer

The application layer is the core layer for realizing the system functions, which contains public application components, TerraExplorer API components and the database interfaces (ArcSDE and ADO.net). All of them call each other through the standard COM interface.

3.2.3 Display layer

The functions of the display layer are offered to users through graphical user interface (GUI), which displays the information and transfers user's operation to the application layer components to realize the interoperation of the system.

3.3 Function design

There are nine modules in this system, which are basic information, sea area management, islands and coastal area, marine resource, marine environment, marine disaster, marine enforcement, marine right and polar ocean. According to their functions, those modules can be extended into several categories, which are, basic marine geographical information display, seafloor terrain browse, query display of marine graphical vector information (such as the vector graph of marine functional zonation, the vector line of enforcement track, the vector line of marine right, etc), visualized simulation of marine environment information(such as the 3D dynamic simulation of ocean current, the color rendering of seawater temperature, the dynamic simulation of storm tide, etc), basic data download, the association of attribute data and geographical data, etc. The corresponding data storage and the realization method are different. Fig. 2 illustrates the functions of the system.

3.4 Data organization and storage

The data in the system are categorized into basic geographical remote sensing data, production data, thematic data and business data according to the function design of the system and the feature of marine business. Basic geographical remote sensing data and seafloor terrain DEM are the basic data source of the sphere scene making. Basic geographic remote sensing data are stored in spatial database by Geodatabase model of ArcSDE, and it is managed and applied with the principle of vector and grid integration.

The basic geographical data include global data on a scale of 1:10 000 000, the whole China Sea region data on a scale of 1:5 000 000 and 1:1 000 000, China coastal data on a scale of 1:250 000, and important region data on a scale of 1:50 000. The major elements are introduced in Tab. 1. The remote sensing images involve several sensor image data like TM, SPOT, QuickBird and MODIS. Their resolutions differ from 1 km to 0.6 m. The black border of each image is removed by mosaic processing the image of the nearby orbit in the same sensor. ArcSDE is taken to store, manage and compress the images. The half-minute grid DEM data of the important sea region draw out from the multi-beam data, and are stored under the certain directory of the data server. The

production data contain the statistical analysis results of basic marine data (which has a data set format), grid graph & image products, video, 3D model and so on, which are stored in Oracle database with the format of BLOB, according to their categories. Thematic data are marine background information data of each subject. Business data is the result information of the marine management business. These two kinds of data both contain vector graphic layer and relational data table, which are stored in Oracle database through Geodatabase model and relational data table, respectively.

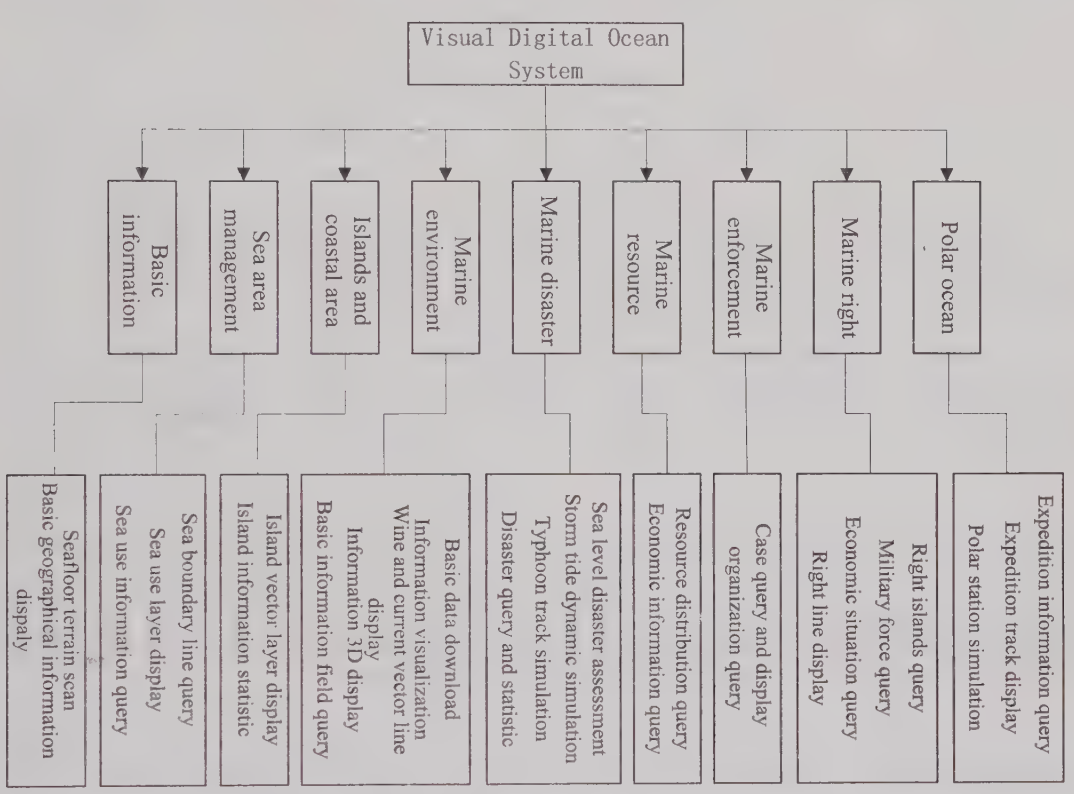

Fig. 2 Functions of the system

Tab.1 Elements of basic geographical data

Coast Line	Isobath	Depth Point	Dry Shoal	Reef	Contour	Label Point	Administrative Borderline	Residential Area	.....

4 Realization

The visual digital ocean system takes the 3D sphere model as the system framework. The construction of the sphere model and the seafloor scene are the precondition of the system realization. The overlap display of vector data and the making & integration of 3D

model are the base of the visualization. The publication of the scene files is the key point of the system realization. The design functions of the system are realized by calling TerraExplorer API interface in the ASP.net environment.

4.1 Construction of Sphere Model

The reference frame of the sphere model is built based on WGS-84 geoid and WGS-84 ellipsoid, then our system can be built. The data of Beijing 54 and Xi'an 84 coordinate system need to be transformed to that of WGS-84 coordinate system.

Tab. 2 Parameter of WGS-84 ellipsoid

Ellipsoid	Long Half-Axis a	Short Half-Axis b	Flattening of Ellipsoid α	First Eccentricity e^2
WGS-84 Ellipsoid	6 378 137	635 6751.314	1/298.257 223 563	0.006 694 379 901 3

4.2 Construction of the terrain scene

The basic data forming the terrain scene in the visual digital ocean system include the seafloor terrain DEM data, the basic geographical remote sensing image and the texture data. The methods of constructing the terrain scene by TerraBuilder are as follows:

First, create a new terrain scene project and make an empty sphere. Set two parameters: (1) File Directory. Considering the multi-server we use, the network directory is taken comparing with local directory. (2) Limit the Elevation Value. We set an elevation range between -5 000 m and 8 000 m, and the values beyond this range are abnormal or empty value, which will be filtrated out from the elevation data.

Second, load data. Image, elevation and vectors are three categories of data for constructing the terrain scene. When loading, specify the data type, the projective way and the coordinate system, in order to transform to WGS-84 coordinate. After loading a single data file onto the sphere, two operations should be taken: (1) Data cutting. Cut the black border, the empty area and the overlap of the image data using the cutting tool of TerraBuilder. (2) Data accuracy and visual range setting. Reset the original data according to the system's accuracy requirement. Set the visual range to make sure in which angle range the data are visible. Besides these two basic operations, color adjustment and data organization, etc, are available, too.

Third, establish the pyramid structure of data. The sphere terrain scenes are displayed one layer by another, and their data storage are graded and parted in pyramid structure. TerraBuilder can be used to establish image pyramid, yet it takes a considerable long time.

In the end, create the mpt file. Mpt file is the final terrain scene file created by TerraBuilder, which can be opened directly by TerraExplorer Pro or be online published and applied by TerraGata.

4.3 Overlapping display of vector data

The vector data used in our system can be categorized by element type into point, line and polygon, while by content can be categorized into the basic geographical data on different scale (such as administrative borderline, water system and road, etc) and the various thematic data(marine resource distribution, bio-chemical elements distribution and depth points layer, etc). There are two methods of overlapping the vector data onto the sphere model: (1) Make fly layer using TerraExplorer Pro to display. (2) Directly publish the vector data by TerraGata SFS(Spatial Framework Services). The first method processes the vector data into spatial object, then load onto the sphere as the layer and keep the attribute value of the vector data. The second method processes the vector data into grid images, then transport to the user with the data stream, which strongly improves the loading speed. Thus, it's more proper to make fly layer when the point and line element data and the label data, or the spatial object is small, while the SFS method is better for the situation of large data magnitude.

4.4 3D model making and integrating

The 3D models in this system can be categorized into 3 parts, which are architecture model, landscape model and facility model. The architecture model involves port, dock, the marine supervising department, the observing station, the polar expedition station and so on. The landscape model involves dam, lighthouse, seafloor pipeline, and fish and so on. The facility model is comprised by enforcement plane and marine expedition ship and so on. There are two methods for making model: one is establishing model directly in the terrain scene of the sphere model using the modeling tools of TerraExplorer Pro; another one is making the model files using the popular 3D modeling software (such as 3dMax), and put the model files into the terrain scene by setting the position of the model. The visualization is realized by integrating the 3D model to the 3D terrain scene of sphere model.

4.5 Scene data publication

The sphere scene data set (mpt) is published by TerraGate, which supports the standard WFS/WMS application, and can be browsed through the normal IE explorer by users. If the data magnitude of the scene file is huge, the DirectConnect can be used to connect each module and publish the scene project file directly.

The cache technique is used in the scene data publication, which improves the server's responding speed under the multi-customer situation. Considering the high standard software and hardware environments needed, the recommend configuration includes the CPU with multi-core and multi-thread, the cache bigger than 1GB (determined by the accessing quantity, each one more accessing leads 2MB increase of cache), and the explorer newer than IE6.

4.6 System function development

In the ASP.net environment, the system functions such as scene display, typhoon path, and marine information visualization, are realized by calling TerraExplorer API, using the related interface and function methods. Fig. 3 shows the realized system function interface.

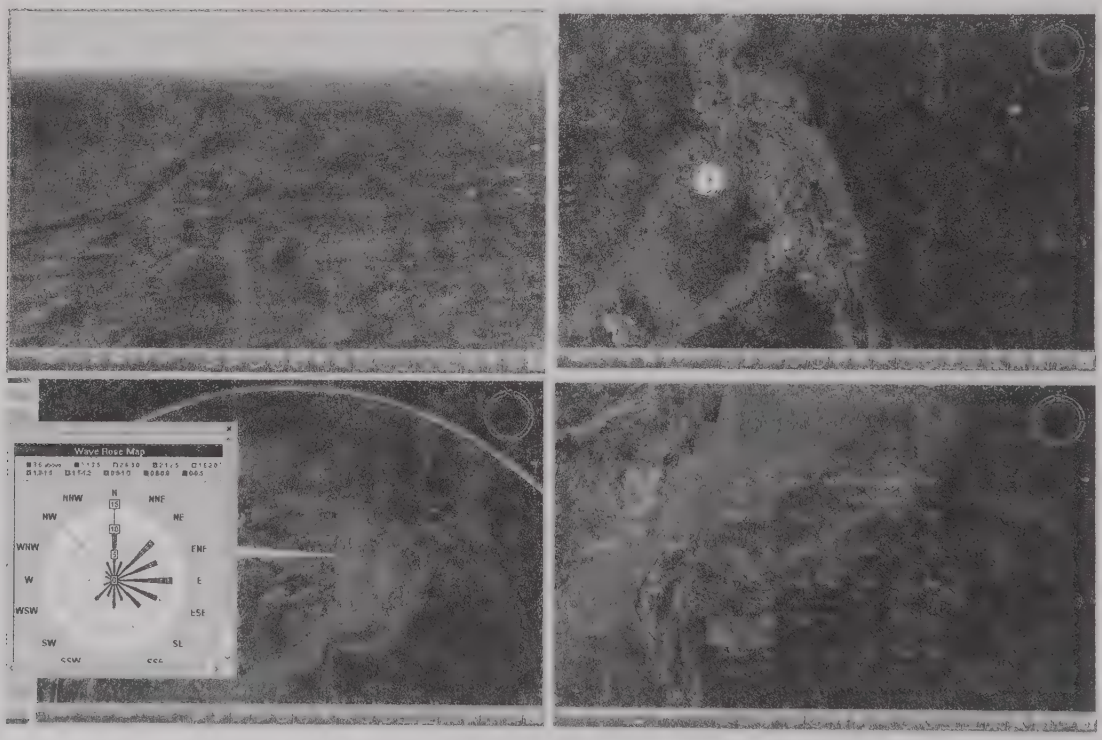

Fig. 3 Interface of system function

5 Conclusion

The key problem that the system construction needs to be solved is the run efficiency. The major factors that affect the efficiency include: (1) Large quantity of vector and grid

graphics objects employed by the system; (2) Massive seafloor terrain DEM data forming by remote sensing image and multi-beam data; (3) Heavy accessing from users; (4) Huge real-time computing burden when visualizing the basic marine environment field. Researches and experiments prove three solutions are effective: (1) Use WFS to supply vector service; (2) Dispose Web server, terrain scene publishing server, vector data server and thematic data server separately; (3) Update the database server and the application server to 64-bit CPU and 64-bit operation system.

The research and development of visual digital ocean system based on Skyline sphere model present a good solution for the integration and visualization sharing of massive marine information of multi-subject. Practices and applications prove this system has a stable performance and high graphical query efficiency. It realizes the integrating and sharing service of marine information in the dedicated network environment, which shows a bright future of application.

Acknowledgements

This study is supported by State Oceanic Administration "908" Program (908-03) and State Oceanic Administration Funds for Young Scholar (No. 2009609).

References

[1] The overall implementation program of 908-03 "Digital Ocean" Foundational Information Framework of China [R]. Beijing: State Oceanic Administration People's Republic Of China, 2006.

[2] Introduction of Skyline Software Products [EB/OL].http://www.skysymbol.com/product

[3] ZU Weiguo, DENG Fei, LIANG Jingyong. Realization of Visualization System for Large Volume 3D GIS Data [J]. Bulletin of Surveying and Mapping, 2008, (7): 39 - 40.

[4] MA Ni, LI Weigong, MA Jianliang. The Planning of Application Software System of Spatial Information Service Organizations [J]. Bulletin of Surveying and Mapping, 2008, (7): 19 - 22.

[5] LI Hu, WU Jiazhu. Research and Realization of a Battlefield Situation System Based on Skyline [J]. Computer Engineering and Science, 2009, 31(4):26 - 29.

[6] DENG Jie, XIA Chunlin, WANG Runfang. Establishment of 3D Urban Landscape Model Based on Skyline Terrasuite [J]. Remote Sensing Technology and Application, 2008, 23(5): 529 - 533.

[7] SHI Sui-Xiang. Study on Soft Fusion Strategy of Multi-Channel Incertitude Information in Digital Ocean [D]. Shenyang: Northeastern University, 2005.

数字海洋可视化系统研究与实现

张 峰[1,2]，李昊倩[2]，刘 金[2]，李四海[2]

（1. 中国地质大学 地球科学与资源学院，北京 100083；2. 国家海洋信息中心
数字海洋重点实验室，天津 300171）

摘 要：球体模型系统是目前 GIS 领域的研究热点，它以强大的空间数据管理能力，丰富直观的信息表现能力迅速成为空间信息集成共享的有力平台。以 Skyline 软件平台为基础，介绍了数字海洋可视化系统的体系架构、功能设计和技术实现方法。实践应用表明，该系统在多源海洋信息可视化集成共享方面具有良好的应用前景。

关键词：skyline；数字海洋；球体模型；可视化；数据共享

海 洋 通 报（英文版）

HAIYANG TONGBAO

2011 年 5 月 第 13 卷 第 1 期

目 次

热带印度洋海温异常与 ENSO 关系的进一步研究 …… 蔡 怡 等 (09)

台湾以东黑潮锋的中尺度过程研究 ……王 琦 等 (24)

变水深对畸形波及其时频能量谱的影响…… 崔 成 等 (39)

天津近海潮汐特征分析……李希彬 等 (49)

南极普里兹湾溶解态镉的分布 ……孙维萍 等 (59)

从培养的微藻中初步筛选抗菌和抗肿瘤活性物质……邓 伟 等 (70)

汕头南澳海水养殖区不同水层重金属的分布和环境质量评价 …… 周艳晖 等 (79)

汕头沿岸水体沙壳纤毛虫季度变化 ……刘华雪 等 (86)

数字海洋可视化系统研究与实现 …… 张 峰 等 (96)

Marine Science Bulletin

Marine Science Bulletin publishes papers on marine science and technology including physical oceanography, chemical oceanography, marine biology, marine geology, environmental oceanography, estuarine & coastal sciences, marine technology, digital ocean, coastal zone management, ocean engineering, marine economics, etc., and aims to promote international academic exchange.

Editor-in-Chief: XU Sheng (徐　胜)
Associate Editor-in-Chief: LI Dong-xu (李东旭)　XUE Hui-feng (薛惠芬)
Executive Editor: QIU Wen-jing (邱文静)　LI Xue (李　雪)　YANG Rui (杨　瑞)
LI Xiao-guang (李晓光)　DONG Yi (董　艺)　YUAN Ze-yi (袁泽轶)
English proofed by: WANG Qi (王　琦)

Semi-annually (started in 1999, sum 25)
Publication date: May 15th and Oct. 15th

Marine Science Bulletin **(Vol. 13, No. 1, May 2011)**

Responsible Institution:
State Oceanic Administration of China
Sponsored by:
National Marine Data and Information Service
Edited by:
Office of Marine Science Bulletin (English edition)
Printed by:
Printery of National Marine Date and Information Service

Published by:
Office of Marine Science Bulletin (English edition)
E-mail: msb@mail.nmdis.gov.cn
Tel: (022) 24011287
Address: 93 Liuwei Rd., Hedong District, Tianjin 300171, China

---

ISSN1000-9620
CN12-1271/N

ISSN 1000-9620

Price: $ 30.00 / ￥40.00 Per year